Université de Lille

Université de Lille

Doctoral School **ED ENGSYS-632**

University Department **Unité de Mécanique de Lille - Joseph Boussinesq ULR 7512**

Thesis defended by **Saad Raza**

Defended on **December 15, 2025**

In order to become Doctor from Université de Lille

Academic Field **Applied Mathematics**

Speciality **Fluid Mechanics**

Study of the influence of a dispersed phase on the stability of the Rayleigh-Bénard system

Thesis supervised by	Silvia HIRATA	Supervisor
	Enrico CALZAVARINI	Co-Monitor

Committee members

Referees	Harunori YOSHIKAWA	Professor at Doshisha University, Kyoto (Japan)
	Sergio CHIBBARO	Professor at Université Paris-Saclay
Examiners	Farzam ZOUESHTIAGH	Professor at Université de Lille and Institut d'électronique de microélectronique et de nanotechnologie (IEMN)
	Diwakar S. VENKATESAN	Associate Professor at Jawaharlal Nehru Centre for Advanced Scientific Research (India)
Guest	Francesco ROMANO	HDR Associate Professor at École nationale supérieure d'Arts et Métiers (ENSAM)
Supervisors	Silvia HIRATA	HDR Associate Professor at Université de Lille
	Enrico CALZAVARINI	Associate Professor at Université de Lille

Université de Lille

Université de Lille

Doctoral School **ED ENGSYS-632**

University Department **Unité de Mécanique de Lille - Joseph Boussinesq ULR 7512**

Thesis defended by **Saad Raza**

Defended on **December 15, 2025**

In order to become Doctor from Université de Lille

Academic Field **Applied Mathematics**

Speciality **Fluid Mechanics**

Study of the influence of a dispersed phase on the stability of the Rayleigh-Bénard system

Thesis supervised by	Silvia HIRATA	Supervisor
	Enrico CALZAVARINI	Co-Monitor

Committee members

Referees	Harunori YOSHIKAWA	Professor at Doshisha University, Kyoto (Japan)
	Sergio CHIBBARO	Professor at Université Paris-Saclay
Examiners	Farzam ZOUESHTIAGH	Professor at Université de Lille and Institut d'électronique de microélectronique et de nanotechnologie (IEMN)
	Diwakar S. VENKATESAN	Associate Professor at Jawaharlal Nehru Centre for Advanced Scientific Research (India)
Guest	Francesco ROMANO	HDR Associate Professor at École nationale supérieure d'Arts et Métiers (ENSAM)
Supervisors	Silvia HIRATA	HDR Associate Professor at Université de Lille
	Enrico CALZAVARINI	Associate Professor at Université de Lille

Université de Lille

Université de Lille

École doctorale **ED ENGSYS-632**

Unité de recherche **Unité de Mécanique de Lille - Joseph Boussinesq ULR 7512**

Thèse présentée par **Saad Raza**

Soutenue le **15 décembre 2025**

En vue de l'obtention du grade de docteur de l'Université de Lille

Discipline **Mathématiques Appliquées**

Spécialité **Mécanique des Milieux Fluides**

Étude de l'influence d'une phase dispersée sur la stabilité du système Rayleigh-Bénard

Thèse dirigée par	Silvia HIRATA	directrice
	Enrico CALZAVARINI	co-encadrant

Composition du jury

Rapporteurs	Harunori YOSHIKAWA	professeur au Doshisha University, Kyoto (Japan)
	Sergio CHIBBARO	professeur à l'Université Paris-Saclay
Examinateurs	Farzam ZOUESHTIAGH	professeur à l'Université de Lille and Institut d'électronique de microélectronique et de nanotechnologie (IEMN)
	Diwakar S. VENKATESAN	MCF au Jawaharlal Nehru Centre for Advanced Scientific Research (India)
Invité	Francesco ROMANO	MCF HDR au École nationale supérieure d'Arts et Métiers (ENSAM)
Directeurs de thèse	Silvia HIRATA	MCF HDR à l'Université de Lille
	Enrico CALZAVARINI	MCF à l'Université de Lille

This thesis has been prepared at

Unité de Mécanique de Lille - Joseph Boussinesq ULR 7512
Polytech' Lille, Bâtiment ESPRIT
Avenue Paul Langevin
59650 Villeneuve-d'Ascq
France

Web Site https://uml.univ-lille.fr/

To my parents, Syed Raza Hassan, Farkhanda Raza

To my wife, Ayesha

I also dedicate this work to all those who have supported me throughout this journey.

Study of the influence of a dispersed phase on the stability of the Rayleigh-Bénard system

Abstract

The interaction between thermal convection and suspended particles is central to many geophysical and industrial processes, ranging from magmatic flows and sediment-laden currents to bubble-driven chemical reactors. Even in dilute concentrations, particles can profoundly alter convective stability through momentum and heat exchange with the surrounding fluid. Despite its importance, a general framework that disentangles mechanical and thermal feedbacks remains limited. This thesis addresses this challenge by investigating the linear stability of Rayleigh–Bénard (RB) system in fluid layers containing a dispersed phase of non-Brownian thermal particles, using a two-fluid Eulerian approach. Particular focus is placed on how particle material properties (density, heat capacity) and geometric features (size) combine with boundary injection conditions to influence the onset of convection. In the first part of this work, particles are introduced in the system at their terminal velocity with a prescribed temperature. The results show that both heavy and light particles invariably stabilize the system, raising the critical Rayleigh number by large factors—up to 30 for bubbles and 60 for particles heavier than the fluid at volume fractions of 0.1%. When particles are injected at their terminal velocity, the divergence of the particle velocity field vanishes everywhere in the system, ensuring uniform concentration and preventing accumulation. Stabilization results from mechanical coupling, which damps fluid motion, and thermal inertia, which modifies interphase heat exchange. A second configuration examines the particulate RB (pRB) system, where particles are injected at different inlet velocities and constant volumetric flux. The results show that altering the injection velocity permits particle accumulation and produces an asymmetry: increasing inlet velocity destabilizes the system for heavy particles but progressively stabilizes it for light ones. Accumulation also depends on injection regime, appearing in downwelling regions for sub-terminal injection and in upwelling regions for super-terminal injection. When the injection velocity matches the terminal velocity, no accumulation occurs as particle concentration remains constant. Finally, the role of thermal coupling is investigated by varying the particle-to-fluid specific heat capacity ratio. The results show that for heavy particles, stronger coupling consistently enhances stability, while for light particles, it can either stabilize or destabilize depending on injection conditions and flux. In all cases, convection onset remains stationary, occurring through a pitchfork bifurcation as in the classical RB problem, but with significantly shifted thresholds and altered spatial structures. Together, these findings demonstrate that even dilute suspensions can shift convective thresholds by more than an order of magnitude and, in some cases, permit convection under heating from above. The results establish a theoretical foundation for particulate RB convection and provide a framework for future experimental and numerical studies relevant to geophysical, environmental, and industrial flows.

Keywords: particle/fluid flow, Rayleigh–Bénard convection, flow instabilities

Unité de Mécanique de Lille - Joseph Boussinesq ULR 7512
Polytech' Lille, Bâtiment ESPRIT – Avenue Paul Langevin – 59650 Villeneuve-d'Ascq – France

Étude de l'influence d'une phase dispersée sur la stabilité du système Rayleigh-Bénard

Résumé

L'interaction entre convection thermique et particules en suspension est au cœur de nombreux processus géophysiques et industriels, allant des écoulements magmatiques et des courants sédimentaires aux réacteurs chimiques à bulles. Même à des concentrations diluées, les particules peuvent altérer profondément la stabilité convective par leur quantité de mouvement et leurs échanges thermiques avec le fluide environnant. Malgré son importance, un cadre général distinguant les rétroactions mécaniques et thermiques reste limité. Cette thèse aborde ce défi en étudiant la stabilité linéaire du système Rayleigh-Bénard (RB) dans des couches fluides contenant une phase dispersée de particules thermiques non browniennes, en utilisant une approche eulérienne à deux fluides. Une attention particulière est portée à la manière dont les propriétés des particules (densité, capacité thermique) et leurs caractéristiques géométriques (taille) se combinent aux conditions d'injection aux limites pour influencer le déclenchement de la convection. Dans la première partie de ce travail, les particules sont introduites dans le système à leur vitesse terminale et à une température prescrite. Les résultats montrent que les particules lourdes et légères stabilisent invariablement le système, augmentant considérablement le nombre de Rayleigh critique : jusqu'à 30 pour les bulles et 60 pour les particules plus lourdes que le fluide à des fractions volumiques de 0,1%. Lorsque les particules sont injectées à leur vitesse terminale, la divergence du champ de vitesse des particules disparaît partout dans le système, assurant une concentration uniforme et empêchant l'accumulation. La stabilisation résulte du couplage mécanique, qui amortit le mouvement du fluide, et de l'inertie thermique, qui modifie l'échange thermique interphasique. Une deuxième configuration examine le système RB particulaire (pRB), où les particules sont injectées à différentes vitesses d'entrée et à flux volumétrique constant. Les résultats montrent que la modification de la vitesse d'injection permet l'accumulation des particules et produit une asymétrie : l'augmentation de la vitesse d'entrée déstabilise le système pour les particules lourdes, mais le stabilise progressivement pour les particules légères. L'accumulation dépend également du régime d'injection, apparaissant dans les régions descendantes pour l'injection subterminale et dans les régions ascendantes pour l'injection superterminale. Lorsque la vitesse d'injection correspond à la vitesse terminale, aucune accumulation ne se produit car la concentration en particules reste constante. Enfin, le rôle du couplage thermique est étudié en faisant varier le rapport de capacité thermique massique particules/fluide. Les résultats montrent que pour les particules lourdes, un couplage plus fort améliore systématiquement la stabilité, tandis que pour les particules légères, il peut se stabiliser ou se déstabiliser selon les conditions d'injection et le flux. Dans tous les cas, le début de la convection reste stationnaire, se produisant par une bifurcation en fourche comme dans le problème RB classique, mais avec des seuils significativement décalés et des structures spatiales altérées. Ensemble, ces résultats démontrent que même des suspensions diluées peuvent décaler les seuils de convection de plus d'un ordre de grandeur et, dans certains cas, permettre la convection sous chauffage par le haut. Ces résultats établissent un fondement théorique pour la convection RB particulaire et fournissent un cadre pour de futures études expérimentales et numériques pertinentes pour les écoulements géophysiques, environnementaux et industriels.

Mots clés : écoulement de particules/fluides, convection de Rayleigh–Bénard, instabilités d'écoulement

Unité de Mécanique de Lille - Joseph Boussinesq ULR 7512
Polytech' Lille, Bâtiment ESPRIT – Avenue Paul Langevin – 59650 Villeneuve-d'Ascq – France

Acknowledgements

I would like to express my sincere gratitude to my supervisor, **Silvia Da Costa Hirata**, and my co-supervisor, **Enrico Calzavarini**, for their unwavering support and guidance throughout my doctoral studies. Their constant encouragement, thoughtful feedback, and constructive critique have been invaluable in shaping this dissertation, while their patience and inspiration have greatly contributed to my growth as both a researcher and an individual.

Above all, my gratitude goes to ALLAH pak for giving me the strength and knowledge and my Salam to Prophet Muhammad (PBUH) whose life is candle for us in darkness of life. I wish to express my deepest and most heartfelt gratitude to my beloved wife, **Ayesha Javed**, whose unwavering love, patience, and encouragement sustained me throughout this long and demanding journey. Her constant support, quiet strength, and boundless understanding were my greatest source of motivation and resilience, especially during moments of doubt and exhaustion. She stood beside me through every challenge, celebrating the small victories and offering comfort during setbacks, and her belief in me never wavered. This thesis is as much a reflection of her sacrifices and support as it is of my own efforts, and it would not have been possible without her presence, compassion, and unconditional love.

I am also sincerely thankful to my siblings Syeda Ujalla Raza and Syed Ali Raza. I would also like to sincerely thank my brother-in-laws Adil Javed , Umer Javed and Atiq Javed for their encouragement and support, and as well as my colleagues (Alioune Sene, Katia Ali Amar), for their valuable support and for helping me in countless ways, whether through encouragement or by resolving challenges along the way. I also thank Prof. Leonardo S. B. Alves and Romulo B. Freitas for their collaboration and valuable input. I would like to extend my heartfelt thanks to Prof. Abdullah Shah for his continuous encouragement and invaluable guidance throughout this journey, as well as for his support in helping me develop as a researcher.

Last but not the least, I must express my sincere gratitude to my parents **Syed Raza Hassan** and **Syeda Farkhanda Raza** for providing me unfailing support. I am deeply grateful to my father-in-law **Rana Nasir Javed** and mother-

in-law **Shamshad Javed** for their kindness, prayers, and continued goodwill. Their support and belief in me are truly appreciated. All my achievements and success are the results of their constant strives and continuous prayers. This accomplishment is not possible without them. At last, I am very thankful to everyone who help and pray for my success.

Table of Contents

List of Tables

List of Figures

Chapter 1

Introduction

Outline of the current chapter

1.1 Context

Convection is one of the most fundamental mechanisms of heat and mass transport in fluid systems. Among the many convective phenomena, the Rayleigh–Bénard (RB) system has served as a classical model problem in fluid dynamics and stability theory. In its simplest form, the RB problem describes the onset of convection in a horizontal fluid layer heated from below and cooled from above. This apparently simple configuration has been a cornerstone in the study of pattern formation, hydrodynamic instabilities, and nonlinear dynamics [1, 2]. Its significance extends across a wide range of disciplines, including geophysical flows in Earth's mantle and atmosphere [4, 5], astrophysical convection

in stellar interiors [6], and numerous engineering applications such as cooling technologies and material processing [7, 3].

The theoretical framework for the RB system is based on the Navier–Stokes equations coupled with the heat equation under the Boussinesq approximation. At small temperature differences, heat is transported purely by conduction, and the fluid layer remains quiescent. However, when the temperature gradient exceeds a critical value, buoyancy forces overcome viscous and diffusive dissipation, leading to the onset of convective motion. This transition is governed by the Rayleigh number (Ra), a dimensionless parameter that quantifies the ratio of buoyancy to dissipation. Another important parameter is the Prandtl number (Pr), which characterizes the relative importance of viscous to thermal diffusion. The interplay between these parameters determines both the onset of convection and the subsequent stability of flow patterns.

Historically, the problem was first analyzed by Lord Rayleigh [9] through a linear stability analysis, which established the critical Rayleigh number for convection onset. Later, G. I. Taylor [10] made fundamental contributions to hydrodynamic stability and rotating convection, while E. Hopf introduced the concept of the Hopf bifurcation [11], laying the mathematical foundation for the transition from steady convection to oscillatory flows. Building on these ideas, Lorenz [12] derived a simplified set of nonlinear equations from the RB system, which became a seminal model in chaos theory. The Lorenz system demonstrated that deterministic equations can yield solutions that are highly sensitive to initial conditions, leading to the discovery of deterministic chaos and the famous Lorenz attractor. This breakthrough established the RB system as a central model not only in fluid mechanics but also in nonlinear science and dynamical systems theory.

Over the years, several extensions of the RB problem have been introduced to capture more realistic physical scenarios. These include convection in rotating frames, magnetoconvection under externally applied magnetic fields, and double-diffusive convection where both heat and solute gradients are present. More recently, attention has been directed toward particulate Rayleigh–Bénard systems, in which suspended particles interact dynamically with the fluid motion. The presence of particles modifies both the onset conditions and the

nonlinear evolution of convection, giving rise to new stability characteristics that are relevant in environmental, geophysical, and industrial contexts.

Thus, the RB system not only provides fundamental insights into thermal convection but also serves as a versatile framework for understanding complex multi-physics phenomena. Its extensions, including particulate convection, continue to play an essential role in advancing the theory of hydrodynamic stability and in modeling natural and engineered systems where heat transfer, fluid motion, and particle interactions are intricately coupled. Figures (1.1) and (1.2) shows a visualization of two-dimensional Rayleigh–Bénard convection and related pattern formations respectively.

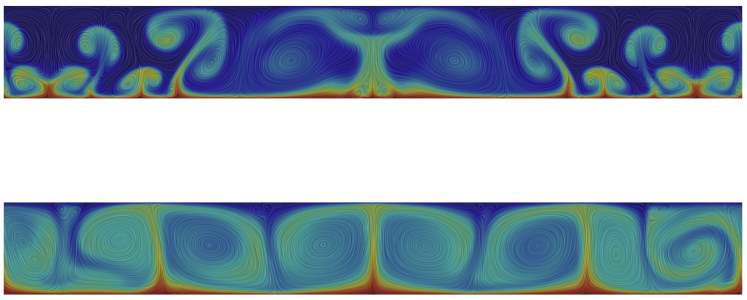

Figure 1.1: Visualization of two-dimensional Rayleigh-Bénard convection. Figure taken from [13].

1.2 Motivation

Convection in particle-laden or more generally dispersed multiphase flows arises in a wide range of natural and industrial settings. In the ocean, suspended sediments interact with convection and mixing processes, influencing large-scale transport and coastal morphodynamics (see Fig. 1.3).

In engineering applications, dispersed-phase convection is equally important. In nuclear systems such as boiling water reactors, the two-phase flow of liquid water and vapor bubbles governs heat transfer and stability (Fig. 1.4a). Another example is magma chambers, where convection interacts with crystals and bubbles, shaping magmatic evolution and volcanic activity (Fig. 1.4b). Similarly, fluidized beds are widely used in chemical processing and energy systems; in

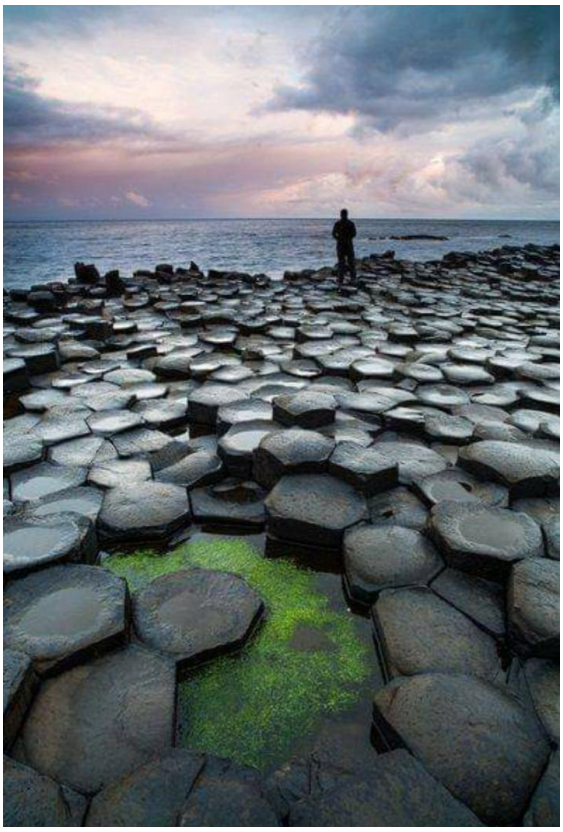

Figure 1.2: Columnar basalt formation at the Giant's Causeway, Northern Ireland. The hexagonal patterns arise from thermal contraction during the cooling of lava. The cellular geometry is reminiscent of the convection cell patterns observed in Rayleigh–Bénard convection [14].

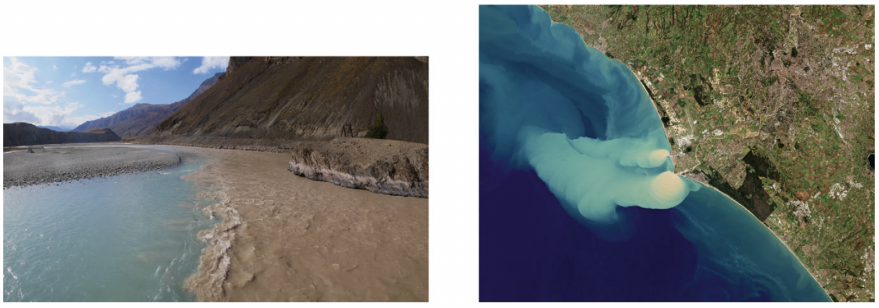

(a) (b)

Figure 1.3: Illustrations of how sediment transport occurs in rivers. Figure taken from [15]

particular, particle-based fluidized beds are being developed for concentrated solar power plants, where efficient heat transfer and storage are essential (Fig. 1.5).

In geophysical systems, volcanic plumes carry ash particles whose interaction with convective currents determines how far the ash is dispersed in the atmosphere (see Fig. 1.6).

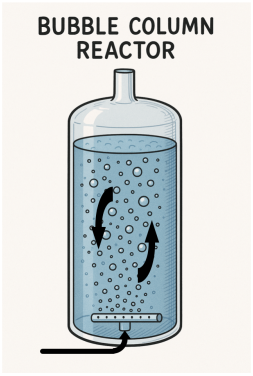

(a) Sketch of a bubble column reactor with gas bubbles rising through the liquid phase.

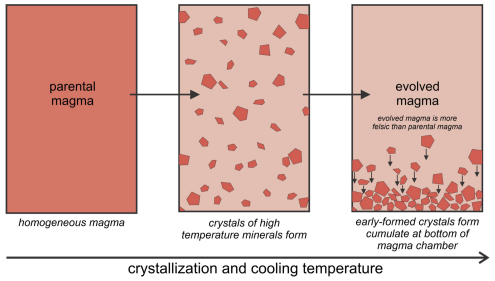

(b) Illustration of a magma chamber and associated processes. Figure taken from [17].

Figure 1.4: (a) Bubble column reactor and (b) magma chamber, illustrating particle–fluid interactions in industrial and geophysical systems.

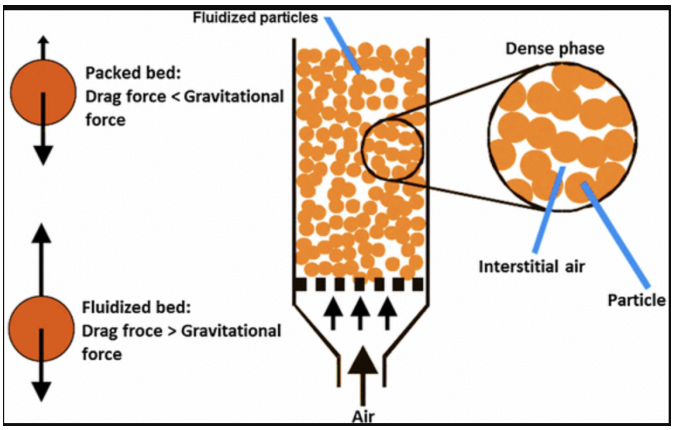

Figure 1.5: Illustration of dense phase fluidization of particles in a fluidized bed. Figure taken from [24]

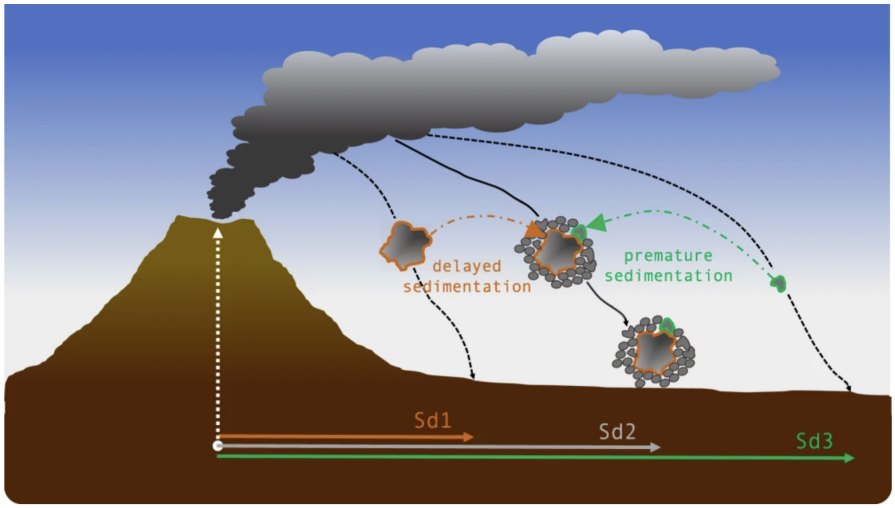

Figure 1.6: Volcanic plume dynamics with premature and delayed sedimentation of ash particles affecting their dispersion in the atmosphere. Figure taken from [23]

The Rayleigh–Bénard system, though idealized, provides a fundamental framework to study such convection phenomena under controlled conditions. By introducing a dispersed phase into this classical problem, we obtain a tractable yet physically rich model that captures the essential mechanisms of multiphase convective instability. Previous studies have shown that particle loading or bubble-induced forces can shift the critical threshold for convection. However, these works are often limited to simplified assumptions or narrow parameter regimes, leaving important aspects of the problem unresolved.

The motivation of this thesis is to address this gap through a systematic linear stability analysis of the particulate Rayleigh–Bénard problem. By conducting a systematic study that aimed to extensively explore the parameters of the problem, from the material properties of the particles to those of their mode of introduction into the system. In addition to its theoretical significance, the analysis also establishes a reference framework for interpreting and modeling dispersed-phase convection in both natural and industrial systems.

1.3 State of the art

The experimental exploration of Rayleigh–Bénard systems containing a dispersed phase began with bubbly convection. Zhong *et al.* [25] showed that the introduction of vapor bubbles could enhance heat transport by up to an order of magnitude through latent-heat exchange and plume intensification, and Lakkaraju *et al.* [33] confirmed that bubbling turbulent convection exhibits large increases in Nusselt number which characterize the efficiency of convective heat transfer relative to conduction. together with reorganized large-scale circulation. The dispersion of air bubbles in cavity Rayleigh–Bénard convection has been explored by Kim *et al.* [26, 27] through combined experimental and numerical approaches. Their findings highlight that, beyond dispersion itself, bubble dynamics are strongly shaped by the large-scale circulation imposed by the tank geometry, particularly when the aspect ratio is close to unity. More recently, Pelusi *et al.* [28] studied convection in concentrated emulsions and demonstrated that finite-size droplets modulate plume emission and generate intermittent heat-flux bursts, revealing the critical role of droplet deformability and rheology. In contrast to these enhancement scenarios, particle-laden convection under rotation has highlighted suppression mechanisms: Joshi *et al.* [29] found that neutrally buoyant microparticles in rotating RBC form porous deposits on the plates, reducing heat transfer and emphasizing that interfacial and boundary-layer conditioning can outweigh plume-seeding effects in the bulk. At the same time, advances in high-resolution velocimetry have refined our understanding of the single-phase large-scale circulation that sets the background flow for dispersed-phase couplings. Horstmann *et al.* [30] reported abrupt global flow-state transformations in rectangular cells, while Barta and Wagner [31] observed rare, system-wide reorientation events of the large-scale circulation in cubic cells using three-dimensional particle-tracking velocimetry. Collectively, these studies demonstrate that the impact of dispersed phases on convective heat transfer depends sensitively on interfacial physics, dispersed-phase properties, and the stability of the underlying large-scale circulation, which itself is strongly controlled by geometry and rotation. It is worth mentioning here the pioneering experimental studies by Solomatov et al. [97] and Lavorel et al. [131] focused on

the settling dynamics of solid particles and to their resuspension in vigorously convective fluids, the more recent experiments on vapour droplets dynamics in a supersaturated RB cell (cloud chamber) [93]

On the numerical side, direct numerical simulations (DNS) have provided valuable mechanistic insight. Earlier pioneering simulations by Climent & Magnaudet [83] demonstrated bubble-induced convection in a quiescent layer, while Iga & Kimura [16] mapped the onset and regime transitions of bubble-driven cellular flows. Oresta *et al.* [32] used a point-bubble model to quantify how bubble buoyancy and thermal coupling shift the effective transport mechanisms, observing that bubbles can both stabilize or destabilize depending on Jacob number. Lakkaraju *et al.* [33, 34] extended this approach to boiling RBC, linking bubble nucleation and superheat to Nusselt enhancement. More recent advances employ particle-resolved DNS: Chen *et al.* [35] resolved thousands of finite-size particles within RBC at Rayleigh numbers up to 10^7, showing how two-way coupling between flow and particles reorganizes turbulence. Wu *et al.* [36] developed robust solvers for three-dimensional particle-laden Rayleigh–Bénard system, while Pan *et al.* [37] and Yang *et al.* [38] explored radiatively heated particle suspensions, identifying new energy-transfer pathways that significantly alter thermal efficiency. At the boundary level [40] showed that bubbles attached to plates can reduce global transport due to conductivity contrasts. Studies with a similar Eulerian-Lagrangian point-particle numerical approach where conducted by Park et al. [39] and in [130, 125, 96, 94]. This line of research goes even beyond the RB setting and extend to general convective turbulent flows, see e.g. [124]. Numerical studies adopting particle resolved approach, where both mechanical and thermal couplings between dispersed phase and the fluid are included, are on the other hand quite recent, with limitations in the number of particles [122, 123, 137]. More frequent are the numerical studies that have attempted a characterization of the one-way coupled dynamics of particles in RB [136, 120, 121, 95, 92]. When the so called two-way coupling is considered, i.e. the particle feedback on the fluid flow, the dynamics and the parameter space of the problem becomes much wider. The recent work by [41] on heavy particles in Rayleigh–Bénard convection demonstrated that, at sufficiently large particle volume fractions, two-way momentum coupling enhances settling by distorting

the flow into smaller scales. These numerical studies collectively establish a nuanced picture in which dispersed phases may either enhance or suppress heat transfer depending on particle properties, loading, and thermal and mechanical forcing.

From a theoretical perspective, linear and weakly nonlinear analyses have recently been extended to particulate Rayleigh–Bénard system. Wollkind and Zhang [48, 49] developed a weakly nonlinear stability analysis of the pure conduction solution for an aerosol one-layer Rayleigh–Bénard model of a Boussinesq particle–gas system, formulated within a two-fluid framework. Their investigations primarily focused on regimes close to the onset of convection, or at Rayleigh numbers restricted to values below 2×10^4. Prakhar *et al.* [50] formulated a two-fluid linear stability model, predicting shifts in the critical Rayleigh number and wavenumber due to particle thermal and momentum coupling. The studies by Nakamura *et al.* [51, 52] revealed that bottom injection of bubbles into an isothermal fluid layer destabilizes the system. Differently from the previously mentioned studies, these authors had considered the possibility of injecting bubbles at sub-terminal velocities, which is more realistic with respect to experiments. In contrast to such destabilizing effects, earlier investigations of particle-laden Rayleigh–Bénard convection demonstrated that small, heavy particles tend to stabilize the flow. Linear stability analysis performed by Kang *et al.* [53] indicated that the critical Rayleigh number increases with particle loading, leading to turbulence suppression and the emergence of cell-like structures. A recent contribution by Chang *et al.* [42] on Rayleigh–Bénard instability in nanofluids highlights the influence of additional transport mechanisms beyond Brownian motion and thermophoresis. In particular, it was shown that gravitational settling of nanoparticles introduces a stabilizing effect that can delay the onset of convection. Although this framework is developed for nanofluids and thus differs fundamentally from our case of non-Brownian particles, their analysis also relies on a linear stability framework, which provides a methodological parallel to the present study. More recently, Srinivas *et al.* [54] performed a weakly nonlinear analysis, deriving Landau amplitude equations that capture symmetry breaking and higher-harmonic generation in particle-laden convection. Building upon the framework of [50], who addressed the linear stability

of Rayleigh–Bénard convection in the presence of heavy inertial particles, we extend the analysis to include both light particles and bubbles. In addition, we introduce the effect of particle injection velocity, a control parameter which, to the best of our knowledge, has not been investigated in this context before. Finally, we examine the role of particle–fluid thermal coupling, thereby providing a more general description of how dispersed phases influence the onset of convection. This extension offers new insights into the parameter space of particulate Rayleigh–Bénard systems and broadens the connection between theoretical predictions and experimental/numerical observations.

1.4 Outline

This thesis is organized into three main parts: Part I (Mathematical Modeling), which includes Chapter 2; Part II (Methodology), comprising Chapter 3 and Chapter 4; and Part III (Results), containing Chapter 5, Chapter 6 and Chapter 7, followed by conclusions and perspectives.

In Chapter 2, we introduce the modeling of disperse multiphase flows. Different modeling strategies (Eulerian, Lagrangian, and fully resolved descriptions) are reviewed, and the governing equations for the particulate and fluid phases are derived. The chapter concludes with the formulation of the particulate Rayleigh–Bénard (pRB) model system in both dimensional and dimensionless form.

Chapter 3 is devoted to the linear stability analysis of the pRB system. The general framework of stability analysis is first presented, followed by its application to the pRB model. Both the conductive state and the linearized perturbation equations are discussed, leading to modal analysis results. A particular case where particles are injected at their terminal velocity is also examined.

In Chapter 4, we describe the numerical methods employed to solve the stability problem. The shooting method, Galerkin method, and a matrix-forming approach are introduced, with a comparison and validation of these approaches provided at the end of the chapter.

Part III presents the main findings of this study. In Chapter 5, we investigate the stabilization of the Rayleigh–Bénard system by the injection of inertial parti-

cles and bubbles at terminal velocity, analyzing the effects of particle density, flux, size, and thermal coupling. Chapter 6 focuses on the role of particle injection velocity, highlighting its impact on the system's stability and the onset of convection. Chapter 7 addresses the influence of particle–fluid thermal coupling, examining parameters such as heat capacity ratio, injection temperature.

Finally, a comprehensive conclusion is presented, summarizing the main findings and outlining perspectives for future research, while Appendix A provides additional results on the influence of lift force on the stability of bubbly Rayleigh–Bénard systems through modal analysis, which may serve as a useful reference for future work.

1.5 List of notations

Particulate-phase

$\alpha(\boldsymbol{x}, t)$	particle volume fraction
$n(\boldsymbol{x}, t)$	local particle number concentration
$N(t)$	total number of particles
$\mathbf{w}(\boldsymbol{x}, t)$	particle velocity field
$\mathbf{w}_T$	terminal velocity
$T_p(\boldsymbol{x}, t)$	particle-phase temperature
ρ_p	particle density
c_{Pp}	particle specific heat capacity
d_p	particle size (diameter)
V_p	volume of the single particle
$\mathbf{n}$	unit normal vector

Fluid-phase

$\mathbf{u}(\boldsymbol{x}, t)$	part velocity field
$T(\boldsymbol{x}, t)$	fluid-phase temperature
ρ	fluid density
c_p	fluid specific heat capacity
V_f	fluid volume
V	reference volume
$\mathbf{g}$	gravitational force
μ	dynamic viscosity
ν	kinematic viscosity
κ	thermal diffusivity
β_T	thermal expansion coefficient

Dimensionless Numbers

Re_p	particle Reynolds number
Re_s	shear Reynolds number
Re	Reynolds number
St	Stokes number
Nu	Nusselt number
Pr	Prandtl number
Ga	Galileo number
Θ	fluid temperature
Θ_p	particle temperature
$\mathbf{U}$	fluid velocity
$\mathbf{W}$	particle velocity
$\mathbf{W}_T$	terminal velocity
Φ	particle diameter
τ_p	particle viscous response time
τ_T	particle thermal response time
β	fluid to particle density ratio
E	particle to fluid volumetric heat capacity ratio
ϵ	particle to fluid specific heat capacity ratio
E_Θ	Total thermal energy
E_k	Total kinetic energy

Part I

Mathematical Modeling

Chapter 2

Modelization of disperse multiphase flows

Outline of the current chapter

In this chapter, we discuss the modeling strategies and governing equations that form the theoretical foundation of the particulate Rayleigh–Bénard (pRB) model, which is derived at the end of the chapter. Its outline is summarized as follows: Section 2.1 reviews different approaches to describe disperse two-phase flows, including Eulerian formulations. Section 2.2 establishes the governing equations for the particulate phase. In Section 2.3, we present the two-fluid formulation of dispersed two-phase flows in Eulerian framework, covering mass, momentum and energy conservation. Finally, Section 2.4 introduces the particulate Rayleigh–Bénard (pRB) model system, including a detailed description of the model.

2.1 Different modeling strategies

The modeling of dispersed particulate multiphase flows has evolved through three dominant modeling strategies: (i) treating both the fluid and the particulate phases as continuous fields (Eulerian-Eulerian), (ii) combining a continuum representation for the fluid phase with a discrete point-like modelization tracking approach for particles (Eulerian-Lagrangian), or (iii) treating particles as solid bodies advected by the flow, fully resolving the hydrodynamic interactions around each particle (fully resolved or particle-resolved approaches). Figure 2.1 illustrates these three approaches. These methodologies have found extensive application in sedimentation, fluidized beds, hydraulic fracturing, slurry transport, and aerosol dynamics ([43], [44], [45], [46], [47]).

2.1.1 Eulerian description

The field-based approach, also known as the Eulerian description, is widely used for investigating particle-laden flows and provides a robust computational framework when the particulate phase can be treated as a continuum. Its applicability relies on two main conditions: (i) there must be a sufficiently large number of particles within the reference volume to define meaningful averaged fields, and (ii) the volume fraction of particles should remain relatively low, so that particle–particle interactions do not dominate the flow. Typically, this approach is valid for dilute to moderately dense suspensions, with particle volume

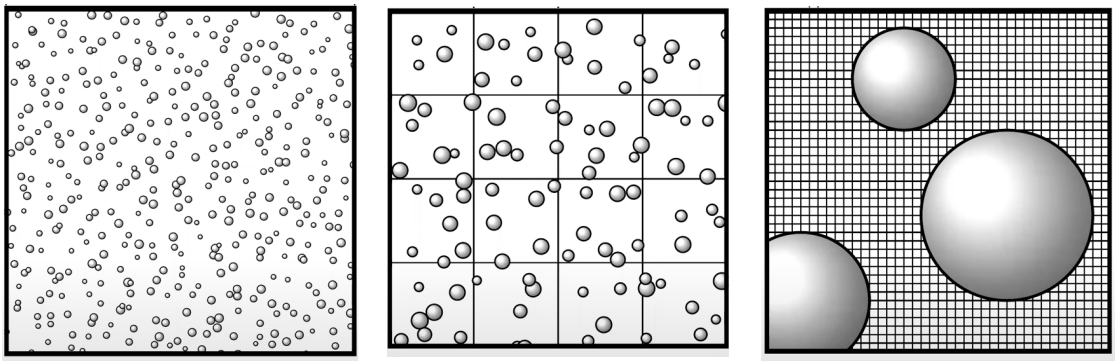

(a) Euler-Euler (b) Euler-Lagrange (c) Fully resolved

Figure 2.1: Scheme illustrating the different modeling approaches for dispersed multiphase flows.

fractions less than 0.1% [88, 170] as shown in figure 2.2, where the continuum assumption for the dispersed phase holds and the Eulerian description accurately captures the averaged particle dynamics. Beyond these ranges, discrete or particle-resolved simulations are generally required to account for strong inter-particle interactions and localized effects.

In this approach, the dispersed and carrier phases are modeled as continua, interpenetrating media that are coupled through interphase exchange terms.

The two-phase Eulerian–Eulerian model, when applied to particle–fluid dynamics, offers a rigorous approach to understanding and predicting the complex behavior of these two-phase systems. Fundamentally, the Eulerian–Eulerian model relies on the conservation of mass, momentum, and energy for each phase within the particle-suspended system.

This approach is particularly well-suited for analyzing phase segregation, entrainment, and phase inversion, providing insights critical for engineering applications such as fluidized beds [153], sediment transport and submarine landslides [154], and heat transfer optimization [155]. By solving governing equations simultaneously for both phases, the Eulerian-Eulerian model effectively captures interparticle interactions and momentum exchange however particle particle interactions can not be modeled. A key advantage of this approach is its suitability for linear stability analysis, which has played a foundational role in understanding the dynamics of multiphase systems. Classical investigations,

such as the pioneering work of Saffman on the stability of laminar flow in dusty gases [144], were among the first to demonstrate how suspended particles can both dampen or destabilize flow instabilities, depending on particle-to-fluid response time. Building on these theoretical foundations, Prosperetti's contributions [169] further strengthen this evolution, offering theoretical insights into multiphase stability and dynamics, especially relevant to particulate multiphase flows. Moreover, recent works have adapted stability analysis to modern particle-laden and continuum frameworks, enabling detailed explorations of particle–feedback mechanisms in contemporary flow systems. For instance, Prakhar et al. [50] present a sophisticated modeling approach for particulate Rayleigh Bèrnard problem.

2.1.2 Lagrangian description

The principle of Euler-Lagrange models is to describe the continuous phase (liquid or gas) in an Eulerian manner and to ensure Lagrangian tracking of the dispersed phase (particles). The latter means that individual particles are followed in their frames of reference (meshless). This method is widely used in pollutant dispersion, sprays, and sediment transport, where particle inertia plays a crucial role [149, 151, 150, 152].

The Eulerian-Lagrangian approach can be applied under different assumptions. In some problems, it is reasonable to suppose that the particles do not alter the flow field. Following that, the solution entails tracking the particle paths inside a specified/known velocity field [156]. This type of coupling configuration is well known and described as one-way coupling as shown in figure (2.2). In some other problems, the particle has enough momentum to disturb the surrounding flow. In this scenario, the feedback effect from the particle momentum must be added into the fluid phase. However, the particle concentration in comparison to the fluid concentration may still be negligible [157]. In fact, in the fully coupled system, the higher particle concentration is considered, including feedback from the particulate phase, but the particles are assumed sufficiently dispersed so that particle collisions are infrequent, referred to as two-way coupling (see fig. 2.2). When particulate volume fractions exceed 5%, particle collision frequen-

cies are significant and should be taken into consideration. The interparticle stress resulting from collisions in the Eulerian/Lagrangian technique for dense particulate flows cannot be resolved by Lagrangian collision computations. The latter discussed case is also known as a four-way coupling, where inter-particle forces are also taken into account.

Linear stability analysis within this framework is more challenging due to the inherent need for statistical averaging of particle distributions, making it less preferable than the Eulerian-Eulerian model for theoretical stability studies.

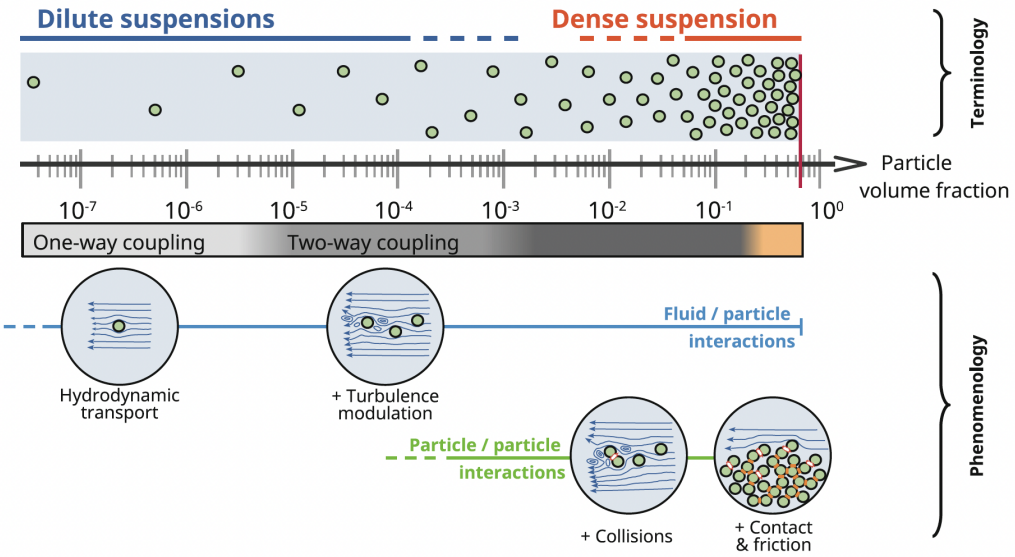

Figure 2.2: Schematic of different coupling regimes in particle-laden flows, using particle volume fraction as an indicator. As concentration increases from dilute to dense suspensions, fluid–particle coupling shifts from one-way to two-way, with inter-particle interactions (four-way coupling) becoming dominant at high loadings. Figure taken from [15].

2.1.3 Fully/particle resolved

Particle-resolved simulations directly describe the flow around each individual particle without need of modeling beyond local conservation equations and boundary conditions. Unlike continuum-based models, these simulations resolve fine-scale interactions such as boundary layers and wakes around the

particles and provide unparalleled accuracy in flows where local particle effects are significant. This approach has proven essential in studies involving turbulent suspensions, microfluidic particle transport, and Rayleigh-Bénard convection laden with solid inclusions [160, 159, 137]. Although the method offers significant advantages, it also comes with notable drawbacks. For example, the computational cost of the method is always a concern because each particle must be resolved with sufficient grid points, which results in rapid cost growth with particle size ratio and number of particles. This limits the number of particles that can be simulated and becomes non-feasible for full-scale engineering systems (such as fluidized beds and pollutant dispersion). Apart from the limited scalability, parametric restrictions, and tackling complex geometries these present a significant challenge in adoption of this method.

Various computational techniques have been developed to enable particle-resolved simulations. These approaches are broadly divided into two classes: body-fitted and fictitious domain methods. In body-fitted methods (see fig. 2.3), the computational mesh conforms to the particle surface but comes at the cost of complex and often expensive mesh generation and adaptation. Examples include unstructured body-conformal meshes based on finite volume or finite element discretizations, Arbitrary Lagrangian–Eulerian (ALE) formulations [168]. In contrast, fictitious domain methods (see fig. 2.3) embed the particle within a fixed Cartesian grid and impose the boundary conditions through additional constraints. Among these, the immersed boundary method (IBM) [55, 165, 164] is widely used, where forcing terms are introduced into the Navier–Stokes equations to represent the effect of the particle surface. Alternative fictitious domain strategies rely on penalization techniques [166], which impose particle-induced constraints through modified governing equations, offering a flexible and computationally efficient way to handle complex particle–fluid interactions.

Beyond these approaches, the lattice Boltzmann method (LBM) [56, 167] provides a mesoscopic framework for simulating the continuum fluid phase. In particle-resolved simulations, the particle–fluid coupling is achieved through the enforcement of boundary conditions at the particle surface and the evaluation of hydrodynamic forces and torques. This treatment is conceptually different from IBM or penalization strategies and has been extensively developed in the work of

Aidun and collaborators [167], while the Physalis method [57] employs spectral techniques for high-resolution computations. The main idea in this methodology is to exploit the analytical solution of the Stokes equations near each particle, where a truncated series of spherical harmonics can represent the flow. In order to ensure accuracy close to the particle boundary and computational efficiency in the bulk flow. Recent advancements, such as adaptive mesh refinement and parallel computing, have expanded the feasibility of these simulations, making them viable for increasingly complex systems [58, 59, 35].

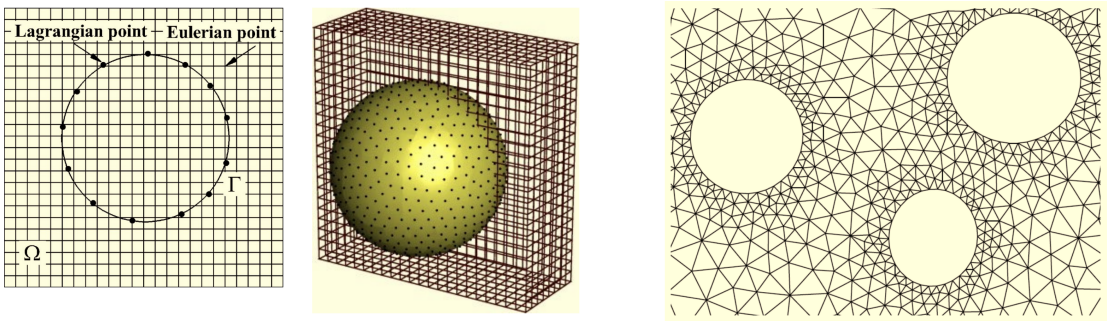

Fictitious domain Body fitted

Figure 2.3: Schematic representation of two classes of computational approaches for particle-resolved simulations: (left) Fictitious domain methods, where the particle is embedded in a fixed grid and (right) Body-fitted methods, where the computational mesh conforms to the particle surface, allowing exact enforcement of boundary conditions.

2.2 Governing equations for the particulate phase

In the following section we will present the equations of motion for the particulate phase, together with the coupling to the fluid ones, that we will use in the rest of this thesis. The particulate phase is described through its own macroscopic field variables, namely the particle volume fraction $\alpha(\mathbf{x}, t)$, the particle velocity field $\mathbf{w}(\mathbf{x}, t)$ and the particle-phase temperature $T_p(\mathbf{x}, t)$. These fields are complemented by the intrinsic material properties of the particles, such as their density ρ_p and specific heat capacity c_{Pp} and also by their geometric properties, such as the particle size. Together, these quantities provide the basis

for formulating the conservation equations of mass, momentum, and energy for the dispersed phase.

2.2.1 Particulate phase continuity equation

Conservation of local particle number concentration $n(\boldsymbol{x}, t)$ in an arbitrary reference volume (V) is expressed by [60]

$$\partial_t \int_V n dV + \int_S n\mathbf{w} \cdot \mathbf{n}\, dS = 0, \tag{2.1}$$

where $\mathbf{n}$ is an outwardly directed unit vector normal to the surface element dS and $\mathbf{w}$ is particle velocity. Using Gauss divergence theorem, we convert the surface integral to a volume integral,

$$\int_V (\partial_t n + \nabla \cdot (n\mathbf{w}))dV = 0, \tag{2.2}$$

in view of the arbitrariness of volume V , we deduce

$$\partial_t n + \nabla \cdot (n\mathbf{w}) = 0, \tag{2.3}$$

which can be recast in term of the volumetric density $\alpha = nV_p$, with V_p volume of a single particle.

$$\partial_t \alpha + \nabla \cdot (\alpha\mathbf{w}) = 0. \tag{2.4}$$

2.2.2 Particulate phase momentum equation

The study of the motion of a rigid sphere in a viscous fluid has a long history. Stokes first obtained the steady drag law for a small sphere moving slowly through a viscous medium, valid in the creeping flow regime [163]. Subsequently, Boussinesq, Oseen, and Basset extended the analysis to account for the motion of a sphere settling out under gravity in a fluid that was otherwise at rest ([61], [62], [63]). The disturbance flow produced by the motion of the sphere was assumed to have sufficiently low Reynolds number so that the fluid force on the sphere could be calculated from the results of unsteady Stokes flow. Here, the relevant Reynolds number is the particle Reynolds number based on the slip velocity,

defined as

$$Re_p = \frac{\rho d_p |\mathbf{u} - \mathbf{w}|}{\mu} = \frac{d_p |\mathbf{u} - \mathbf{w}|}{\nu},$$

with d_p the sphere diameter, ρ the fluid density, μ the dynamic viscosity, and $\nu = \mu/\rho_f$ the kinematic viscosity. The unsteady Stokes approximation requires $Re_p \ll 1$. When the background flow has significant shear, one also requires a small shear Reynolds number,

$$Re_s = \frac{G d_p^2}{\nu}, \qquad G \equiv \|\nabla \mathbf{u}\|,$$

so that $Re_s \ll 1$ as well.

Tchen extended this work to a sphere settling under gravity in an unsteady and nonuniform flow, with a view to application to turbulent flows [161]. The resulting model (known as BBOT, Basset-Boussinesq-Oseen-Tchen) has been revisited in 1983, simultaneously by Maxey & Riley [64] and by Gatignol [65]. The particle equation of motion derived by Maxey, Riley, and Gatignol (MRG) is considered the most accurate description of the dynamics of a small, rigid, spherical particle in an unsteady and inhomogeneous flow, provided that both the particle Reynolds number and the shear Reynolds number remain small. The MRG formulation also accounts for the non-uniformity of the surrounding flow, incorporating the corrections originally studied by Faxén [162] for non-homogeneous velocity fields.

Apart from the history force (i.e. unsteady Stokes drag) and the Faxén corrections, which are neglected in this study due to their negligible contribution, the governing equation reduces to

$$\frac{d\mathbf{w}}{dt} = \frac{\mathbf{u} - \mathbf{w}}{\tau_p} + \beta \frac{D\mathbf{u}}{Dt} + (1 - \beta)\mathbf{g}, \tag{2.5}$$

where $\mathbf{w}$ is the particle velocity, $\mathbf{u}$ is the carrier flow velocity field, the operator $D\mathbf{u}/Dt$ denotes the material or Lagrangian derivative representing the velocity of the undisturbed fluid velocity and $d\mathbf{w}/dt$ is the particle Lagrangian velocity time derivative. The terms on the right-hand side, left to right, follow as:

- The Stokes drag force, which is due to the relative velocities of particle and

fluid. In the expression above, the drag is parameterized by the viscous response time

$$\tau_p = \frac{d_p^2}{12\nu\beta},$$

where ν is the fluid kinematic viscosity and d_p is the particle diameter.

- The fluid acceleration force with the added mass correction. The added mass force (also known as virtual mass force) intensity by the modified density ratio defined as,

$$\beta = \frac{3\rho}{\rho + 2\rho_p},$$

with ρ the fluid mass density. This force is purely inertial in nature and arises due to the force exerted by the displaced fluid caused by the particle that resists particles acceleration and deceleration. The parameter β that varies in the range [0,3] discriminates between the cases of particles heavier than the fluid, $\beta < 1$, or lighter than the fluid, $\beta > 1$, the limiting cases corresponding respectively to the infinitely heavy (ballistic limit) and infinitely light (which is a good approximation e.g. for air bubbles in water) as shown in figure 2.4. The case $\beta = 1$ is special case which accounts for neutrally buoyant particles.

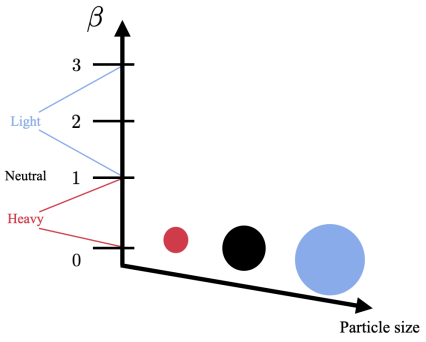

Figure 2.4: Classification of particles based on their modified mass density ratio β.

- The Archimedes force, which is the net force due to gravity and buoyancy.

In this work, we focus on non-Brownian particles, which are sufficiently large

that thermal fluctuations can be neglected. Several studies have also accounted for the lift force acting on particles in a fluid. This force, which is perpendicular to the relative velocity between the particle and the fluid, can originate from two distinct mechanisms. The first arises from velocity gradients in the fluid, giving rise to the shear-induced lift force commonly referred to as the Saffman lift force [128]. The second results from the particle rotation, generating a rotation-induced lift force or Magnus force [171].

In the special case of a particle settling in a still fluid ($\mathbf{u} = \mathbf{0}$), the equation of motion reduces to a balance between the Stokes drag and the effective buoyancy force. At long times, the particle reaches a constant settling velocity, known as the Stokes terminal velocity, given by

$$\mathbf{w_T} = (1-\beta)\tau_p \mathbf{g}.$$

The equation (2.5) is written in the Lagrangian framework, where it describes the motion of a single particle. From the mathematical point of view, this is an ordinary differential equation (ODE) since the velocity $\mathbf{w}$ is expressed as a function of time only.

If we instead reformulate the problem in the Eulerian framework, the velocity is no longer associated with a single particle trajectory, but becomes a velocity field $\mathbf{w}(\mathbf{x}, t)$ that depends on both space and time. Consequently, the ordinary time derivative must be replaced by the material (or convective) derivative, which accounts for both local and advective changes. This transformation turns the original ODE into a partial differential equation (PDE).

In other words, in a field description, the ordinary time derivative following each particle in the Lagrangian picture is replaced by the convective derivative. Thus, in the Eulerian framework, the particle momentum equation (2.5) takes the form:

$$\partial_t \mathbf{w} + \mathbf{w} \cdot \nabla \mathbf{w} = \beta \frac{D\mathbf{u}}{Dt} + \frac{\mathbf{u} - \mathbf{w}}{\tau_p} + (1-\beta)\mathbf{g}. \tag{2.6}$$

2.2.3 Particulate phase energy equation

By using the first law of thermodynamics and considering the particle temperature in lumped capacitance approximation which assumes that each particle has a spatially uniform temperature at any given time [66]. It is valid when the particle is small or has high thermal conductivity, so that internal heat conduction is much faster than heat exchange with the fluid. This simplifies the thermal modeling by treating the particle temperature as time-dependent only. Finally, we write the energy balance equation for the particulate phase as

$$\frac{dT_p}{dt} = \frac{-Q_p}{m_p c_{Pp}}, \tag{2.7}$$

where c_{Pp} is the specific heat of the particle and T_p is the particle temperature. here Q_p is the heat transferred by particles to fluid is given by

$$Q_p = \pi d_p^2 h_p (T_p - T).$$

Here, the heat transfer coefficient h_p is obtained from a standard correlation for the Nusselt number of a sphere ([68, 69]):

$$Nu_p = \frac{d_p h_p}{k},$$

with k denoted the the thermal conductivity. Based on the above equation, a temperature relaxation time defined as:

$$\tau_T = \frac{d_p^2 E}{12\kappa},$$

where, $E = \rho_p c_{Pp}/(\rho c_P)$, with c_P and c_{Pp} representing the fluid and particle specific heat capacity respectively, at constant pressure.

After substituting this expression in equation (2.7) and simplifying, we obtain:

$$\frac{dT_p}{dt} = \frac{T - T_p}{\tau_T}. \tag{2.8}$$

Furthermore, by adopting the same analogy used in the previous section for

the particle momentum equation, the ordinary time derivative following each particle in the Lagrangian description is replaced by the convective derivative of the particulate fields. Accordingly, in the Eulerian framework, the particle energy equation can be written as:

$$\partial_t T_p + \mathbf{w} \cdot \nabla T_p = \frac{T - T_p}{\tau_T}. \tag{2.9}$$

2.3 Governing equations of dispersed two-phase flows

Now that we have introduced the equations describing the particulate phase in the Eulerian framework, we turn to the fluid phase. The fluid is modeled as an incompressible Newtonian fluid governed by the Navier–Stokes equations. In the presence of density variations due to temperature, the Boussinesq approximation is employed to account for buoyancy effects. This sets the stage for deriving the complete set of equations governing the dispersed two-phase flow.

2.3.1 Two-fluid mass conservation

We consider a system containing fluid and particles having total volume V as shown in Fig. 2.5. The domain volume V is taken to be fixed in time; variations in the total number of particles $N(t)$ may occur due to particles crossing the external boundary. The volume of the fluid is V_f and the volume of one particle is V_p. The total number of particles is given by

$$N(t) = \int_V n(\mathbf{x}, t)\, dV, \tag{2.10}$$

where $n(x,t)$ denotes the local particle number concentration. Thus, the total volume V of the domain consists of the fluid volume V_f and the volume occupied by particles, giving

$$V = V_f + N V_p = V_f + V_p \int_V n\, dV. \tag{2.11}$$

Introducing the relation for the dispersed phase volume fraction (α) , the above expression can be written as

$$V = V_f + \int_V \alpha \, dV.$$

The total mass of the system is given by

$$m = m_f + m_p = \int_V \Big[(1-\alpha)\rho + \alpha\rho_p\Big] \, dV, \tag{2.12}$$

where ρ and ρ_p are the fluid and particle densities, respectively.

To derive the local form of mass conservation, we apply the Reynolds Transport Theorem (RTT), which relates the time derivative of an integral over a control volume to a local, pointwise formulation:

$$\frac{d}{dt}\int_V \phi \, dV = \int_V \frac{\partial \phi}{\partial t} \, dV + \int_{\partial V} \phi \, \mathbf{u} \cdot \mathbf{n} \, dA, \tag{2.13}$$

where ϕ is a scalar field, $\mathbf{u}$ is the velocity, and $\mathbf{n}$ is the outward normal at the control surface.

Applying this to the total mass expression and using the divergence theorem, we obtain the local mass conservation equation for the fluid phase in the Eulerian–Eulerian framework with spatially particle varying volume fraction $\alpha(\mathbf{x}, t)$:

$$\frac{\partial[(1-\alpha)\rho]}{\partial t} + \nabla \cdot [(1-\alpha)\rho \, \mathbf{u}] = 0.$$

similarly for the particulate-phase we write:

$$\frac{\partial(\alpha\rho_p)}{\partial t} + \nabla \cdot (\alpha\rho_p \, \mathbf{w}) = 0.$$

In the limit of the point-particle model, where the particle volume fraction is negligible, i.e., $\alpha \to 0$, the fluid-phase equation reduces to the standard single-phase fluid continuity equation:

$$\frac{\partial \rho}{\partial t} + \nabla \cdot (\rho \mathbf{u}) = 0,$$

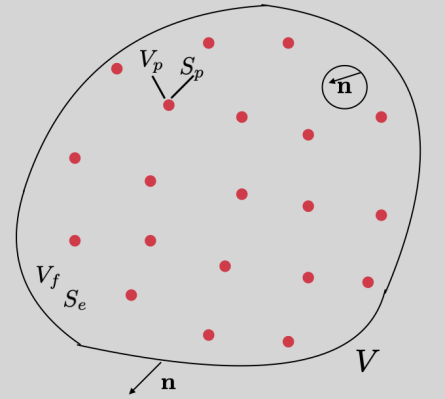

Figure 2.5: Illustration of a control volume V containing a fluid phase and suspended particles.

since in this work we consider the carrier fluid to be incompressible (i.e. with constant density ρ), the above relation reduces to

$$\nabla \cdot \mathbf{u} = 0, \tag{2.14}$$

which expresses the divergence-free condition on the velocity field.

2.3.2 Two-fluid momentum conservation

In the two-fluid model, the conservation of momentum governs the interaction between the fluid and dispersed phases, treating each as a continuum while incorporating interphase momentum exchange [70, 71, 72]. As adapted perviously in mass conservation we have $V = V_f + N V_p$. The flow is contained by the particle surface S_p and the external surface S_e as shown previously in figure 2.5.

The conservation of momentum for the fluid phase within the control volume V_f is expressed as:

$$\int_{V_f} \rho \frac{D\mathbf{u}}{Dt} dV = \int_{S_e} \boldsymbol{\sigma} \cdot \mathbf{n} dS + \int_{S_i} \boldsymbol{\sigma} \cdot \mathbf{n} dS + \int_{V_f} \rho \mathbf{g} dV, \tag{2.15}$$

where ρ is the fluid density, $\mathbf{u}$ is the velocity field, $\boldsymbol{\sigma}$ is the stress tensor, and $\mathbf{g}$ represents the gravitational acceleration. The first term on the right-hand side accounts for surface forces acting on the external boundary S_e, while the second

term captures the interfacial forces between the fluid and dispersed phase over S_i.

Similarly, the momentum equation for the dispersed phase, considering a finite number of particles, is given by:

$$\int_V \alpha\rho_p \frac{d\mathbf{w}}{dt}\, dV = -\int_{S_i} \boldsymbol{\sigma}\cdot\mathbf{n}\, dS + \int_V \alpha\rho_p \mathbf{g} dV, \tag{2.16}$$

where ρ_p is the particle density, $\mathbf{w}$ represents the particle velocity, and α denotes the volume fraction of the dispersed phase. The left-hand side accounts for the rate of change of momentum within the dispersed phase, while the right-hand side includes surface forces at the fluid-particle interface and body forces such as gravity.

Further by adding equation (2.15) and (2.16) the general integral-form momentum balance for the fluid-particle phases can be written as,

$$\int_{V_f} \rho\frac{D\mathbf{u}}{Dt}\, dV + \int_V \alpha\rho_p \frac{d\mathbf{w}}{dt}\, dV = \int_{S_e} \sigma\cdot\mathbf{n}\, ds + \int_{V_f} \rho\mathbf{g}\, dV + \int_V \rho_p dV, \tag{2.17}$$

adding $\int_V \alpha\rho\frac{D\mathbf{u}}{Dt} dV$ both side of the equation, we get

$$\int_V \rho\frac{D\mathbf{u}}{Dt}\, dV + \int_V \alpha\rho_p \frac{d\mathbf{w}}{dt}\, dV = \int_V \alpha\rho\frac{D\mathbf{u}}{Dt} dV + \int_{S_e} \sigma\cdot\mathbf{n}\, ds + \int_{V_f} \rho\mathbf{g}\, dV + \int_V \alpha\rho_p dV, \tag{2.18}$$

again by adding $\int_V \alpha\rho\mathbf{g} dV$ both side of the equation, we get

$$\int_V \rho\frac{D\mathbf{u}}{Dt}\, dV + \int_V \alpha\rho_p \frac{d\mathbf{w}}{dt}\, dV + \int_V \alpha\rho\mathbf{g}\, dV = \int_V \alpha\rho\frac{D\mathbf{u}}{Dt}\, dV + \int_{S_e} \boldsymbol{\sigma}\cdot\mathbf{n}\, ds + \int_V \rho\mathbf{g}\, dV + \int_V \alpha\rho_p\, dV, \tag{2.19}$$

by using Gauss divergence theorem we convert the surface integral into volume

integral the above equation simplifies to,

$$\int_V \rho \frac{D\mathbf{u}}{Dt}\, dV + \int_V \alpha\rho_p \frac{d\mathbf{w}}{dt}\, dV = \int_V \alpha\rho \frac{D\mathbf{u}}{Dt}\, dV + \int_V \nabla\cdot\sigma\, dV + \int_V \rho\mathbf{g}\, dV + \int_V \alpha\rho_p\, dV - \int_V \alpha\rho\mathbf{g}\, dV, \quad (2.20)$$

rearranging and simplifying the above equation,

$$\int_V \rho \frac{D\mathbf{u}}{Dt}\, dV = \int_V \alpha\rho \frac{D\mathbf{u}}{Dt}\, dV + \int_V \nabla\cdot\sigma\, dV + \int_V \rho\mathbf{g}\, dV + \int_V \alpha\rho_p\, dV - \int_V \alpha\rho\mathbf{g}\, dV - \int_V \alpha\rho_p \frac{d\mathbf{w}}{dt}\, dV, \quad (2.21)$$

using the arbitrariness of the volume we get,

$$\rho \frac{D\mathbf{u}}{Dt} = \nabla\cdot\sigma + \rho\mathbf{g} + \alpha\left[\rho\left(\frac{D\mathbf{u}}{Dt} - \mathbf{g}\right) + \rho_p\left(\mathbf{g} - \frac{d\mathbf{w}}{dt}\right)\right], \quad (2.22)$$

following the standard Boussinesq procedure we set $\rho = \rho[1 - \beta(T - T_r)]$, we conclude

$$\partial_t\mathbf{u} + \mathbf{u}\cdot\nabla\mathbf{u} = \frac{-\nabla p}{\rho} + \nu\nabla^2\mathbf{u} + [1 - \beta(T - T_r)]\mathbf{g} + \alpha\left[\left(\frac{D\mathbf{u}}{Dt} - \mathbf{g}\right) + \frac{\rho_p}{\rho}\left(\mathbf{g} - \frac{d\mathbf{w}}{dt}\right)\right]. \quad (2.23)$$

2.3.3 Two-fluid energy conservation

The two-fluid energy conservation equation is a fundamental component in understanding the thermal dynamics of particulate flow systems. It governs the transfer of energy between the fluid and particulate phases, accounting for both convective heat transport and the interaction between the phases. This equation provides insights into how the energy is distributed and exchanged, incorporating the effects of particle flux and heat conduction. The integral form of the energy equation for the fluid phase including the effect of particle is given by [50] is expressed as follows:

$$\int_{V_f} \rho c \frac{DT}{dt} dV = -\int_{S_e} \mathbf{q} \cdot \mathbf{n}\, dS + \int_V \alpha Q_p\, dV, \tag{2.24}$$

with c the fluid specific heat and Q_p is the heat transfer by the particles to the fluid or which we assume the form

$$Q_p = \pi d_p^2 h_p (T_p - T).$$

Similarly, the particulate equation can be written as,

$$\int_V \alpha \rho_p c_p \frac{dT_p}{dt} dV = -\int_V \alpha Q_p\, dV, \tag{2.25}$$

here, the particle temperature is modeled using the lumped-capacitance approximation, assuming spatially uniform temperature within each particle. This is valid for small or highly conductive particles, where internal conduction is fast compared to external heat exchange.

By adding equation (2.24) and (2.25) the general integral-form energy balance for the two-fluid model can be written as,

$$\int_{V_f} \rho c \frac{DT}{Dt} dV + \int_V \alpha \rho_p c_p \frac{dT_p}{dt} dV = -\int_{S_e} \mathbf{q} \cdot \mathbf{n}\, dS, \tag{2.26}$$

Using $\int_{V_f}(\cdot)\, dV = \int_V (1-\alpha)(\cdot)\, dV$ we write

$$\int_V (1-\alpha) \rho c \frac{DT}{Dt} dV + \int_V \alpha \rho_p c_p \frac{dT_p}{dt} dV = -\int_{S_e} \mathbf{q} \cdot \mathbf{n}\, dS, \tag{2.27}$$

adding $\int_V \alpha \rho c \frac{DT}{Dt} dV$ to both sides yields

$$\int_V \rho c \frac{DT}{Dt} dV + \int_V \alpha \rho_p c_p \frac{dT_p}{dt} dV = -\int_{S_e} \mathbf{q} \cdot \mathbf{n}\, dS + \int_V \alpha \rho c \frac{DT}{Dt} dV, \tag{2.28}$$

by rearranging the above equation we get,

$$\int_V \rho c \frac{DT}{Dt} dV = -\int_{S_e} \mathbf{q} \cdot \mathbf{n} dS + \int_V \alpha \rho c \frac{DT}{Dt} dV - \int_V \alpha \rho_p c_p \frac{dT_p}{dt} dV, \tag{2.29}$$

By using Gauss Divergence theorem the we convert the surface integral into volume integral the above equation simplifies to,

$$\int_V \rho c \frac{DT}{Dt} dV = -\int_V \nabla \cdot \mathbf{q} dV + \int_V \alpha \rho c \frac{DT}{Dt} dV - \int_V \alpha \rho_p c_p \frac{dT_p}{dt} dV, \tag{2.30}$$

using the arbitrariness of the volume we get,

$$\rho c \frac{DT}{Dt} = -\nabla \cdot \mathbf{q} + \alpha \left[\rho c \frac{DT}{Dt} - \rho_p c_p \frac{dT_p}{dt} \right], \tag{2.31}$$

substituting the particulate temperature expression from equation (2.9) we get,

$$\rho c \frac{DT}{Dt} = -\nabla \cdot \mathbf{q} + \alpha \left[\rho c \frac{DT}{Dt} - \rho_p c_p \frac{T - T_p}{\tau_T} \right], \tag{2.32}$$

further after using Fourier's law for heat flux vector

$$\mathbf{q} = -k \nabla T,$$

with k the thermal conductivity of the fluid the equation (2.32) yields two-fluid energy equation,

$$\partial_t T + \mathbf{u} \cdot \nabla T = \kappa \nabla^2 T + \alpha \frac{DT}{Dt} - \alpha E \frac{T - T_p}{\tau_T}. \tag{2.33}$$

Here, κ is the thermal diffusivity.

2.4 Particulate Rayleigh-Bénard (pRB) model system

2.4.1 Model description

As we have already mentioned, in this study we adopt an Eulerian model system for the description of the dynamics of a non-Brownian suspension of particles in the Rayleigh-Bénard (RB) setting. The particle volume concentration is assumed small everywhere so that the fluid can be considered incompressible and described by the conventional Boussinesq system of equations for the fluid velocity field $\mathbf{u}(\boldsymbol{x},t)$ and its temperature $T(\boldsymbol{x},t)$. However, due to the total conservation of momentum and thermal energy, the particulate phase can exert on the fluid both mechanical and thermal feedbacks. The particulate phase is characterized by the individual particle material properties, the mass density ρ_p, particle diameter d_p, specific thermal capacity (at constant pressure) c_p, and by the fields of volume concentration $\alpha(\boldsymbol{x},t)$, velocity $\mathbf{w}(\boldsymbol{x},t)$ and temperature $T_p(\boldsymbol{x},t)$.

In summary, the conservation equations of mass, momentum and heat for the fluid and particle phases read as follow:

$$0 = \nabla\cdot\mathbf{u}, \tag{2.34}$$

$$0 = \frac{d\alpha}{dt} + \alpha(\nabla\cdot\mathbf{w}), \tag{2.35}$$

$$\frac{D\mathbf{u}}{Dt} = \frac{-\nabla p}{\rho} + \nu\nabla^2\mathbf{u} + [1-\beta_T(T-T_r)]\mathbf{g} + \alpha\left[\left(\frac{D\mathbf{u}}{Dt}-\mathbf{g}\right) + \frac{\rho_p}{\rho}\left(\mathbf{g}-\frac{d\mathbf{w}}{dt}\right)\right], \tag{2.36}$$

$$\frac{d\mathbf{w}}{dt} = \beta\frac{D\mathbf{u}}{Dt} + \frac{\mathbf{u}-\mathbf{w}}{\tau_p} + (1-\beta)\mathbf{g} + \frac{\beta}{3}[(\mathbf{u}-\mathbf{w})\times(\nabla\times\mathbf{u})], \tag{2.37}$$

$$\frac{DT}{Dt} = \kappa\nabla^2 T + \alpha\left[\frac{DT}{Dt} - E\frac{T-T_p}{\tau_T}\right], \tag{2.38}$$

$$\frac{dT_p}{dt} = \frac{T-T_p}{\tau_T}. \tag{2.39}$$

Some observations are in order. First, $\frac{D}{Dt}() = \partial_t() + \mathbf{u}\cdot\nabla()$ denotes the fluid

material derivative, while $\frac{d}{dt}() = \partial_t() + \mathbf{w} \cdot \nabla()$ is the particulate phase material derivative.

As mentioned earlier in detail, we take into account the effect of four main hydrodynamics forces on the particle following the order of appearance on the right-hand side of Eq. (2.37)

- Fluid acceleration force with the added mass correction
- The Stokes drag force
- Buoyancy force
- Lift force.

The drag is parameterized by the viscous response time $\tau_p = \frac{dp^2}{12\nu\beta}$ where ν is the fluid viscosity. The added mass force intensity by the modified density ratio $\beta = 3\rho/(\rho + 2\rho_p)$ with ρ the fluid mass density.

The lift force, whose role can be relevant for bubbles ($\beta = 3$), see e.g. [52]. Third, the temperature inside each particle is assumed constant (lumped approximation) and its relaxation to the equilibrium is given by the timescale $\tau_T = d_p^2 E/(12\kappa)$ with κ the fluid thermal diffusivity and $E = \rho_p c_{Pp}/(\rho c_p)$ with c the fluid specific heat at constant pressure. We note that the parameter E describes the intensity of the thermal coupling between the particulate phase and the fluid (such coupling vanishes in the $E = 0$ limit). The thermophoretic force on the particle is neglected, as normally done for non-Brownian particles. The remaining constants represent the fluid volumetric thermal expansion coefficient β_T at the reference temperature T_r, the gravity vector $\mathbf{g}$ and the pressure field $p(\mathbf{x}, t)$.

The system spatial domain is three-dimensional, confined by two-infinite parallel horizontal walls at coordinates $z = \pm H/2$, with $\hat{\mathbf{z}}$ pointing upwards. The boundaries are no-slip for the fluid velocity ($\mathbf{u} = 0$), and isothermal with a thermal gap of ΔT between them, the bottom wall being the warmest. In this way, when the thermal expansion coefficient of the fluid (β_T) is positive, an unstable density stratification is created. In order to help the reader to visualize the model system a schematic representation is provided in Figure (2.6).

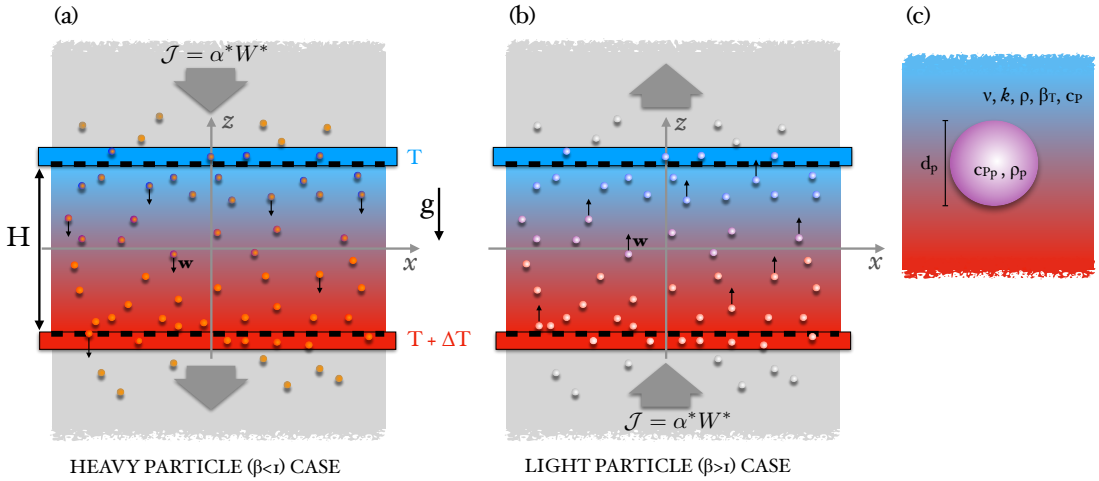

Figure 2.6: Sketch of the particulate Rayleigh-Bènard model system, for the case of heavy (a) and light particles (b). The fluid domain has a height H and is infinitely extended in the horizontal direction. From the stability point of view only one lateral dimension is important, hence the system can be thought and represented as two-dimensional. The horizontal boundaries are isothermal, with the bottom being warmer of $\Delta T > 0$, and no-slip for the fluid velocity. The particles are injected either from top (for heavier than the fluid particles) or from the bottom walls (for light particles) at their prescribed velocity with a prescribed volume flow rate. The overall set of parameters specifying the fluid and particle properties are in indicated in panel (c). They are for the fluid: ν kinematic viscosity, κ thermal diffusivity, ρ mass density, β_T thermal expansion coefficient, c_p the specific heat capacity at constant pressure. For the particle: d_p the diameter, c_{Pp} the specific heat capacity and ρ_p the mass density.

Particles are introduced from one of the boundaries at a constant volumetric flux and with a prescribed velocity $\mathbf{w}^*$, expressed as a multiple of the reference terminal velocity, i.e. $\mathbf{w}_T = (1-\beta)\tau_p\mathbf{g}$. such a velocity can be easily computed by setting uniformly to zero the fluid velocity in Eq (2.37). Particles with $\beta < 1$, hereafter referred to as "heavy particles", are injected from the top boundary, whereas those with $\beta > 1$, i.e. "light particles", are injected from the bottom one.

The particle inlet temperature is also prescribed at a specific value T_p^*. In other words the inlet particle condition is prescribed by a concentration particle flux whose intensity is $\mathcal{J} = \alpha^*\mathbf{w}^*$, and by an analogous thermal flux $\mathcal{J}_T = \alpha^*\mathbf{w}^*T_p^*$. On the other hand, the particle accumulation on the opposite boundary, the *outlet*, is neglected, as if they are removed from the domain as soon as they reach the opposite wall. We note that the corresponding outlet mass and thermal fluxes do not need to match those at the inlet. It is worth noting that the equations governing the particulate-phase are first-order in space, as they lack a dissipation term in the form of a Laplacian. Consequently, only an inlet particulate-phase boundary condition is required to determine their solution.

2.4.2 Dimensionless system

In view of the stability study that we will discuss in forthcoming chapters, it is convenient to adimensionalize the model system in terms of its height ($\mathbf{X} = \mathbf{x}/H$), the corresponding conductive time scale, ($\mathcal{T} = t\kappa/H^2$) and the fluid density ρ. This leads to the introduction of the dimensionless fields:

$$\mathbf{U} = \mathbf{u}\frac{H}{\kappa}, \quad P = \frac{pH^2}{\rho\kappa^2}, \quad \Theta = \frac{T - T_r}{\Delta T}, \quad \mathbf{W} = \mathbf{w}\frac{H}{\kappa}, \quad \Theta_p = \frac{T_p - T_r}{\Delta T},$$

respectively for the fluid velocity, pressure and temperature and for the particulate velocity and temperature. Without any loss of generality we take the reference temperature T_r to be equal to the fixed temperature of the top (cold) wall. Keeping the same notation for the dimensionless material derivatives and the differential operator (∇), and making explicit the particles momentum feedback, equations (2.34)-(2.39) read:

$$
\begin{aligned}
0 &= \nabla\cdot\mathbf{U}, && (2.40)\\
\frac{d\alpha}{d\mathcal{T}} &= -\alpha(\nabla\cdot\mathbf{W}), && (2.41)\\
\frac{D\mathbf{U}}{D\mathcal{T}} &= -\nabla P + Pr\nabla^2\mathbf{U} + PrRa\Theta\hat{\mathbf{z}} + \frac{\alpha}{2}\left[(\beta-1)\left(\frac{D\mathbf{U}}{D\mathcal{T}} + GaPr^2\hat{\mathbf{Z}}\right)\right]\\
&- \frac{\alpha}{2}\left[(3-\beta)\left(12Pr\frac{\mathbf{U}-\mathbf{W}}{\Phi^2} + \frac{(\mathbf{U}-\mathbf{W})}{3}\times(\nabla\times\mathbf{U})\right)\right], && (2.42)\\
\frac{d\mathbf{W}}{d\mathcal{T}} &= \beta\left[\frac{D\mathbf{U}}{D\mathcal{T}} + 12Pr\frac{\mathbf{U}-\mathbf{W}}{\Phi^2} + \left(\frac{(\mathbf{U}-\mathbf{W})}{3}\times(\nabla\times\mathbf{U})\right)\right] - (1-\beta)GaPr^2\hat{\mathbf{Z}}, && (2.43)\\
\frac{D\Theta}{D\mathcal{T}} &= \nabla^2\Theta + \alpha\left(\frac{D\Theta}{D\mathcal{T}} - 12\frac{\Theta-\Theta_p}{\Phi^2}\right), && (2.44)\\
\frac{d\Theta_p}{d\mathcal{T}} &= \frac{12}{E}\frac{\Theta-\Theta_p}{\Phi^2}, && (2.45)
\end{aligned}
$$

In the above equations we have introduced the following dimensionless characteristic parameters:

$$Ra = \frac{\beta_T\Delta T g H^3}{\nu\kappa}, \quad Pr = \frac{\nu}{\kappa}, \quad Ga = \frac{gH^3}{\nu^2}, \quad \Phi = \frac{d_p}{H}, \tag{2.46}$$

where Ra denotes the Rayleigh number, which quantifies the relative strength of thermally induced buoyancy against mechanical and thermal dissipation, Pr the Prandtl number, which characterizes the fluid phase diffusive material properties, and Ga the Galileo number, which represents the balance between gravitational and viscous forces. Although Ga does not depend on the particle properties, it becomes a relevant control parameter whenever the coupling between the particle and the fluid is taken into account. In dimensionless units, the terminal velocity expression is $\mathbf{W}_T = \frac{1-\beta}{\beta}\frac{\Phi^2}{12}GaPr\hat{\mathbf{Z}}$. Along with the modified fluid-to-particle density ratio, β, the volumetric particle inlet flux $\mathcal{J}$, and the inlet velocity and temperatures (W^*, Θ_p^*), they define the full set of control parameters. In total, the model is governed by nine parameters: three associated with the fluid phase (Ra, Pr, Ga) and six with the particulate-phase $(\Phi, \beta, E, \mathcal{J}, W^*, \Theta_p^*)$.

We observe that in the present model system the coupling between the fluid and the particles depends linearly on the local volume fraction α. The particle diameter Φ which controls not just the mechanical coupling but also the thermal coupling. The parameter E, particle to fluid mass specific heat capacity ratio, controls the thermal coupling between the two phases. If $E \to 0$ then $\Theta_p \to \Theta$ meaning that the particle phase

immediately adapts to the temperature of the fluid. In the opposite limit $E \to \infty$ the particles do not change their temperature and act as volume heat sources in the fluid.

In terms of the dimensionless variables the boundary conditions read,

Fluid phase

$$\mathbf{U} = 0; \quad \Theta = 1 \quad \text{at} \quad Z = -\frac{1}{2}, \quad \text{and} \quad \mathbf{U} = 0; \quad \Theta = 0 \quad \text{at} \quad Z = \frac{1}{2}. \tag{2.47}$$

Particulate phase

$$\mathbf{W} = \mathbf{W}^* = W^* \hat{\mathbf{Z}}, \qquad \alpha = \mathcal{J}/\|\mathbf{W}^*\|, \quad \Theta_p = \Theta_p^* \quad \text{at} \quad Z = Z^*, \tag{2.48}$$

where Z^* denotes the location of the inlet horizontal wall. Note that W^* can be either positive or negative, depending on whether the particle is lighter or heavier than the fluid, while the inlet flux $\mathcal{J}$ is defined as always positive.

Part II

Methodology

Chapter 3

Linear stability analysis of particulate Rayleigh Bèrnard (pRB) system

Outline of the current chapter

3.1 Introduction to stability analysis

Stability analysis is a fundamental tool in the study of dynamical systems and continuum mechanics, particularly in order to comprehend how solutions to nonlinear differen-

tial equations behave under small perturbations. In physical systems—such as fluid flows, chemical reactions, population models, and mechanical structures—determining whether a steady state or equilibrium solution is stable can provide deep insights about the long-term behavior of physical systems. The general aim of stability analyses is to find out whether a system, when slightly disturbed from steady state, returns to its original configuration (stable), diverges away (unstable), or remains in a marginal state.

The evolution of such perturbations can reveal the onset of complex phenomena like , pattern formation, oscillations, or bifurcations. In multiphase flow modeling, for example, stability analysis helps in predicting when uniform flow configurations become unstable due to interfacial or interphase interactions, drag effects, or buoyancy-driven instabilities.

Several methods exist for analyzing stability, including energy methods [76, 77], Lyapunov theory [80, 81], Floquet analysis for time-periodic systems [78, 79], and linear stability analysis [73, 74, 75]. Among these, linear stability analysis is the widely adopted method for investigating the behavior of complex systems, especially as a first step in exploring the dynamics of complex systems.

3.2 Linear stability analysis

In general the dynamical system stability is expressed through the nonlinear equations and cannot be solved analytically. For the sake of solution, the nonlinear problem then linearized by a small departure from conductive (or base) state, with the aid of perturbative analysis. This procedure yields an approximate solution of the system under study, which is strictly accurate when the system is at the critical point (i.e. marginal condition). As the system moves away from the critical condition, the accuracy of the solution progressively decreases.

3.2.1 General formalism

It begins with identifying the equilibrium (or fixed) sate where the system remains unchanged. In classical approach, the time evolution is observed by small departure from the conductive state. The system is then linearized by replacing the dependent variable in governing equations by this conductive state superposed with infinitesimal perturbations

$$\xi = \xi_0 + \epsilon \xi'. \tag{3.1}$$

Here, ξ_0 represents the conductive state, ξ' represents the perturbation, and $\epsilon \ll 1$ denotes the amplitude parameter of the perturbation.

In the modal approach, the perturbation is assumed to have a monochromatic wave like behavior in the homogeneous direction, which allows the decomposition of the perturbed quantities in Fourier modes of the form

$$\xi'(X, Y, Z, \mathcal{T}) = \xi_n(Z)\, e^{(ikX + \lambda \mathcal{T})} + c.c., \tag{3.2}$$

where $\xi' = \{\mathbf{U}', \Theta', P', \alpha', \Theta_p', \mathbf{W}'\}$, *c.c.* is the complex conjugate, and ξ_n is the normal mode amplitude varying in the non-homogeneous direction Z. Accordingly to the temporal stability approach, k is the real wave number, and $\lambda = \lambda_r + i\ \lambda_i$, where λ_r is the temporal growth rate of the perturbation and λ_i is its oscillation frequency.

Different thermoconvective structures can be characterized:

- Streamwise disturbances, or longitudinal rolls (LR), are characterized by roll axes parallel to the direction of the main flow, with $k_x = 0$.
- Spanwise disturbance, or Transversal rolls (TR), are characterized by rolls with axis perpendicular to the primary flow, with $k_y = 0$.
- Oblique structures (OS), which are characterized by wavevectors having both nonzero streamwise and spanwise components, i.e., $k_x \neq 0$ and $k_y \neq 0$.

In this study, since there is no main flow, the problem is two-dimensional, and only k_x is considered. The onset of convective instability can be determined through a temporal stability analysis. This approach considers only spatially sinusoidal disturbances, i.e., normal modes with real wave numbers ($k_x \in \mathbb{R}$, $k_y \in \mathbb{R}$) and a complex frequency ($\lambda \in \mathbb{C}$). This relation can be determined by substituting (3.2) into the perturbed linearize equations.

The marginal stability boundary, which separates stable and unstable regions, is defined by the condition $\mathrm{Im}(\lambda) = 0$. At this boundary, the control parameter—for example, the Rayleigh number attains its minimum, referred to as the critical Rayleigh number Ra_c. This instability is typically triggered by a stationary mode, characterized by $\mathrm{Re}(\lambda) = 0$, which corresponds to a pitchfork bifurcation. In the other case, the onset

of convection is induced by an oscillatory mode, where $\lambda_r \neq 0$, characterizing a Hopf bifurcation.

3.3 Linear stability analysis of particulate Rayleigh-Bènard model system

In this section, we employ the linear stability analysis procedure outlined in the previous section, applied to the particulate Rayleigh–Bénard model system developed in Chapter 2.

3.3.1 Conductive state

In order to identify the onset of natural convection in the pRB system, its equilibrium solution must first be defined. The one chosen here is its steady-state with particles settling or rising in a quiescent and conductive fluid. Hence, one can impose

$$\mathbf{U} = 0, \qquad \mathbf{W} = W_0(Z)\hat{\mathbf{Z}}, \qquad \alpha = \alpha_0(Z),$$

$$\Theta = \Theta_0(Z), \qquad \Theta_p = \Theta_{p0}(Z),$$

and re-write equations (2.40)-(2.45) as:

$$D(\alpha_0 W_0) = 0, \tag{3.3}$$

$$W_0 D W_0 = -12 Pr \beta W_0 \Phi^{-2} - (1-\beta) GaPr^2 \hat{\mathbf{Z}}, \tag{3.4}$$

$$0 = -\nabla P_0 + PrRa\Theta_0 \hat{\mathbf{Z}} + \tfrac{\alpha_0}{2}(\beta - 1) GaPr^2 \hat{\mathbf{Z}} + \frac{6\alpha_0 Pr(3-\beta)}{\Phi^2}\mathbf{W}_0 \tag{3.5}$$

$$D^2\Theta_0 - 12\alpha_0 \Phi^{-2}(\Theta_0 - \Theta_{p0}) = 0, \tag{3.6}$$

$$W_0 D\Theta_{p0} = 12(E\Phi^2)^{-1}(\Theta_0 - \Theta_{p0}), \tag{3.7}$$

where D represents the derivative with respect to Z. The steady-state governing equations (3.3)-(3.7), with their respective boundary conditions derived from (2.47) and (2.48), are computed numerically. Particle volume fraction profiles are shown in figure

3.1. It is possible to note that, in general, particle concentration varies with height, except for the special case where particles are injected at their terminal velocity ($W^* = W_T$), which is the case previously studied by [50] and [146]. When particles are introduced at a velocity lower (higher) than their terminal velocity, they accelerate (decelerate) until they reach it. This process leads to an accumulation (rarefaction) of particles near the injection wall, e.g. in the upper region for heavier particles and in the lower region for lighter ones. Finally, for the prescribed particle inflow considered here, reducing the injection velocity increases the volumetric concentration of incoming particles. Hence, smaller inlet velocities lead to a higher amount of particles. Similarly, in Figures 3.2 and 3.3, the base velocity profiles for light and heavy particles, respectively, are presented for varying injection velocities, ranging from sub- to super-terminal regimes. These profiles illustrate how particles either accelerate or decelerate toward their respective terminal velocities. Finally, Figure 3.4 shows the base-state temperature profile for the case of light particles with $\beta = 3$. Note that the pressure base state P_0 is not used in the forthcoming analysis.

3.3.2 Linearization

We now proceed to linearize equations (2.40-2.45) assuming a small departure from the previously calculated base state. According to the standard linear stability approach [3], the dependent vector and scalar fields in the governing equations are constructed as a superposition of the base state and infinitesimal perturbations

$$P = P_0 + \epsilon P', \quad \mathbf{U} = \boldsymbol{U}_0 + \epsilon \boldsymbol{U}', \qquad \Theta = \Theta_0 + \epsilon \Theta', \tag{3.8}$$

$$\alpha = \alpha_0 + \epsilon \alpha', \quad \mathbf{W} = W_0 \hat{\mathbf{Z}} + \epsilon \boldsymbol{W}' \quad \Theta_p = \Theta_{p0} + \epsilon \Theta_p', \tag{3.9}$$

where $\epsilon << 1$, the primed quantities represent the perturbations, and base state fields is denoted by the index zero. Substituting the above relations in the governing equations leads to a following new system of equation at different orders in ϵ.

Fluid-phase

We begin by linearizing the fluid-phase equations, followed by the particulate phase.

$$0 = \nabla \cdot (\boldsymbol{U_0} + \epsilon \boldsymbol{U}'), \tag{3.10}$$

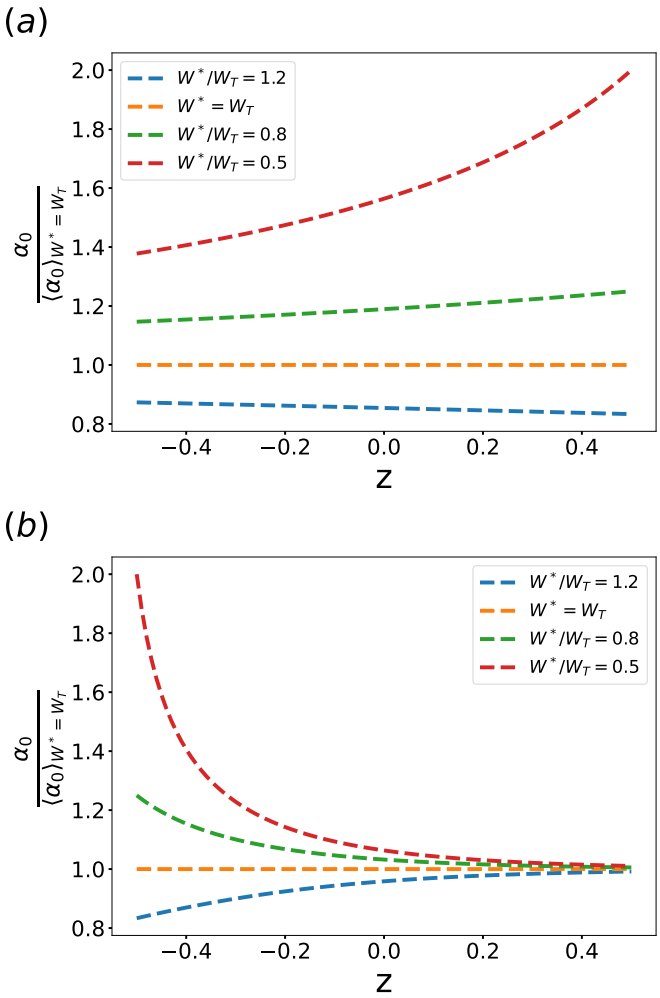

Figure 3.1: Vertical dependence of the steady-state volume concentration field of the particulate-phase, $\alpha_0(Z)$, for different inlet velocities W^* for (a) $\beta = 0.5$ (heavy particles) and $\Theta_p^* = 0$ (b) $\beta = 3$ (bubbles) and $\Theta_p^* = 1$. Data are normalized by the steady-state concentration field corresponding to the case $W^* = W_T$.

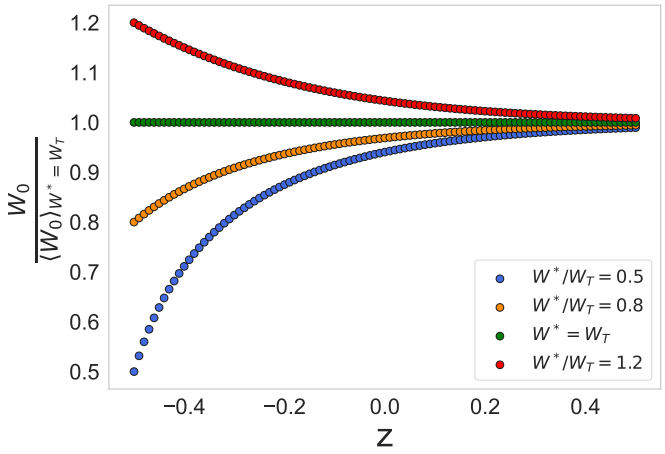

Figure 3.2: Vertical dependence of the base velocity field of the particulate-phase, $W_0(Z)\hat{\mathbf{Z}}$, for different inlet velocities W^* for light particles $\beta = 3$. The particle injection temperature is $\Theta_p^* = 1$ and $E = 5 \times 10^{-3}$. Data are normalized by the base velocity field corresponding to the case $W^* = W_T$.

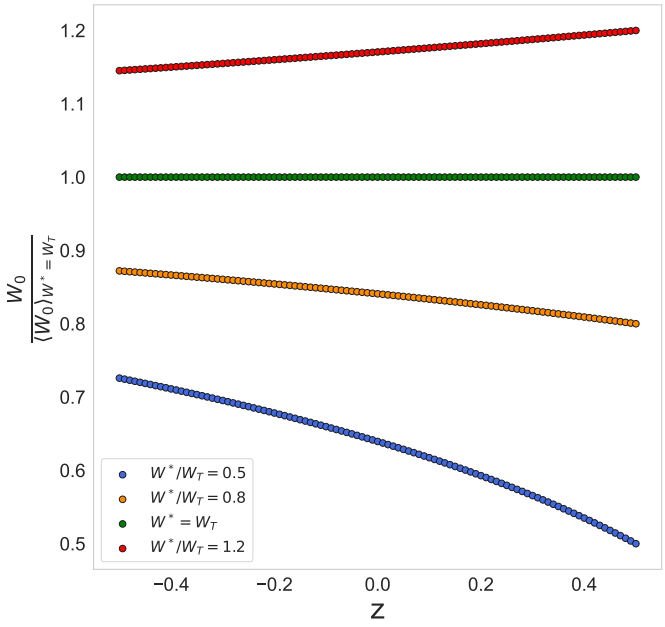

Figure 3.3: Vertical dependence of the base velocity field of the particulate-phase, $W_0(Z)\hat{\mathbf{Z}}$, for different inlet velocities W^* for heavy particles $\beta = 0.5$. The particle injection temperature is $\Theta_p^* = 0$ and $E = 5 \times 10^{-3}$. Data are normalized by the base velcoity field corresponding to the case $W^* = W_T$.

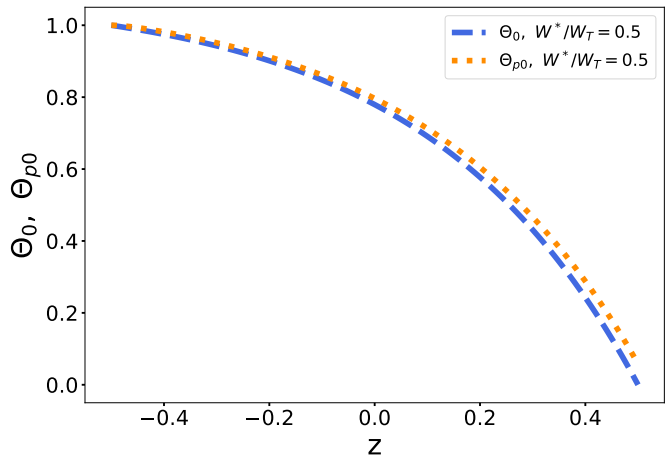

Figure 3.4: The base state fluid and particle temperature vertical distribution in the cell for light particles ($\beta = 3$). The particle injection temperature is $\Theta_p^* = 1$ and $E = 5 \times 10^{-3}$.

$$\partial_{\mathcal{T}}(\boldsymbol{U_0} + \epsilon \boldsymbol{U}') + (\boldsymbol{U_0} + \epsilon \boldsymbol{U}') \cdot \nabla(\boldsymbol{U_0} + \epsilon \boldsymbol{U}') = -\nabla(P_0 + \epsilon P') + Pr\nabla^2(\boldsymbol{U_0} + \epsilon \boldsymbol{U}')$$
$$+ PrRa(\Theta_0 + \epsilon\Theta')\hat{\mathbf{z}} + \frac{(\alpha_0 + \epsilon\alpha')}{2}\Bigg[(\beta - 1)\Bigg((\partial_{\mathcal{T}}(\boldsymbol{U_0} + \epsilon \boldsymbol{U}') + (\boldsymbol{U_0} + \epsilon \boldsymbol{U}') \cdot \nabla(\boldsymbol{U_0} + \epsilon \boldsymbol{U}'))$$
$$+ GaPr^2\hat{\mathbf{Z}}\Bigg) - (3 - \beta)\Bigg(12Pr\frac{(\boldsymbol{U_0} + \epsilon \boldsymbol{U}') - (W_0\hat{Z} - \epsilon \boldsymbol{W}')}{\Phi^2}\Bigg)$$
$$- (3 - \beta)\Bigg(\frac{(\boldsymbol{U_0} + \epsilon \boldsymbol{U}') - (W_0\hat{Z} - \epsilon \boldsymbol{W}')}{3} \times (\nabla \times (\boldsymbol{U_0} + \epsilon \boldsymbol{U}'))\Bigg)\Bigg], \quad (3.11)$$

$$\partial_{\mathcal{T}}(\Theta_0 + \epsilon\Theta') + (\boldsymbol{U_0} + \epsilon \boldsymbol{U}') \cdot \nabla(\Theta_0 + \epsilon\Theta') = \nabla^2(\Theta_0 + \epsilon\Theta')$$
$$+ (\alpha_0 + \epsilon\alpha')\Bigg[\partial_{\mathcal{T}}(\Theta_0 + \epsilon\Theta') + (\boldsymbol{U_0} + \epsilon \boldsymbol{U}') \cdot \nabla(\Theta_0 + \epsilon\Theta')$$
$$- 12\frac{(\Theta_0 + \epsilon\Theta') - (\Theta_{p0} + \epsilon\Theta_p')}{\Phi^2}\Bigg]. \quad (3.12)$$

Upon deducting the base-state relations while keeping the terms of $\mathcal{O}(\epsilon)$ and disregarding higher-order terms in the perturbed quantities, the fluid-phase governing equations at the leading order become,

$$0 = \nabla \cdot \boldsymbol{U}', \tag{3.13}$$

$$\begin{aligned}\partial_{\mathcal{T}} \boldsymbol{U}' = &-\nabla P' + Pr\nabla^2 \boldsymbol{U}' + PrRa\Theta'\hat{\boldsymbol{Z}} + \left(\frac{\beta-1}{2}\right)\alpha_0 \partial_{\mathcal{T}} \boldsymbol{U}' \\ &- \left(\frac{6Pr(3-\beta)}{\Phi^2}\right)(\alpha_0 \boldsymbol{U}' - \alpha_0 \boldsymbol{W}') + \left(\frac{\beta-1}{2} GaPr^2\right)\alpha'\hat{\mathbf{Z}} + \left(\frac{6Pr(3-\beta)}{\Phi^2}\right) W_0 \alpha'\hat{\mathbf{Z}} \\ &- (3-\beta)\frac{\alpha_0 W_0}{6}\omega'\hat{\mathbf{X}},\end{aligned} \tag{3.14}$$

where ω' is the y-component of the fluid perturbation vorticity, $\omega' = (\partial_Z U'_X - \partial_X U'_Z)$.

Pressure elimination:

Further, we eliminate the pressure field from the fluid momentum equation (3.14). This is achieved by taking the double curl of the fluid momentum equation

$$\begin{aligned}\partial_{\mathcal{T}} \nabla^2 \boldsymbol{U}' = &\, Pr\nabla^4 \boldsymbol{U}' - PrRa(\nabla(\partial_Z \Theta') - \nabla^2 \Theta'\hat{\boldsymbol{Z}}) - \frac{\beta-1}{2}(\nabla \times (\nabla \times (\alpha_0 \partial_{\mathcal{T}} \boldsymbol{U}')) \\ &+ \frac{6Pr(3-\beta)}{\Phi^2}\left[\nabla \times (\nabla \times (\alpha_0 \boldsymbol{U}')) - \nabla \times (\nabla \times (\alpha_0 \boldsymbol{W}'))\right] \\ &- \left(\frac{\beta-1}{2} GaPr^2\right)(\nabla(\partial_z \alpha') - \nabla^2 \alpha'\hat{\mathbf{Z}}) - \left(\frac{6Pr(3-\beta)}{\Phi^2}\right)\left[\nabla \times (\nabla \times (W_0 \alpha'\hat{\mathbf{Z}}))\right] \\ &- \frac{3-\beta}{6}\left[\nabla \times (\nabla \times (\alpha_0 W_0 \omega'\hat{\mathbf{X}}))\right],\end{aligned} \tag{3.15}$$

furthermore, we expand the above equation by inserting the relation for double curl and decompose it into its vertical and horizontal fluid velocity components respectively,

$$\begin{aligned}\partial_{\mathcal{T}} \nabla^2 U'_Z = &\, Pr\nabla^4 U'_Z + PrRa\partial_X^2 \Theta' + \frac{\beta-1}{2}\left(d_Z \alpha_0 \partial_{\mathcal{T}} \partial_Z U'_Z + \alpha_0 \partial_{\mathcal{T}} \nabla^2 U'_Z\right) \\ &- \frac{6Pr(3-\beta)}{\Phi^2}\left[\left(d_Z \alpha_0 \partial_Z U'_Z + \alpha_0 \nabla^2 U'_Z\right)\right] \\ &+ \frac{6Pr(3-\beta)}{\Phi^2}\left[\left(\alpha_0 \partial_X^2 W'_z - \alpha_0 \partial_{ZX} W'_X - d_Z \alpha_0 \partial_X W'_X\right)\right] \\ &+ \left(\frac{\beta-1}{2} GaPr^2\right)\partial_X^2 \alpha' + \left(\frac{6Pr(3-\beta)}{\Phi^2}\right) W_0 \partial_X^2 \alpha' \\ &+ \frac{3-\beta}{6}\left[W_0 \alpha_0 \left(\partial_Z^2 \partial_X U'_X - \partial_X^2 \partial_Z U'_Z\right)\right] \\ &+ \frac{3-\beta}{6}\left[\left(\partial_{ZX} U'_X - \partial_X^2 U'_Z\right)\left(\alpha_0 d_Z W_0 + W_0 d_Z \alpha_0\right)\right],\end{aligned} \tag{3.16}$$

$$
\begin{aligned}
\partial_T \nabla^2 U'_X = {} & Pr\nabla^4 U'_X - PrRa\partial_{ZX}\Theta' \\
& + \frac{\beta-1}{2}\Big(2d_Z\alpha_0\partial_T\partial_Z U'_X + \alpha_0\partial_T\nabla^2 U'_X + d_Z\alpha_0\partial_T U'_x\Big) \\
& + \frac{6Pr(3-\beta)}{\Phi^2}\Bigg[\Big(-2d_Z\alpha_0\partial_Z U'_X - U'_X d_Z^2\alpha_0 - \alpha_0\nabla^2 U'_X\Big) \\
& - \Big(\partial_X W'_Z d_Z\alpha_0 + \alpha_0\partial_X W'_X + \alpha_0\partial_Z W'_Z - W'_X d_Z^2\alpha_0 \\
& - 2d_Z\alpha_0\partial_Z W'_X - \alpha_0\partial_X^2 W'_X - \alpha_0\partial_Z^2 W'_X\Big)\Bigg] \\
& - \Big(\frac{\beta-1}{2}GaPr^2\Big)\partial_{ZX}\alpha' - \frac{6Pr(3-\beta)}{\Phi^2}\Big(d_Z W_0\partial_X\alpha' + W_0\partial_{XZ}\alpha'\Big),
\end{aligned}
\tag{3.17}
$$

$$
[1-\alpha_0]\partial_T\Theta' + U'_Z\partial_Z\Theta_0 = \alpha'\partial_T\Theta_0 + \nabla^2\Theta' - 12\alpha_0\frac{(\Theta'-\Theta'_p)}{\Phi^2} - 12\alpha'\frac{(\Theta_0-\Theta_{p0})}{\Phi^2}, \tag{3.18}
$$

Particulate-phase

$$
\partial_T(\alpha_0+\epsilon\alpha') + (W_0\hat{Z}-\epsilon\boldsymbol{W'})\cdot\nabla(\alpha_0+\epsilon\alpha') = -(\alpha_0+\epsilon\alpha')(\nabla\cdot(W_0\hat{Z}-\epsilon\boldsymbol{W'})), \tag{3.19}
$$

$$
\begin{aligned}
\partial_T(W_0\hat{Z}-\epsilon\boldsymbol{W'})\cdot\nabla(W_0\hat{Z}-\epsilon\boldsymbol{W'}) = {} & \beta\left[\partial_T(\boldsymbol{U_0}+\epsilon\boldsymbol{U'}) + (\boldsymbol{U_0}+\epsilon\boldsymbol{U'})\cdot\nabla(\boldsymbol{U_0}+\epsilon\boldsymbol{U'})\right] \\
& + 12Pr\beta\frac{(\boldsymbol{U_0}+\epsilon\boldsymbol{U'})-(W_0\hat{Z}-\epsilon\boldsymbol{W'})}{\Phi^2} \\
& + \beta\left(\frac{(\boldsymbol{U_0}+\epsilon\boldsymbol{U'})-(W_0\hat{Z}-\epsilon\boldsymbol{W'})}{3}\times(\nabla\times(\boldsymbol{U_0}+\epsilon\boldsymbol{U'}))\right),
\end{aligned}
\tag{3.20}
$$

$$
\partial_T(\Theta_{p0}+\epsilon\Theta'_p) + (W_0\hat{Z}-\epsilon\boldsymbol{W'})\cdot\nabla(\Theta_{p0}+\epsilon\Theta'_p) = \frac{12}{E}\left(\frac{(\Theta_0+\epsilon\Theta')-(\Theta_{p0}+\epsilon\Theta'_p)}{\Phi^2}\right), \tag{3.21}
$$

adopting the same procedure as previously presented in fluid-phase the corresponding particle-phase mass, momentum and energy equations respectively become,

$$
\partial_T\alpha' + W_0\partial_Z\alpha' = -\alpha_0(\nabla\cdot\boldsymbol{W'}), \tag{3.22}
$$

the above equation on further expansion becomes,

$$
\partial_T\alpha' = -\Big(\alpha_0\partial_Z + d_Z\alpha_0\Big)W'_Z - \alpha_0\partial_X W'_X - \Big(W_0\hat{\boldsymbol{Z}}\partial_Z + d_Z W_0\Big)\alpha', \tag{3.23}
$$

$$\partial_{\mathcal{T}} \boldsymbol{W}' + \partial_Z \boldsymbol{W}' W_0 \hat{\mathbf{Z}} = \beta \partial_{\mathcal{T}} \boldsymbol{U}' + 12 Pr \beta \frac{(\boldsymbol{U}' - \boldsymbol{W}')}{\Phi^2} + \beta \frac{W_0}{3} \omega' \hat{\mathbf{X}}, \tag{3.24}$$

Subsequently, we decompose the above equation into its vertical and horizontal components, respectively.

$$\partial_{\mathcal{T}} W_Z{}' + W_0 \partial_Z W_Z{}' + W_Z' d_Z W_0 = \beta \partial_{\mathcal{T}} U_Z' + 12 Pr \beta \frac{(U_Z{}' - W_Z{}')}{\Phi^2}, \tag{3.25}$$

$$\partial_{\mathcal{T}} W_X{}' + W_0 \partial_Z W_X{}' = \beta \partial_{\mathcal{T}} U_X' + 12 Pr \beta \frac{(U_X{}' - W_X{}')}{\Phi^2} + \beta \frac{W_0}{3} (\partial_Z U_X' - \partial_X U_Z'), \tag{3.26}$$

$$\partial_{\mathcal{T}} \Theta_p' + W_0 \partial_Z \Theta_p' + W_Z{}' \partial_Z \Theta_{p0} = \frac{12}{E} \frac{\Theta' - \Theta_p'}{\Phi^2}. \tag{3.27}$$

3.3.3 Modal Analysis

In this section, we rewrite the linearized set of equations derived in the previous section in normal mode form. To proceed by adopting the procedure as described in the earlier section (3.2) since coefficients of our equations are constant, the time dependence of the solution will be exponential. So, we can write the perturbation as two-dimensional periodic waves which depend on X and $\mathcal{T}$ as a superposition of terms proportional to $e^{\lambda t}$, with λ eigenvalues to be determined. Again in view of the linearity of the problem, it is sufficient to consider a single one of these terms as the general solution can be obtained by superposition. Therefore we write

$$\boldsymbol{U}' = \boldsymbol{U}^{\boldsymbol{n}}(Z) e^{(ikX + \lambda \mathcal{T})}, \quad \boldsymbol{W}' = \boldsymbol{W}^{\boldsymbol{n}}(Z) e^{(ikX + \lambda \mathcal{T})}, \quad \alpha' = \alpha^n(Z) e^{(ikX + \lambda \mathcal{T})}$$

$$\Theta' = \Theta^n(Z) e^{(ikX + \lambda \mathcal{T})}, \quad \Theta_p' = \Theta_p^n(Z) e^{(ikX + \lambda \mathcal{T})},$$

By substituting the above prescribed transformations into linearized equations and moreover by using the following incompressibility relation in order to eliminate the horizontal component of the fluid velocity,

$$\partial_X U_X + \partial_Z U_Z = 0, \implies \quad ik U_x^n + D u_z^n = 0,$$

where D represents the derivative with respect to Z, which further implies,

$$U_x^n = -\frac{DU_z}{ik},$$

we arrived to the final linearized non-dimensional system,

$$\lambda\alpha^n = -\Big(\alpha_0 DW_z^n + W_z^n D\alpha_0\Big) - \alpha_0 ikW_x^n - \Big(W_0 D\alpha^n + \alpha^n DW_0\Big), \tag{3.28}$$

$$\begin{aligned}\lambda(D^2-k^2)U_z^n = {} & Pr(D^2-k^2)^2U_z^n - PrRak^2\Theta^n + \frac{D\alpha_0(\beta-1)}{2}\lambda DU_z^n \\ & - \frac{6Pr(3-\beta)}{\Phi^2}\Big(\alpha_0(D^2-k^2)U_z^n + \alpha_0k^2W_z^n + \alpha_0 ikDW_x^n\Big) \\ & - \frac{6Pr(3-\beta)}{\Phi^2}\Big(D\alpha_0 DU_z^n + D\alpha_0 ikW_x^n\Big) + \frac{\alpha_0(\beta-1)}{2}\lambda(D^2-k^2)U_z^n \\ & - \left(\frac{\beta-1}{2}GaPr^2 + 6Pr(3-\beta)\frac{W_0}{\Phi^2}\right)k^2\alpha^n,\end{aligned} \tag{3.29}$$

$$\lambda {W_z}^n + W_0 D{W_z}^n + {W_z}^n\frac{dW_0}{dz} = \beta\lambda U_z^n + 12Pr\beta\frac{({U_z}^n - {W_z}^n)}{\Phi^2}, \tag{3.30}$$

$$\lambda {W_x}^n + W_0(D{W_x}^n) = \beta\lambda U_x^n + \frac{12Pr\beta}{\Phi^2}\left(-\frac{DU_z^n}{ik} - {W_x}^n\right), \tag{3.31}$$

$$(1-\alpha_0)[\lambda\Theta^n + U_z^n D\Theta_0] = \alpha^n\lambda\Theta_0 + (D^2-k^2)\Theta^n - 12\alpha_0\frac{(\Theta^n - \Theta_p^n)}{\Phi^2} - 12\alpha^n\frac{(\Theta_0 - \Theta_{p0})}{\Phi^2}, \tag{3.32}$$

$$\lambda\Theta_p^n + W_0 D\Theta_p^n + {W_z}^n D\Theta_{p0} = \frac{12}{E}\frac{\Theta^n - \Theta_p^n}{\Phi^2}, \tag{3.33}$$

where D represents the derivative with respect to Z.

Their boundary conditions, obtained by similar means from (2.47) and (2.48), are given by for fluid-phase

$$U_z^n = DU_z^n = 0, \quad \Theta^n = 0 \quad \text{at} \quad Z = \pm 1/2, \tag{3.34}$$

and for the particles

$$\alpha^n = 0, \quad \boldsymbol{W^n} = 0, \quad \Theta_p^n = 0 \quad \text{at} \quad Z = Z^*. \tag{3.35}$$

where $Z^* = 1/2$ for heavy particles ($\rho_p > \rho$) and $Z^* = -1/2$ for light particles ($\rho_p < \rho$).

3.4 Linear stability analysis of particulate Rayleigh-Bènard model system with particles injected at their terminal velocity ($\mathbf{W}^* = \mathbf{W_T}$)

In this section, we investigate a special case of the pRB system in which particles are introduced uniformly in the system that is with their terminal velocity. This uniform injection assumption leads to a significant simplification of the original model, facilitating a more straightforward analysis discussed in subsequent sections.

3.4.1 Conductive state

We start to analyze a condition where the fluid is at rest, the particles are uniformly distributed in the domain with a volume concentration α_0, and they continuously enter the system domain at the terminal velocity, $\boldsymbol{W}_0$, defined in (2.48). Ref. [126] observed that injecting particles with a different velocity (e.g., close to zero velocity) leads to the formation of a highly concentrated, nonuniform particle layer at the inlet boundary. Since this would complicate considerably the stability analysis (see e.g. [52] for the case of an isothermal layer), we adopt the same strict hypothesis: particles are injected at terminal velocity. This condition is realistic as long as the spatial distance across which the particles accelerates is much smaller than cell height. The order of magnitude of such a distance is $|\mathbf{w}_0|\tau_p$ (or in dimensionless terms $|\mathbf{W}_0|\frac{\Phi^2}{12Pr\beta}$).

In such a stationary conductive state, usually denoted as base state, the pressure gradient is only Z-dependent function given by

$$-\boldsymbol{\nabla} P = PrRa\Theta_0\hat{\mathbf{Z}} + \frac{\alpha_0(\beta-1)\Lambda\hat{\mathbf{Z}}}{2} + 12Pr(3-\beta)\frac{\mathbf{W}_0}{\Phi^2}, \tag{3.36}$$

in which the $\Theta_0 = \Theta_0(Z)$ is the base fluid temperature field, which can be computed according to the following steps. First, the particle temperature equations in the conductive state using equation (2.45) reads,

$$\Theta_0 = W_0\frac{E\Phi^2}{12}\partial_Z\Theta_{p0} + \Theta_{p0}, \tag{3.37}$$

here $\Theta_{p0} = \Theta_{p0}(Z)$ is the undistributed particle temperature. Second, upon elimination of the term $(\Theta - \Theta_p)$ from equations (2.44) and (2.45) yields,

$$\partial_Z^2 \Theta_0 - W_0 E\alpha_0 \, \partial_Z \Theta_{p0} = 0, \tag{3.38}$$

Third and finally, by eliminating Θ_0 from equations (3.37) and (3.38) we get,

$$\partial_Z (W_0 \frac{E\Phi^2}{12} \partial_Z^2 \Theta_{p0} + \partial_Z \Theta_{p0} - W_0 E\alpha_0 \, \Theta_{p0}) = 0. \tag{3.39}$$

This third order linear differential equation can be solved analytically and, by means of the boundary conditions for the inlet particle temperature and for the fluid temperature on top and bottom walls, one gets the explicit expression:

$$\Theta_{p0} = \Theta_p^* + C_1\Big[1 - e^{k_1(Z-Z^*)}\Big] + C_2\Big[1 - e^{k_2(Z-Z^*)}\Big], \tag{3.40}$$

here C_1 and C_2 are integration constants and

$$k_{1,2} = \frac{6}{W_0 E\Phi^2}\left(-1 \pm \sqrt{1 + \frac{W_0^2 E^2 \Phi^2 \alpha_0}{3}}\right).$$

Using equations (3.36) and (3.40), the base state temperature field in the fluid phase is therefore determined as

$$\Theta_0 = \Theta_p^* + C_1\Big[1 - (1 + lk_1)e^{k_1(Z-Z^*)}\Big] + C_2\Big[1 - (1 + lk_2)e^{k_2(Z-Z^*)}\Big]. \tag{3.41}$$

where $l = W_0 E\Phi^2/12$. The integration constants are determined by the fluid temperature boundary conditions at the top and bottom of the cell, respectively, $Z = \pm\frac{1}{2}$. Their complete expression is:

$$C_1 = \frac{e^{\left(\frac{1}{2}+Z^*\right)k_1}\left(-e^{\left(\frac{1}{2}+Z^*\right)k_2} - (1+k_2 l)\left(e^{k_2}(-1+\Theta_p^*) - \Theta_p^*\right)\right)}{e^{\left(\frac{1}{2}+Z^*\right)k_1}(-1+e^{k_2})(1+k_2 l) + (1+k_1 l)\left(-e^{\left(\frac{1}{2}+Z^*\right)k_2}(-1+e^{k_1}) + (e^{k_1}-e^{k_2})(1+k_2 l)\right)}, \tag{3.42}$$

$$C_2 = \frac{e^{\left(\frac{1}{2}+Z^*\right)k_2}\left(-e^{\left(\frac{1}{2}+Z^*\right)k_1} - (1+k_1 l)\left(e^{k_1}(-1+\Theta_p^*) - \Theta_p^*\right)\right)}{e^{\left(\frac{1}{2}+Z^*\right)k_2}(-1+e^{k_1})(1+k_1 l) + (1+k_2 l)\left(-e^{\left(\frac{1}{2}+Z^*\right)k_1}(-1+e^{k_2}) - (e^{k_1}-e^{k_2})(1+k_1 l)\right)}. \tag{3.43}$$

The base fluid temperature vertical profile (eq. 3.41) is plotted in Figure 3.5 for the case of heavy particles with $\beta = 0.5$ and different values of the heat capacity ratio E and particle diameter Φ. In this case, particles are injected from above with the same temprature as the one of the top horizontal boundary temperature ($\Theta_p^* = 0$). One may observe that for small values of E the profile remains close to linear, which is what is expected in the single-phase Rayleigh-Bénard system, but larger gradients appear for large values of E and Φ. In the case where both E and Φ assume the largest values, it may be observed that the fluid temperature remains almost constant on the upper part of the system. As a consequence, a region of strong unstable thermal stratification forms at the bottom. Figure 3.6 shows the base fluid temperature vertical distribution for the case of light particles with $\beta = 1.5$, injected from the bottom with the hot wall temperature ($\Theta_p^* = 1$). The temperature field appears to be nearly the upside-down mirrored copy of the ones just observed for the heavy particle case. Additionally, the influence of inlet particles temperature for both heavy (solid lines) and light (dashed lines) particles is presented in Figure 3.7. In this case temperature gradients can appear also at the particle inlet wall due to the local heating/cooling produced by the particulate phase on the fluid.

3.4.2 Problem reduction

The boundary condition for the particle velocity fluctuation at the inlet wall, $\boldsymbol{W}' = 0$, implies that $\partial_X \boldsymbol{W}' = 0$, and by means of (3.24) also that $\partial_Z \boldsymbol{W}' = 0$ at the same wall ($Z = Z^*$). This has a consequence that $\nabla \cdot \boldsymbol{W}' = 0$ at the inlet. Now, as already observed in [50], taking the divergence of equation (3.24) we get

$$\partial_{\mathcal{T}}(\nabla \cdot \boldsymbol{W}') - W_0 \partial_z(\nabla \cdot \boldsymbol{W}') = -12 Pr \beta \frac{(\nabla \cdot \boldsymbol{W}')}{\Phi^2}, \tag{3.44}$$

here we observe that the equation for $\nabla \cdot \boldsymbol{W}'$ is not coupled to other equations, and it can be solved. Its solution is obtained by introducing the new variable $\mathcal{Y} \equiv \mathcal{T} + Z/W_0$ so

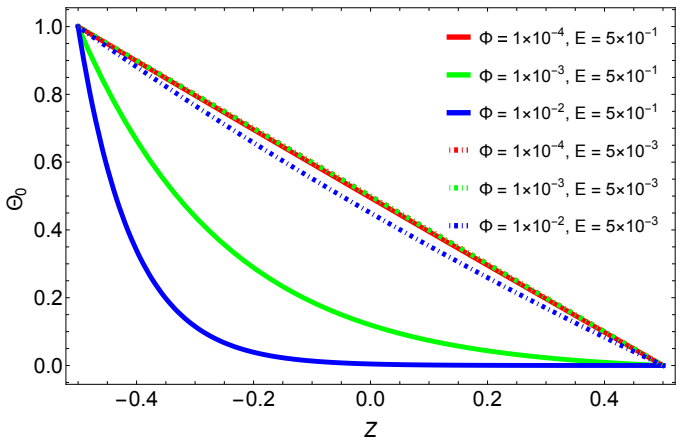

Figure 3.5: The fluid temperature vertical distribution in the cell diameter for heavy particles ($\Theta_p^* = 0$) with respect to different values of the particle diameter Φ. The particles to fluid heat capacity ratio $E = 5 \times 10^{-1}$ (solid lines) and $E = 5 \times 10^{-3}$ (dashed lines), the particle to fluid density ratio $\beta = 0.5$. The particle volume fraction is $\alpha_0 = 10^{-3}$, and the Galileo number $\Lambda = 48 \times 10^{10}$.

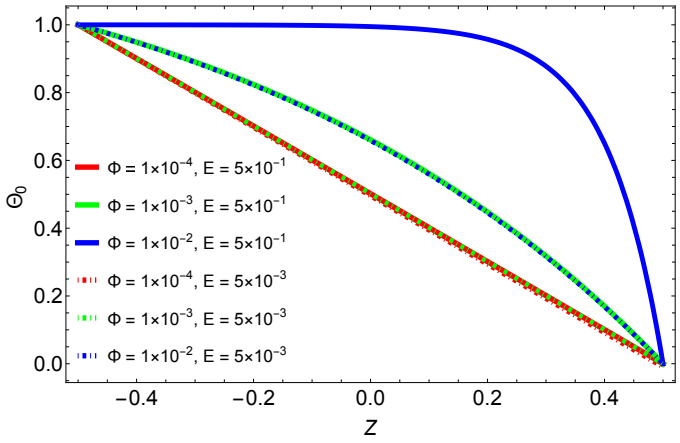

Figure 3.6: The fluid temperature vertical distribution in the cell for light particles ($\Theta_p^* = 1$) with respect to different values of the particle diameter Φ. The particles to fluid heat capacity ratio $E = 5 \times 10^{-1}$ (solid lines) and $E = 5 \times 10^{-3}$ (dashed lines), the particle to fluid density ratio $\beta = 1.5$. The particle volume fraction is $\alpha_0 = 10^{-3}$, and the Galileo number $\Lambda = 48 \times 10^{10}$.

that $d\mathcal{Y} = d\mathcal{T} + dZ/W_0$ with this the equation becomes

$$\partial_{\mathcal{Y}} \nabla \cdot \boldsymbol{W}' = -12 Pr \beta \frac{\nabla \cdot \boldsymbol{W}'}{\Phi^2}, \tag{3.45}$$

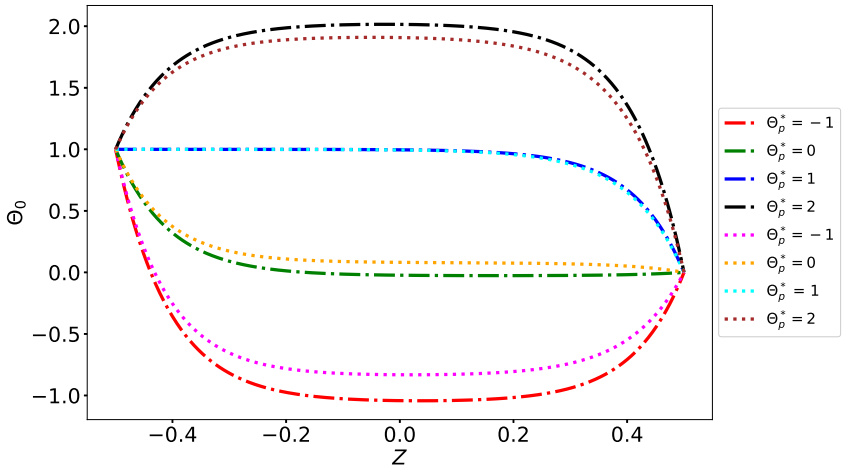

Figure 3.7: The fluid temperature vertical distribution in the cell for $\Theta_p^* = -1, 0, 1, 2$ for heavy $\beta = 0.5$ (dash dot lines) and light $\beta = 1.5$ (dotted lines) particles .The dimensionless particle diameter $\Phi = 10^{-2}$, the particles to fluid heat capacity ratio $E = 5 \times 10^{-1}$, the particle to fluid density ratio $\beta = 0.5$.

therefore the solution is

$$\nabla \cdot \boldsymbol{W}' = C e^{-\frac{12Pr\beta}{\Phi^2}(\mathcal{T} + Z/W_0)}, \tag{3.46}$$

indicating with $\nabla \cdot \boldsymbol{W}'|_{Z=Z^*} = \nabla \cdot \boldsymbol{W}'(\mathcal{T}, Z = 1/2)$ the condition at the top, $Z = 1/2$, for any time $\mathcal{T}$ one get $C = \nabla \cdot \boldsymbol{W}'|_t \; e^{\frac{12Pr\beta}{\Phi^2}(\mathcal{T} + 1/(2W_0))}$ so

$$\nabla \cdot \boldsymbol{W}'(Z, \mathcal{T}) = \nabla \cdot \boldsymbol{W}'|_{Z=Z^*} \; e^{\frac{12Pr\beta}{\Phi^2 W_0}(1/2 - Z)}. \tag{3.47}$$

Note that when the boundary condition is applied at $Z = 1/2$ it means that $W_0 < 0$, hence the above solution is decreasing as one moves away from the top wall (which is in $Z = 1/2$). In principle the constant can depend on the horizontal direction X and of time, but we show here below that it must be just a constant.

We now consider the equations for α' and $\nabla \cdot \boldsymbol{W}'$, by dividing the first by α_0 and the second by $12Pr\beta/\Phi^2$ and by subtracting them, we obtain:

$$(\partial_{\mathcal{T}} + W_0 \partial_z)\left(\frac{\alpha'}{\alpha_0} - \frac{\Phi^2}{12Pr\beta}\nabla \cdot \boldsymbol{W}'\right) = 0. \tag{3.48}$$

This implies that the quantity $\frac{\alpha'}{\alpha_0} - \frac{\Phi^2}{12Pr\beta}\nabla \cdot \boldsymbol{W}'$ is just transported by the flow and that it has the same value at the top $Z = 1/2$ and at the bottom $Z = -1/2$. It follows that if

$\alpha'(Z = 1/2) = \alpha'(Z = -1/2)$ then $\nabla \cdot \boldsymbol{W}'$ is equal on top and bottom, and by using the solution for $\nabla \cdot \boldsymbol{W}'$ one finds $\nabla \cdot \boldsymbol{W}' = 0$ everywhere.

The above solution can be inserted in the equation for α', it gives

$$\partial_{\mathcal{T}} \alpha' - W_0 \partial_z \alpha' = \alpha_0 \, \nabla \cdot \boldsymbol{W}'|_{Z=Z^*} \, e^{\frac{-12Pr\beta}{\Phi^2 W_0}(1/2-Z)}, \tag{3.49}$$

which can be written in the Lagrangian frame, where $Z(\mathcal{T}) = 1/2 - W_0 \mathcal{T}$, as

$$\frac{d}{d\mathcal{T}} \alpha' = \alpha_0 \nabla \cdot \boldsymbol{W}'|_{Z=Z^*} \, e^{\frac{-12Pr\beta}{\Phi^2}\mathcal{T}}, \tag{3.50}$$

which has solution

$$\alpha'(\mathcal{T}) = \alpha'(0) + \alpha_0 \nabla \cdot \boldsymbol{W}'|_{Z=Z^*} \, \frac{\Phi^2}{-12Pr\beta} \left(e^{(\frac{-12Pr\beta}{\Phi^2})\mathcal{T}} - 1 \right).$$

Now going back to the Eulerian frame and considering that $\alpha' = 0$ in $Z = 1/2$ we obtain:

$$\alpha' = \nabla \cdot \boldsymbol{W}'|_{Z=Z^*} \, \frac{\alpha_0 \Phi^2}{12Pr\beta} \left(1 - e^{\frac{-12Pr\beta}{\Phi^2 W_0}(1/2-Z)} \right), \tag{3.51}$$

the latter relation has an important consequence because through above equation one obtains $\alpha' = \alpha'|_{Z=Z^*} = 0$. Hence the chosen inlet condition for the particles imposes that the particle concentration is always constant throughout the system. In other words the phenomenon of **particle clustering cannot occur** in the present conditions.

As next step we eliminate the pressure field from the fluid momentum equation (3.14). This is achieved by taking the double curl of the fluid momentum equation.

$$\begin{aligned} \partial_{\mathcal{T}} \nabla^2 \boldsymbol{U}' = {} & Pr \nabla^4 \boldsymbol{U}' - PrRa(\nabla(\partial_Z \Theta') - \nabla^2 \Theta' \hat{\boldsymbol{Z}}) + \frac{\alpha_0(\beta - 1)}{2} \partial_{\mathcal{T}} \nabla^2 \boldsymbol{U}' \\ & + \alpha_0 \frac{6Pr(3-\beta)}{\Phi^2} (-\nabla^2 \boldsymbol{U}' + \nabla^2 \boldsymbol{W}' - \nabla(\nabla \cdot \boldsymbol{W}')) \\ & - \left(\frac{(\beta - 1)}{2} \Lambda + 6Pr(3-\beta) \frac{W_0}{\Phi^2} \right) (\nabla(\partial_Z \alpha') - \nabla^2 \alpha' \hat{\boldsymbol{Z}}), \end{aligned} \tag{3.52}$$

by substituting $\nabla \cdot W' = 0$ and $\alpha' = 0$ the problem is now reduced to four equations.

$$\begin{aligned}
\partial_T \nabla^2 \boldsymbol{U}' &= Pr\nabla^4 \boldsymbol{U}' - Pr\,Ra\Big(\nabla(\partial_Z \Theta') - \nabla^2 \Theta' \hat{\boldsymbol{Z}}\Big) \\
&+ \frac{\alpha_0(\beta-1)}{2}\partial_T \nabla^2 \boldsymbol{U}' + \alpha_0 \frac{6Pr(3-\beta)}{\Phi^2}\Big(-\nabla^2 \boldsymbol{U}' + \nabla^2 \boldsymbol{W}'\Big), \qquad (3.53)\\
\partial_T \boldsymbol{W}' &= -W_0 \partial_Z \boldsymbol{W}' + \beta \partial_T \boldsymbol{U}' + 12Pr\beta \frac{(\boldsymbol{U}' - \boldsymbol{W}')}{\Phi^2}, \qquad (3.54)\\
\partial_T \Theta' &= -U_Z' \partial_Z \Theta_0 + \nabla^2 \Theta' - 12\alpha_0 \frac{\Theta' - \Theta_p'}{\Phi^2}, \qquad (3.55)\\
\partial_T \Theta_p' &= -W_0 \partial_Z \Theta_p' - W_Z' \nabla \Theta_{p0} + \frac{12}{E}\frac{\Theta' - \Theta_p'}{\Phi^2}. \qquad (3.56)
\end{aligned}$$

3.4.3 Modal Analysis

Adopting the same procedure laid down earlier in section (3.3.3), we obtained the final linearized system,

$$\begin{aligned}
(D^2 - k^2)\left[\left(1 - \frac{\alpha_0(\beta-1)}{2}\right)\lambda U_z^n - (D^2 - k^2)Pr U_z^n\right] + PrRak^2\Theta_n \\
+ \frac{6\alpha_0 Pr(3-\beta)}{\Phi^2}(D^2 - k^2)(U_z^n - W_z^n) = 0,
\end{aligned} \qquad (3.57)$$

$$\lambda W_z^n - \frac{(1-\beta)}{\beta}\frac{\Lambda\Phi^2}{12Pr} D W_z^n - 12Pr\beta \frac{(U_z^n - W_z^n)}{\Phi^2} - \beta\lambda U_z^n = 0, \qquad (3.58)$$

$$\lambda\Theta^n + U_z^n D\Theta_0 - (D^2 - k^2)\Theta^n + 12\alpha_0 \frac{(\Theta^n - \Theta_p^n)}{\Phi^2} = 0, \qquad (3.59)$$

$$\lambda\Theta_p^n - \frac{(1-\beta)}{\beta}\frac{\Lambda\Phi^2}{12Pr} D\Theta_p^n + W_n D\Theta_{p0} - \frac{12}{E}\frac{(\Theta^n - \Theta_p^n)}{\Phi^2} = 0, \qquad (3.60)$$

subject to the following boundary conditions for the fluid

$$U^n = DU^n = 0, \qquad \Theta^n = 0 \qquad \textbf{at} \quad Z = \pm\frac{1}{2}, \qquad (3.61)$$

and for the particles

$$\text{heavy } (\beta < 1): \quad W^n = 0 \qquad \Theta_p^n = 0 \qquad \textbf{at} \quad Z = \frac{1}{2}, \qquad (3.62)$$

$$\text{light } (\beta > 1) \quad W^n = 0 \qquad \Theta_p^n = 0 \qquad \textbf{at} \quad Z = -\frac{1}{2}. \tag{3.63}$$

where D represents the derivative with respect to Z.

In the above simplified model, the x- and z-components of the momentum equation are decoupled, so the stability is independent of W_x and U_x. The results for this case are presented in Chapter 5. As before, we set $\lambda_r = 0$ to simplify the formulation and focus on the essential stability features.

Chapter 4

Numerical methods

Outline of the current chapter

In this chapter, we describe in detail the numerical methods used to solve the mathematical model system presented in previous chapters, each with its own advantages and limitations. The Galerkin method has been widely used in stability and bifurcation analyses due to its relatively simple implementation and low computational cost [132]. However, its accuracy is strongly dependent on the truncation order: low-order expansions often capture only the dominant features of the solution, while higher-order truncations significantly increase the computational cost [108]. The shooting method, in contrast, is capable of producing highly accurate solutions but requires a sufficiently accurate initial guess to ensure convergence; without this, the iteration may either diverge or converge to an irrelevant root instead of desired critical root.[133]. To address this difficulty, a low-order Galerkin solution is employed to provide an effective starting point for the shooting method. Furthermore, a matrix forming approach is

introduced, which, although more computationally demanding for larger systems, offers a systematic framework for validation and allows the identification of additional unstable or secondary solutions [142]. By combining these complementary methods, the analysis balances efficiency, accuracy, and robustness, thereby ensuring reliable results throughout the study.

4.1 Shooting method

4.1.1 What is shooting method?

In numerical analysis, the shooting method in technique to solve the boundary value problem by changing it into the initial value problem. The procedure involved in this method is one try to find the solution of initial value problem considering different initial conditions which also satisfied the boundary conditions of the boundary value problem (BVP). To put it simply, one "shoots" out trajectories from one boundary in various directions until they identify the trajectory that "hits" the adjacent boundary condition.

4.1.2 Implementation

The shooting method is used to determine the accurate solutions of the eigenvalue problem associated with the linear instability of the system under investigation. The method transforms the original boundary value problem (BVP) into an initial value problem (IVP), which is then integrated numerically.

The system of equations (3.28)–(3.33) is first rewritten using new initial conditions based on the boundary conditions (3.34) and (3.35):

$$U^n = DU_z^n = 0, \quad D^2U_z^n = \mathcal{C}_1, \quad D^3U_z^n = \mathcal{C}_2 \quad \text{at } Z = Z^*, \tag{4.1}$$

$$\theta_n = 0, \quad D\theta_n = \mathcal{C}_3 \quad \text{at } Z = Z^*, \tag{4.2}$$

$$\alpha^n = 0, \quad W_z^n = 0, \quad W_x^n = 0 \quad \text{at } Z = Z^*, \tag{4.3}$$

where Z^* denotes the location of the inlet horizontal wall. $\mathcal{C}_1$,$\mathcal{C}_2$,$\mathcal{C}_3$ are constants that are initially undetermined and must be chosen such that the boundary conditions at the outlet wall (the one opposite to Z^*) are satisfied.

Since this is an eigenvalue problem, one of these constants must remain arbitrary. In this work, the system is scaled by setting $\mathcal{C}_3 = 1$, allowing simplification without redefining dependent variables. The goal is to find suitable values of two real parameters, denoted $\mathcal{P}_1$ and $\mathcal{P}_2$, along with $\mathcal{C}_1$ and $\mathcal{C}_2$, such that the computed solution at $Z = Z^*$ satisfies the original boundary conditions.

To implement the shooting method, two numerical procedures are employed:

- **First procedure:** The initial value problem is integrated from $Z = -\frac{1}{2}$ to $Z = +\frac{1}{2}$ using the built-in function `NDSolve` in *Mathematica*. Initial conditions from (4.1)-(4.3) are used with trial values of $\mathcal{P}_1$, $\mathcal{P}_2$, Re[$\mathcal{C}_1$], Im[$\mathcal{C}_1$], Re[$\mathcal{C}_2$], and Im[$\mathcal{C}_2$]. All other parameters are held fixed. In its default method option **Automatic**, it uses variable marching steps and switches between different schemes, with different numerical stability and accuracy orders. The step size and local errors are controlled using specified absolute and relative tolerances. The **WorkingPrecision** is increased (e.g., to 16, 18, or 20 digits) to ensure convergence and accuracy.

- **Second procedure:** A mismatch function $\mathcal{F}_1$ is defined to quantify how far the numerical solution at $Z = Z^*$ deviates from the desired boundary conditions. This function returns a vector containing:

$$\text{Re}[U_z^n],\ \text{Im}[U_z^n],\ \text{Re}[DU_z^n],\ \text{Im}[DU_z^n],\ \text{Re}[\theta_n],\ \text{Im}[\theta_n],$$

  all evaluated at $Z = Z^*$. The root-finding function `FindRoot` is then used to compute the values of $\mathcal{P}_1$ and $\mathcal{P}_2$ that drive the mismatch function $\mathcal{F}_1$ to zero using Newton's method. The iteration stopping criterion is controlled by another **WorkingPrecision** parameter. Grid convergence is performed by increasing the value assigned to **WorkingPrecision** until the desired number of converged digits is achieved.

This procedure is crucial for identifying unstable modes. The accuracy of the root-finding depends heavily on the quality of the initial guesses and on the nature of the instability mechanism, which may vary with the physical configuration. In the next section, we therefore turn to the Galerkin method, which will serve both as a tool for providing such initial guesses and as an independent approach for cross-validation.

4.2 Galerkin method

To numerically determine the solution to the eigenvalue problem, we will expand the variables in the form of polynomial functions of order N chosen so that the obtained solution converges. These functions must satisfy the boundary conditions of the problem. We will apply the Galerkin method, based on the principle of weighted residuals; which consists of searching for the unknown functions such that their residue (defined as the equation in which the unknown functions have been replaced by their approximation) weighted by a certain function (called the weighting function) is of zero integral over the domain of the problem.

4.2.1 Galerkin Approximation

We consider following polynomial approximation

$$\begin{cases} U^n(z) = \sum_{i=0}^{N-1} A_i(z)\,\bar{U}_i, \\ W^n(z) = \sum_{i=0}^{N-1} B_i(z)\,\bar{W}_i, \\ \Theta^n(z) = \sum_{i=0}^{N-1} C_i(z)\,\bar{\theta}_i, \\ \Theta_p^n(z) = \sum_{i=0}^{N-1} D_i(z)\,\bar{\theta}_i, \end{cases}$$

where $A_i(z), B_i(z), C_i(z)$ and $D_i(z)$ are families of polynomials that will be chosen according to the problem to be solved. In this study, we employed the Galerkin method for the pRB system (3.57)-(3.60), in which particles are injected at their terminal velocity ($W^* = W_T$). In order to verify boundary conditions (3.61)-(3.63), these polynomials will be chosen here of the form:

$$\begin{cases} A_i(z) = (1-4z^2)^2 z^i, \\ B_i(z) = (1 \mp 2z) z^i, \\ C_i(z) = (1-4z^2) z^i, \\ D_i(z) = (1 \mp 2z) z^i, \end{cases} \quad \text{with} \quad \begin{cases} - \text{ sign if } \beta < 1 & \text{(heavy particles)} \\ + \text{ sign if } \beta > 1 & \text{(light particles)} \end{cases}$$

The corresponding equations are then multiplied by the corresponding weighting function and integrated over the z-domain.

This leads to the matrix eigenvalue problem:

$$A\mathbf{c} = \lambda B\mathbf{c},$$

where:

$$A_{ij} = a(\phi_j, \phi_i), \quad B_{ij} = b(\phi_j, \phi_i),$$

and $\mathbf{c} = [c_1, c_2, \ldots, c_n]^T$ is the vector of unknown coefficients.

We used the built-in `Mathematica` functions `Eigenvalues` and `Eigenfunctions` to compute the eigenvalues and eigenfunctions of the system, after specifying the control parameters Ra (Rayleigh number) and k (wavenumber). Eigenvalues provide critical information about the growth or decay of modes in a dynamical system, while eigenfunction represent the corresponding spatial structures. By tracking the behavior of the eigenvalues, we identified the critical mode where the real part of the eigenvalue crosses zero—this marks the transition of the system from a stable to an unstable state.

`Mathematica`'s symbolic and numerical capabilities, combined with its high-level functions for linear algebra and differential operators, make it a powerful tool for eigenvalue problems. The `Eigenvalues` and `Eigenfunctions` commands automatically handle the underlying algebra and numerical methods, enabling efficient analysis of linear stability in parameter-dependent systems. This facilitated our identification of the bifurcation point at which the system loses stability, a key step in understanding the onset of convection in the given model. Figure 4.1 shows an example of the convergence of the Galerkin method for different truncation orders N.

4.3 Matrix-forming approach

In order to verify the accuracy and validate the results presented in the subsequent chapters, a *matrix-forming approach* is also employed. The procedure follows the same formulation discussed earlier for the shooting method, where the system of normal-mode differential equations was derived.

A fourth-order finite-difference discretization is applied to transform the differential system into a generalized algebraic eigenvalue problem (EVP) of the form

$$A\,\mathbf{c} = \lambda\, B\,\mathbf{c},$$

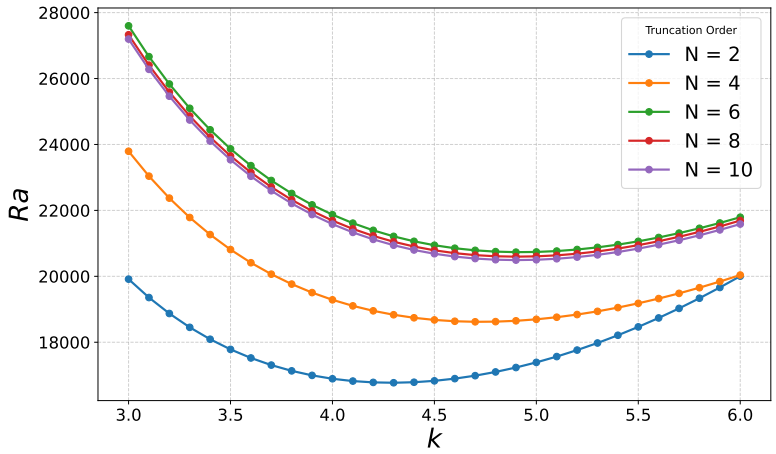

Figure 4.1: Convergence test of the Galerkin method: marginal stability curves obtained for different truncation orders N.

where A and B are the coefficient matrices resulting from the spatial discretization of the governing equations, and $\mathbf{c} = [c_1, c_2, \ldots, c_n]^T$ is the vector of unknown perturbation amplitudes.

The resulting generalized EVP is then solved numerically using the Arnoldi method with a shift-and-invert spectral transformation (see [142] for details).

4.4 Comparison and validation of the different numerical approaches

In this section, we present results that compare the different numerical approaches discussed earlier, namely the shooting method, the Galerkin method, and the matrix-forming approach. Figure 4.2 illustrates the marginal stability curves obtained from both the shooting and Galerkin methods. The results from these two approaches show excellent quantitative as well as qualitative agreement. Furthermore, Figure 4.3 presents a comparison between the shooting method and the matrix-forming approach, where once again a close agreement between the two sets of results is observed. These validations confirm the consistency and reliability of the numerical methods employed in this study.

To conclude this chapter, it is important to emphasize the strategy adopted in this work. The Galerkin method was primarily employed to generate accurate initial guesses

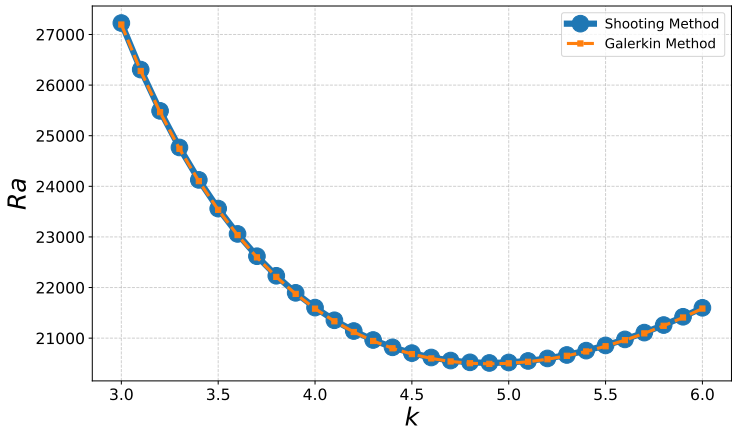

Figure 4.2: Marginal stability curves obtained using the shooting method and the Galerkin method. The results demonstrate excellent agreement between the two approaches, both quantitatively and qualitatively.

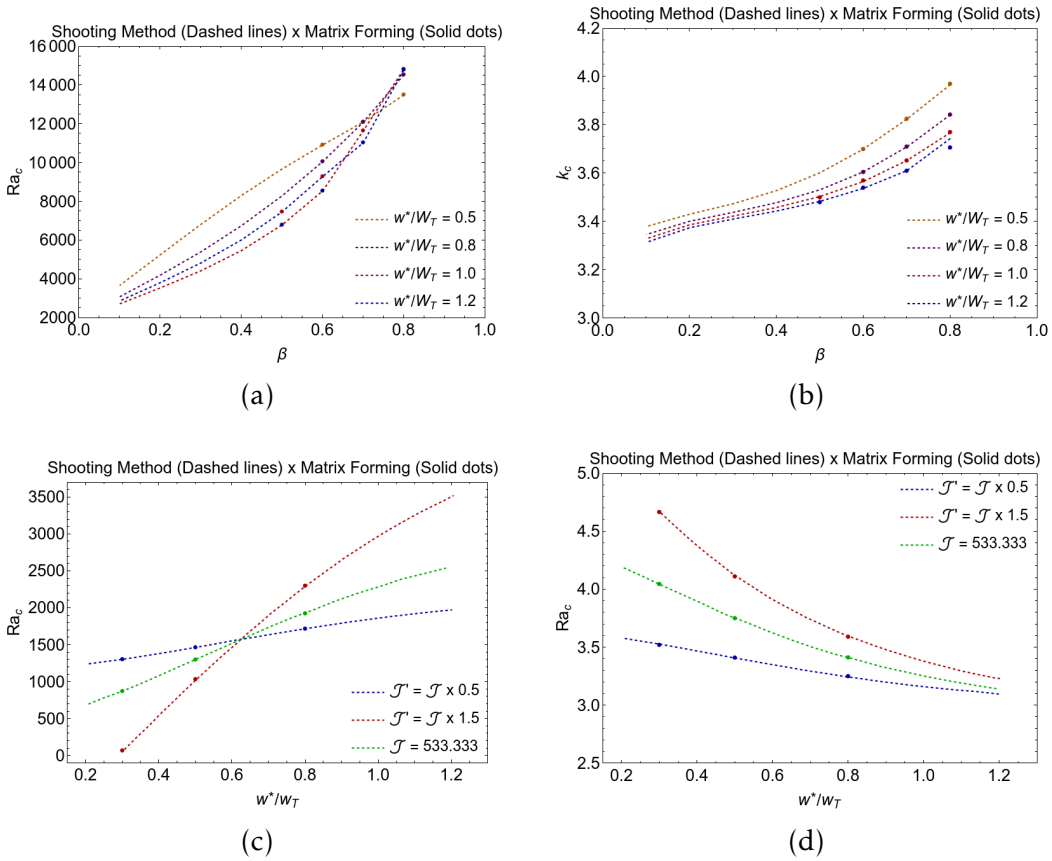

Figure 4.3: Comparison of the shooting method and the matrix-forming approach. (a–b) Critical Rayleigh number and critical wavenumber as functions of the mass density β. (c–d) Critical parameters as functions of the inlet velocity. Results from both methods show very good agreement, validating the accuracy of the numerical approaches.

for the shooting method. Subsequently, all the final results were obtained using the shooting method, owing to its accuracy and robustness. The matrix-forming approach was used only in selected cases for validation, thereby reinforcing the reliability of the results presented in this thesis.

Part III

Results

Chapter 5

Stabilization of the Rayleigh-Bénard system by injection of thermal inertial particles and bubbles at their terminal velocity

Outline of the current chapter

This chapter addresses the impact of a dispersed particulate phase on the onset of Rayleigh–Bénard (RB) convection, with emphasis on the stabilizing role of thermo-mechanical particle–fluid interactions. The work presented here is based on the article *"Stabilization of the Rayleigh–Bénard System by Injection of Thermal Inertial Particles and Bubbles"*, published in Physics of fluids and coauthored with S. Hirata and E. Calzavarini [146].

We consider a thermally stratified fluid layer bounded by two horizontal walls, into which non-Brownian spherical particles with inertia and heat capacity are continuously injected at their **terminal settling velocity**. These particles exchange momentum and heat with the carrier fluid, introducing additional couplings that modify the linear stability properties of the RB system. Both heavier-than-fluid and lighter-than-fluid particles (bubbles) are examined, allowing us to explore the full density spectrum relevant to multiphase convection.

The linear stability analysis shows that the onset of convection remains stationary, with the system undergoing a pitchfork bifurcation as in the classical single-phase RB problem. Nonetheless, the particulate phase introduces strong stabilizing effects. Mechanical coupling due to particle inertia always raises the critical Rayleigh number Ra_c, delaying the onset of convection. Furthermore, the ratio of particle to fluid heat capacities provides a distinct thermal stabilization mechanism, which we analyze by addressing the limiting cases of negligible and overwhelming particle thermal inertia. The combined impact of these couplings is significant: at a particulate volume fraction of only 0.1%, the critical threshold is increased by up to a factor of 30 for the lightest particles and 60 for the heaviest ones.

These results extend the earlier work of Prakhar & Prosperetti [50], who first demonstrated the stabilizing effect of heavy inertial particles. By including the added-mass force in the model, we succeed in covering the entire range of density ratios, thereby offering a more general picture of stabilization by inertial particles and bubbles. Finally, we highlight the influence of the particle injection boundary conditions adopted in this study and discuss their potential role in producing alternative dynamical behaviors.

The chapter is organized as follows. Section 5.1 introduces the problem and its context. In Sec. 5.2, we present the results and discussion, beginning with the perturbative solution in the dilute limit (Sec. 5.2.1) and the analysis of thermal coupling cases (Sec. 5.2.2). We then characterize the linear properties of the instability (Sec. 5.2.3) and examine the role of particle mass density (Sec. 5.2.4), volumetric particulate flux (Sec. 5.2.5), particle size (Sec. 5.2.6), and volumetric heat flux (Sec. 5.2.7). The influence

of particle injection temperature is addressed in Sec. 5.2.8, followed by an energy budget analysis in Sec. 5.2.9. Concluding remarks are provided in Sec. 5.3.

5.1 Introduction

Virtually all fluids present in the natural environment contain dispersed matter, i.e., matter of a different composition from the one of the surrounding environment. This occurs in the form of solid particles, liquid drops or gaseous bubbles. Examples include phenomena as diverse as sand and pollens in the near ground air, rain drops and ice crystals in clouds, air bubbles entrained at the sea-air interface, volatile elements springing up in solidifying magma and planktonic microorganisms dispersed in the ocean[100, 99, 101, 102, 103, 104, 105, 106, 86]. Such particle laden fluids are often set into motion by thermal differences present in the environment. However, while most of the time the role played by the dispersed phase is negligible for the overall dynamics of the fluid - think e.g. to the passive role of the grains of dust brought in suspension by a storm - there are situations where the mechanical agitation and/or the thermal coupling produced by the dispersed phase are relevant for the resulting flow dynamics (one of such examples is bioconvection [85]). Fluid-particle coupling phenomena are also of interest for industrial applications such as for optimization of mixing in bubble column reactors or for the design of particle based solar collectors [107, 109, 110, 111]. The widespread relevance of this topic has spurred extensive researches aimed at understanding the complex interplays governing the dynamics of particle-laden fluid flows [112, 113, 114].

To gain insight into particle-fluid systems, several approaches are possible, each corresponding to different physical conditions of the problem at hand but also to distinct levels of abstraction in their description. At the most refined level we find the “particle resolved" approach that treat the complete fluid-dynamical and thermal fluid-solid body interaction problem. This is the only sound modelization when the characteristic scales of the particulate phase are large as compared to the ones of the fluid. However, the major drawback of this approach is the complexity of its mathematical treatment even with state-of-the-art numerical methods, due to the high numbers of degrees of freedom involved [90]. When the particle sizes are of the same order or smaller than the typical spatial scales of the flow and of the heat transfer process, the particle description can be approximated by material points (dubbed “point particles"). Their coupling

to the fluid can be described by localized forces or source terms that satisfy global conservation laws of mass, momentum and energy. It falls in this case the so called Eulerian-Lagrangian modelization of particulate laden flows, where the fluid variables are treated as continuous fields evolving in the Eulerian frame, while the particles are described as individual entities in the Lagrangian frame. A further level of abstraction is represented by the two-fluid or Eulerian-Eulerian methods where both phases are described in terms of conservation equations for continuous and differentiable fields. The particulate state variables are typically their mass concentration, velocity and local temperature but additional degrees of freedom can be introduced (e.g. the local particle orientation, in case of non spherical particles) [116, 117]. The latter approach has even a more restrictive domain of applications as it requires the particles not only to be tiny in size but also to be sufficiently numerous in order to be able to define continuous state variables in space and time. One appealing aspect of fully Eulerian models is the relative simplicity of their governing equations, which are expressed in the form of partial differential equations that closely resemble the local conservation laws of fluids and transported scalar fields. This also implies that analytical approaches, as for instance the ones of hydrodynamic stability [138] or fluctuating hydrodynamics [140] can be straightforwardly adapted to this type of modelling.

In the present work we aim at understanding how settling and rising thermal inertial particles affect the hydrodynamic stability of an immobile thermally stratified fluid layer. This will be achieved by adopting a fully Eulerian modelization and by performing a fluid dynamics linear stability analysis of the system's governing equations. The system we study in this article builds on the classical model of natural convection, known as Rayleigh-Bénard (RB) model system, which is a layer of fluid between two horizontal planes kept at different constant temperatures, the above one being colder so that the fluid layer is slightly denser on top with respect to the bottom [1]. If the system does not contain a pure fluid but rather a suspension of material particles, it goes under the name of particulate Rayleigh-Bénard (pRB) system [39]. The research questions of interest in the pRB context are multiple. On one hand it is interesting to understand how the fluid flow affects the particle dynamics. In particular how it impacts on the particle spatial distribution and clusters formation, or how it affects the settling speeds, the resulting sedimentation patterns forming at the walls and the possibility of particle resuspension and entrainement by the flow. On the other hand it is pertinent to tackle how the feedback of the particulate phase can in turn influence the spatial structure and

the temporal evolution of the flow, affecting its thermal stability, modulating the heat transfer across the system or disrupting the coherent flow structures that characterize the single phase RB flow. Many of these questions have been addressed in former studies and a comprehensive overview of them goes beyond the scope of this brief introduction. It is worth mentioning here the pioneering experimental studies by Solomatov et al. [97] and Lavorel et al. [131] focused on the settling dynamics of solid particles and to their resuspension in vigorously convective fluids, the more recent experiments on vapour droplets dynamics in a supersaturated RB cell (cloud chamber) [93], the studies on the dynamics of large non-isotropic particles in RB [135, 134]. More frequent are the numerical studies that have attempted a characterization of the one-way coupled dynamics of particles in RB [136, 120, 121, 95, 92]. When the so called two-way coupling is considered, i.e. the particle feedback on the fluid flow, the dynamics and the parameter space of the problem becomes much wider. Oresta et al. [33, 126, 127] showed that the presence of vapor bubbles or suspended particles in a cylindrical convective cell significantly influence flow and heat transfer.

Studies with a similar Eulerian-Lagrangian point-particle numerical approach where conducted by Park et al. [39] and in [130, 125, 96, 94]. This line of research goes even beyond the RB setting and extend to general convective turbulent flows, see e.g. [124]. Numerical studies adopting particle resolved approach, where both mechanical and thermal couplings between dispersed phase and the fluid are included, are on the other hand quite recent, with limitations in the number of particles [122, 123, 137]. This constraint however will become likely less severe in the forthcoming future as more computational power will be available.

In this work, we build upon the recent key findings of the work by Prakhar & Prosperetti [50], which demonstrated theoretically by means of a two-fluid modelization that the introduction of particles, whose density is much larger than the fluid one, has a sensible stabilizing effect on the onset of convection in the Rayleigh-Bénard system. This stabilizing influence becomes increasingly pronounced with rising the particle concentration and the mass density and is primarily attributed to the mechanical interactions between the particles and the fluid. Furthermore, these authors find that the thermal inertia of the particles acts as an additional stabilization factor, and this regardless of the temperatures of the injected particles. One might argue that the physical origin of this mostly mechanical stabilization effect comes from the fact that collectively the falling particles acts as a widespread negative buoyancy force, and that the effect might be reversed for particles that are lighter than the fluid. Indeed

it is well known that a rising bubble front can destabilize a quiescent fluid layer [83], and that bubbles are very effective to enhance mixing [84]. On the other hand, the stabilization might be due to the enhanced dissipation produced by the dispersed phase, that would reduce the effective Rayleigh number (as the latter can be seen as a ratio between buoyant and dissipative forces), similarly to what occurs for the RB instability in superdiffusive media[98]. According to the latter argument the particulate phase would lead to the fluid layer stabilization independently of its mass density and settling direction. This open question represents the primary motivation of the present study.

Our work extends the model adopted in [50] by considering particles of arbitrary mass density with respect to the fluid in order to encompass the cases of stone-like to bubble-like particles. This amount to take into account the role of the added mass hydrodynamic force. Remarkably, we find that the mechanical stabilization effect persists even for particles which are lighter than the flow, although the effect tends to vanish when the particle mass density becomes negligible with respect to the fluid one (such as for the case of bubbles). In this study we also further explore the influence of the combined thermo-mechanical coupling. The linear stability threshold for the onset of convection depends upon factors such as particle diameter and the specific heat capacity ratio of the particle and fluid phases. A thermal/kinetic energy budget analysis is used to validate the stability results and to reveal the thermal and mechanical coupling contributions to system stabilization. Finally we critically discuss the role of the key assumption taken in this study for the particle injection modelization and how their variation could lead to different dynamics, that deserve to be explored in the future.

5.2 Results and discussion

This section describes the main results on the onset of convection in the pRB model system (3.57)-(3.60) and boundary conditions (3.61)-(3.63), obtained by means of the linear stability analysis. Before venturing into this, it is worth briefly discussing the system's behavior in some limiting cases, which offer an easier insight. Notably, we first examine the case of small particles ($\Phi \to 0$) where a perturbative solution of the system is possible. Second, we consider what happens in the limiting cases of the thermal coupling, i.e. when particles are thermally ineffective for the fluid, $E = 0$, (pure mechanical coupling) and the opposite case when their particle thermal inertia is overwhelming, $E = +\infty$. The linear stability analysis will then focus on trends as

compared to different parameters: the fluid to particle mass density ratio (β), the particle size (Φ), the particulate volume flux ($\alpha_0 W_0$) and finally the particulate temperature (Θ_p^*) (that determines the particulate inlet heat flux).

5.2.1 Perturbative solution in the $\Phi^2 \to 0$ limit

If equations (2.43) and (2.45) are multiplied by Φ^2 then we can take the limit for $\Phi \to 0$ and the solution $\mathbf{W} = \mathbf{U}$ is readily obtained. This implies that for small values of Φ^2 the value of W should be close to the one of the fluid velocity $\mathbf{U}$. In the limit of small but non-vanishing Φ^2 a perturbative solution of the above equations can indeed be obtained. We consider that the solution of $\mathbf{W}$ and Θ_p will be of the form

$$\mathbf{W} \simeq \mathbf{U} + \Phi^2 \mathbf{W}_1 \ , \ \Theta_p \simeq \Theta + \Phi^2 \Theta_{p1}, \text{ and } \alpha = \alpha_0 + \Phi^2 \alpha_1.$$

Substituting these expressions into the equations for $\mathbf{W}$, Θ_p and α at the leading order in Φ^2 we obtain the following relations for the particle's variables:

$$\mathbf{W} = \mathbf{U} + \Phi^2 \frac{\beta - 1}{12 Pr \beta} \left(\frac{D\mathbf{U}}{D\mathcal{T}} + \Lambda \hat{\mathbf{Z}} \right), \tag{5.1}$$

$$\Theta_p = \Theta + \Phi^2 \frac{E}{12} \left(\frac{D\Theta}{D\mathcal{T}} \right), \tag{5.2}$$

$$\frac{D\alpha_0}{D\mathcal{T}} = 0, \qquad \frac{D\alpha_1}{D\mathcal{T}} = \frac{\alpha_0}{12 Pr} \frac{1-\beta}{\beta} \nabla \mathbf{U} : \nabla \mathbf{U}. \tag{5.3}$$

Taking this into account the fluid equations reduce to:

$$\frac{D\mathbf{U}}{D\mathcal{T}} = -\nabla P + Pr \nabla^2 \mathbf{U} + PrRa\Theta \hat{\mathbf{z}} + (\alpha_0 + \alpha_1 \Phi^2) \left[\frac{3(\beta - 1)}{2\beta} \left(\frac{D\mathbf{U}}{D\mathcal{T}} + \Lambda \hat{\mathbf{Z}} \right) \right], \tag{5.4}$$

$$\frac{D\Theta}{D\mathcal{T}} = \nabla^2 \Theta + (\alpha_0 + \alpha_1 \Phi^2) E \frac{D\Theta}{D\mathcal{T}}. \tag{5.5}$$

Introducing the boundary condition ($\alpha = \alpha_0$) the above equations simplify to:

$$\frac{D\mathbf{U}}{D\mathcal{T}} = -\nabla P' + \frac{Pr}{\left(1 - \alpha_0 \frac{3(\beta-1)}{2\beta}\right)} \nabla^2 \mathbf{U} + \frac{PrRa}{\left(1 - \alpha_0 \frac{3(\beta-1)}{2\beta}\right)} \Theta \hat{\mathbf{z}}, \tag{5.6}$$

$$\frac{D\Theta}{D\mathcal{T}} = \frac{1}{1 - \alpha_0 E} \nabla^2 \Theta, \tag{5.7}$$

where P' is a redefined pressure. Now redefining the time as $\tilde{\mathcal{T}} = \mathcal{T}/(1-\alpha_0 E)$. We obtain

$$\frac{D\tilde{\mathbf{U}}}{D\tilde{\mathcal{T}}} = -\nabla\tilde{P} + \frac{Pr(1-\alpha_0 E)}{\left(1-\alpha_0\frac{3(\beta-1)}{2\beta}\right)}\nabla^2\tilde{\mathbf{U}} + \frac{PrRa(1-\alpha_0 E)^2}{\left(1-\alpha_0\frac{3(\beta-1)}{2\beta}\right)}\Theta\hat{\mathbf{z}}, \tag{5.8}$$

$$\frac{D\Theta}{D\tilde{\mathcal{T}}} = \nabla^2\Theta, \tag{5.9}$$

which has the form of the usual Boussinesq system. It is linearly unstable for $Ra(1-\alpha_0 E) \gtrsim 1708$ at any value of Pr and β. This correction is always tiny in the range of parameters considered in this study. In fact we will consider at most $\alpha_0 E = 10^{-4}$.

5.2.2 Thermal coupling limiting cases

In this section we will present the thermal coupling limiting cases (i) $E \to 0$ and (ii) $E \to \infty$

Case (i) $E \to 0$

When the thermal specific heat capacity ratio (E) number is very small, fluid and particulate temperatures are strongly coupled so that $\Theta_p \approx \Theta$. Fluid and particle momentum equations are given by (3.57) and (3.58). The fluid energy equation will become,

$$\lambda\Theta_n + U_n D\Theta_0 - (D^2 - k^2)\Theta_n = 0, \tag{5.10}$$

and particle energy equation can be discarded.

Case (ii) $E \to \infty$

In case of extreme heat capacity ratio ($E \to \infty$) the temperature of the particulate phase does not change and also in this case particle energy equation can be discarded. We have to reconstruct the base state which follows from equations (2.44) and (2.45) as,

$$\partial_z^2\Theta_0 - \frac{12\alpha_0}{\Phi^2}(\Theta_0 - \Theta_p^*) = 0 \tag{5.11}$$

The expression for the fluid base state, as illustrated in Figure 5.1, is derived using equation (7.1). After substitution of the boundary conditions we get,

$$\Theta_0 = \frac{e^{-\frac{2\sqrt{3\alpha_0}z}{\Phi}}\left(-e^{\frac{\sqrt{3\alpha_0}}{\Phi}} + e^{\frac{2\sqrt{3\alpha_0}z}{\Phi}}\right)\left(\left(e^{\frac{2\sqrt{3\alpha_0}}{\Phi}} + e^{\frac{(1+2z)\sqrt{3\alpha_0}}{\Phi}}\right)(-1+\Theta_p^*) - \Theta_p^* - e^{\frac{(3+2z)\sqrt{3\alpha_0}}{\Phi}}\Theta_p^*\right)}{-1 + e^{\frac{4\sqrt{3\alpha_0}}{\Phi}}} \tag{5.12}$$

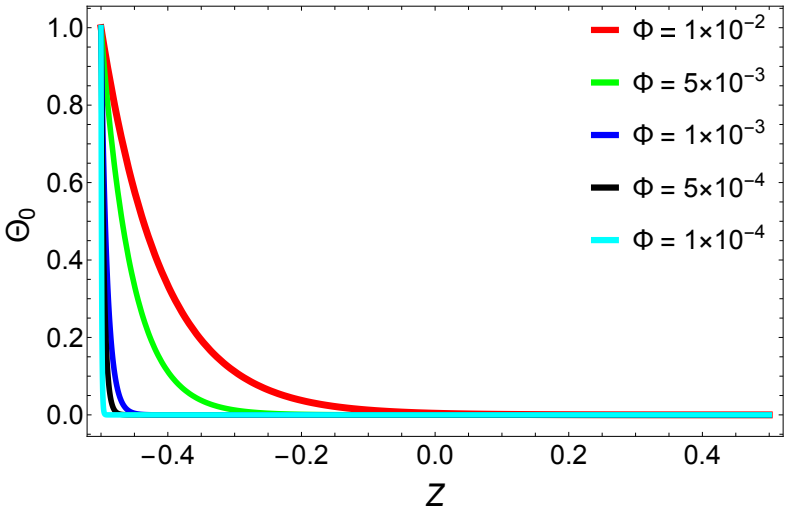

(a) $E = \infty$

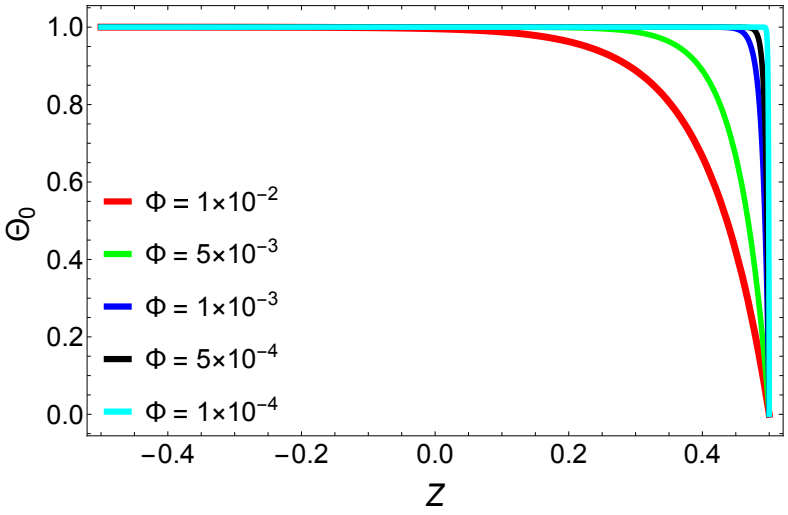

(b) $E = \infty$

Figure 5.1: The fluid temperature vertical distribution in the cell for different particle diameter Φ (a) heavy particles ($\beta = 0.5, \Theta_p^* = 0$) and (b) the light particles ($\beta = 1.5, \Theta_p^* = 1$).

5.2.3 Linear properties of the instability

In this section we present the effects of both heavy and light particles on the stability of the RB system. In addition to the Rayleigh and Prandtl numbers Ra and Pr, the presence of a particulate phase also introduces the following dimensionless parameters: the global particle volume fraction α_0, the added mass-adjusted fluid-to-particle density ratio β, the dimensionless particle diameter Φ, the heat capacity ratio E, the Galileo number Λ, and the dimensionless injection temperature of the particles Θ_p^*.

Parameter values for some representative systems of heavy and light particles are given in Table 5.1. The dimensionless parameters were obtained by considering a layer of height $H = 0.1m$. In order to simplify the analysis, we chose to take water as a representative working fluid and fix in all the calculations $\alpha_0 = 10^{-3}$, $\Lambda = 48 \times 10^{10}$ and $Pr = 5$. Even though we cannot prove that the principle of exchange of stabilities holds for the present problem, we found that the least stable modes have pure imaginary eigenvalues ($\lambda_i = 0$). In other words, the system undergoes a pitchfork bifurcation giving rise to stationary convection for all cases studied.

5.2.4 Effect of particle mass density

Let us first focus on the influence of β on the stability of the particulate RB system. The case $\beta = 1$ corresponds to neutrally buoyant particles, and at this particular value our model presents a singularity as the inlet particle flux can not be different from zero. Heavy particles ($\beta < 1$) are injected from the top with the cold wall temperature ($\Theta_p^* = 0$), and light particles ($\beta > 1$) are injected from the bottom with the hot wall temperature ($\Theta_p^* = 1$), unless specified otherwise. Figure 5.2 shows the critical thresholds as functions of β, for different values of the heat capacity ratio E. The limiting case $E = 0$ corresponds to instant thermal coupling, i.e. the particle and fluid temperature fields are the same. On the other hand, when $E \to \infty$ the particles temperature remains constant ($\Theta_p = \Theta_p^*$) and they act as internal heat source. One can remark that the introduction of particles, either heavy or light, stabilizes the system with respect to the single-phase RB threshold $Ra_c \simeq 1708$ and $k_c = 3.11$. The system becomes increasingly stable as the density of heavy particles increases (i.e., as β decreases from 1), and for large values of E the critical thresholds tend to the asymptotic values $Ra_c \sim 10^5$ and $k_c \sim 8$. On the contrary, as light particles become lighter (i.e., as β increases from 1), for large E the system experiences a sharp stabilization followed by mild decrease in Ra_c, until the limiting

glass/water			
ρ_p	$2.5 g/cm^3$	β	0.5
c_{Pp}	$0.84 J/g$	E	0.5
ρ	$1 g/cm^3$	Λ	48×10^{10}
c_p	$4.1813 J/g$	Pr	5
κ	$1.43 \times 10^{-7} m^2/s$		
ν	$10^{-6} m^2/s$		
polypropylene/water			
ρ_p	$0.86 g/cm^3$	β	1.1
c_{Pp}	$1.92\ J/g$	E	4×10^{-4}
ρ	$1 g/cm^3$	Λ	48×10^{10}
c_p	$4.1813 J/g$	Pr	5
κ	$1.43 \times 10^{-7} m^2/s$		
ν	$10^{-6} m^2/s$		
ice crystals/water			
ρ_p	$0.92 g/cm^3$	β	1.6
c_{Pp}	$2.09 J/g$	E	0.45
ρ	$1 g/cm^3$	Λ	48×10^{10}
c_p	$4.1813 J/g$	Pr	5
κ	$1.43 \times 10^{-7} m^2/s$		
ν	$10^{-6} m^2/s$		
air bubbles/water			
ρ_p	$0.001225 g/cm^3$	β	3
c_{Pp}	$1.005 J/g$	E	3×10^{-4}
ρ	$1 g/cm^3$	Λ	48×10^{10}
c_p	$4.1813 J/g$	Pr	5
κ	$1.43 \times 10^{-7} m^2/s$		
ν	$10^{-6} m^2/s$		

Table 5.1: Dimensional and dimensionless parameter values for some representative systems. The parameters are defined as follows: ρ_p: Density of the particle material, c: Specific heat capacity of the particle material, ρ: Density of the fluid, c_{Pf}: Specific heat capacity of the fluid, κ: Thermal diffusivity of the fluid, ν: Kinematic viscosity of the fluid, β: modified fluid-to-particle density ratio, E: Particle-to-fluid thermal heat capacity ratio, Λ: Galileo number, Pr: Prandtl number.

value $\beta = 3$. As it will be evident in the energy budget analysis of section 5.2.9, at this value of β, the stabilizing role played by the particles is entirely due to the thermal coupling. Indeed, the Stokes drag term in equation (3.57) vanishes for $\beta = 3$. Note that in the neutral stability state, the added mass term of this equation (which multiplies $\alpha_0(\beta - 1)/2$) does not affect the linear stability results since the bifurcation is stationary ($\lambda = 0$). Finally, by comparing the trends of Ra_c and k_c versus β (panels (a) and (b) of figure 5.2) an approximate proportionality relation is clearly noticeable. This is likely related to the form of the fluid temperature base state which is characterized by strong gradients near the top/bottom walls (respectively for heavy/light particles see Fig 3.5 and Fig. 3.6). This form of the temperature profile effectively reduces the height of the thermally unstable layer in the system. As a consequence the convective rolls at the onset appears only in these layers which are characterized by smaller horizontal wave vectors as compared to the RB case (as the rolls have approximately a unit aspect ratio) and by a Rayleigh number that roughly increases by a factor $(H/\lambda_c)^3$ (i.e. the ratio between the usual Rayleigh number based on the cell height and the effective Rayleigh number based on the of the roll height). That is why when k_c increases, Ra_c also increases.

5.2.5 Effect of volumetric particulate flux

One may wonder if the inlet particulate flux affects the stability of the overall system. This question is appropriate because the special choice of injecting particles at their terminal velocity $\boldsymbol{W_0}$ and at a prescribed fixed concentration α_0 implies that the particle volumetric flux $\mathcal{J} = \alpha_0 \boldsymbol{W_0}$ is a function of β. In figure 5.3(a), blue line, we show the dependence of the intensity of the particulate flux $|\mathcal{J}|$ as a function of β. Its qualitative behavior reflects some (but not all) of the features of the $Ra_c(\beta)$ curve of figure 5.2. The flux intensity is moderate for the case of bubbles, null for neutral particles, and progressively increasing and even diverging in the limit of very heavy particles. To better understand the impact of the particulate inlet flux on the instability as a function of the β-type of particle we carry on an additional stability calculation where the inlet flux is kept constant. The particles are still inserted in the system at their terminal velocity, $\boldsymbol{W_0}$, but their volume concentration α_0 is adjusted so that $|\mathcal{J}|$ is the same for all β. In particular, we fix $|\mathcal{J}|$ to the value adopted for bubbles ($\beta = 3$) or equivalently to the case of heavy particles with $\beta = 0.6$ (corresponding to the dashed horizontal line in 5.3(a). The results for two representative cases ($E = 0, 0.05$) are shown in figure 5.3(b).

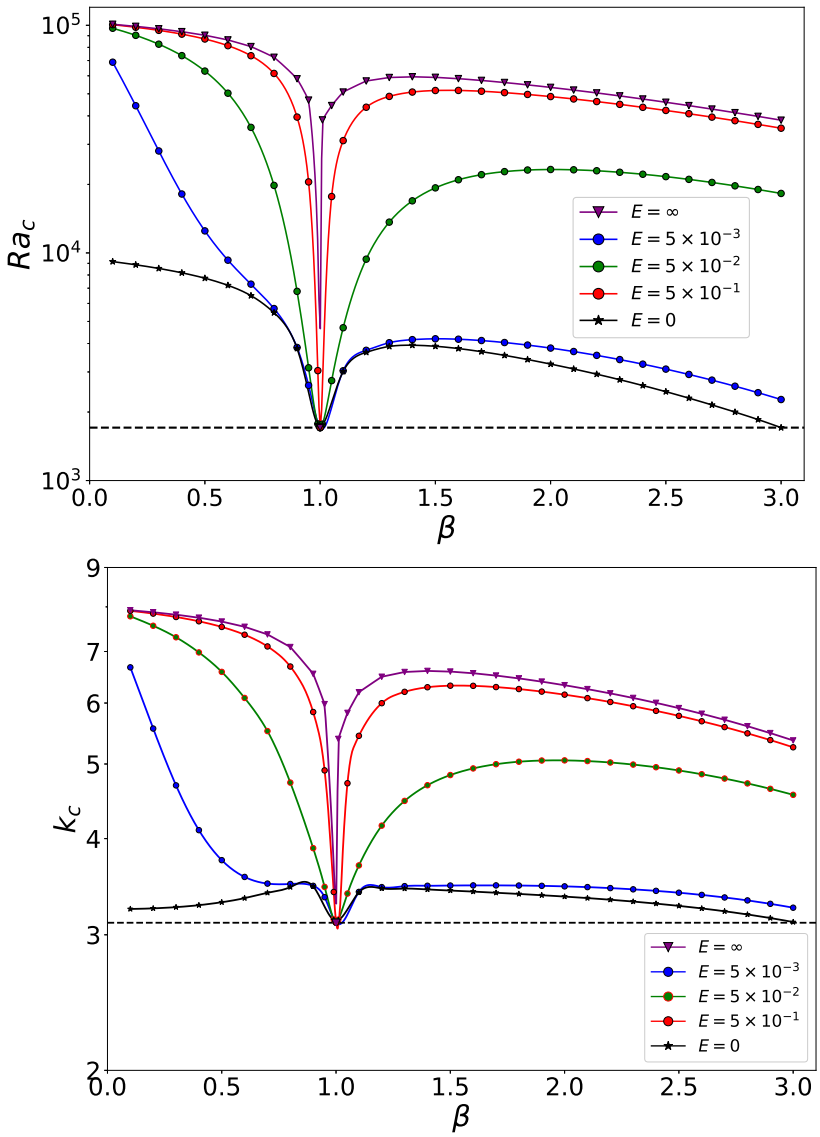

Figure 5.2: (a) Critical Rayleigh number and (b) corresponding wave number as function of the modified density ratio β. Results obtained for fixed $\Phi = 0.01$ and $\Theta_p^* = 0$ ($\beta < 1$), $\Theta_p^* = 1$ ($\beta > 1$). The horizontal dashed lines correspond to the single-phase Rayleigh-Bénard thresholds.

The curves, at fixed flux, have quite different trends. The extreme values of β point to a mild stabilization of the system, while a stronger stabilization (larger Ra_c values are attained for cases approaching neutral particles. The fact that these curves are not

flat, i.e. independent of β, confirms that the stabilization effect can not be completely ascribed to the intensity of the particulate inlet flux, and that particulate hydrodynamics forces and feedback do play a role in the stability of this model system.

5.2.6 Effect of particle size

Figures (5.4)-(5.5) illustrates the effects of the dimensionless particle diameter $\Phi = d_p/H$ on the stability thresholds of heavy and light particles respectively. The trends are similar for the two cases and for all values of the heat capacity ratio E: the critical Rayleigh number (wave number) remains close to the single-phase value for small Φ, then it quickly rises, reaches a maximum and then starts to decrease. This sharp increase on Ra_c can be explained as follows. From the particle momentum equation (3.58) in neutral conditions, and for $\lambda = 0$, one may infer that the magnitude of the velocity difference $|U_n' - W_n'|$ grows with Φ. This difference appears on the last term of the fluid momentum equation (3.57), which accounts for the drag exerted by the particles on the fluid (Stokes drag). Therefore, as Φ increases, this term gains importance, and as a consequence the flow is stabilized. This explanation can be confirmed by inspection of the eigenvectors of Figure 5.6, computed for $\beta = 0.5$, $E = 0.5$ and three values of Φ: just before the "jump" observed on Ra_c ($\Phi = 10^{-3}$), at the inflection point where Ra_c reaches a maximum ($\Phi = 4 \times 10^{-3}$), and after a smooth decrease on Ra_c ($\Phi = 6 \times 10^{-3}$). Before the jump, the particles diameter is relatively small, and the fluid and particle vertical velocity profiles are nearly the same. However, a significant difference can be observed on the eigenvectors obtained for larger values of Φ, meaning that the velocity difference $|U_z' - W_z'|$ is large enough to play a stabilizing role through the last term of equation (3.57). After the jump, the critical Rayleigh number decreases smoothly with increasing Φ. A possible explanation for this destabilization lies in the non-trivial role played by Φ on the fluid/particle thermal coupling, as Φ appears not only on the coefficients of equations (3.59) and (3.60), but also on the base state expressions Θ_0 and Θ_{p0}. This point will be further discussed in section 5.2.9. We remark that the destabilization of the flow with increasing particle diameter was also observed by Prakhar and Prosperetti (see Figs. 2 and 3 of [50]) with a similar model and for $\Phi \geq 0.01$.

The increase in Ra_c with the dimensionless particle diameter is accompanied by an increase on the critical wave number, as shown in Figure 5.4(b). This can be explained as follows. As Φ increases, the linear fluid temperature base profile turns into a nonlinear profile with important thermal gradients on the bottom of the layer (see Figure 3.5). As

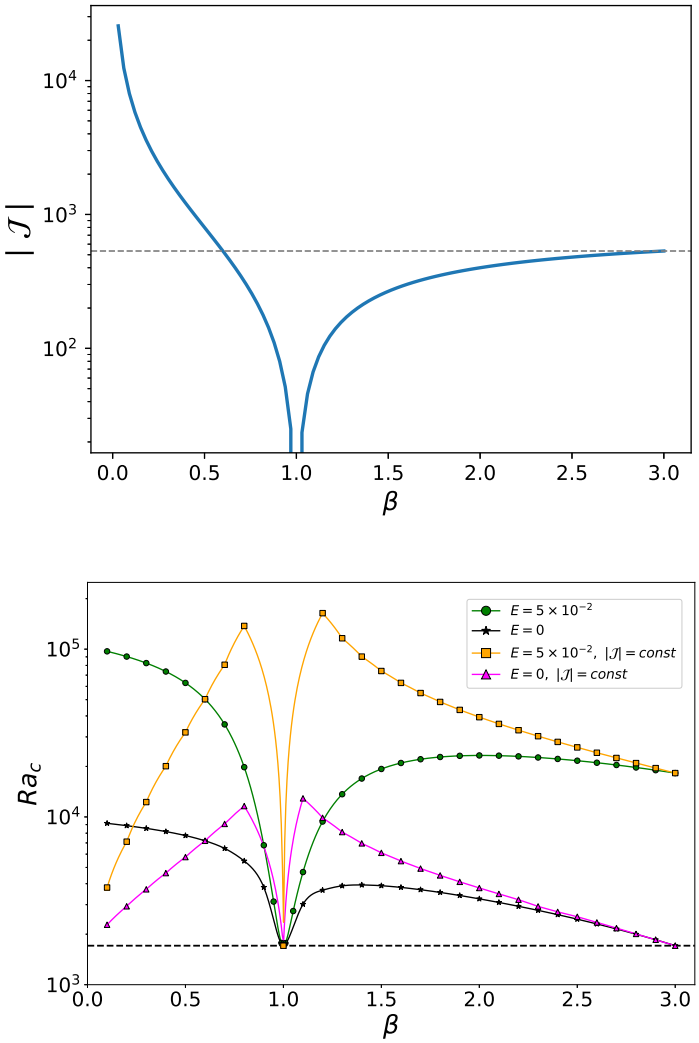

Figure 5.3: ((a) Intensity of the particulate volumetric inlet flux $\mathcal{J} = \alpha_0 W_0$ as a function of β. The horizontal dashed line corresponds to the reference flux intensity taken for the calculations at fixed flux presented in panel (b). (b) Critical Rayleigh number versus β for the cases of variable ($\mathcal{J} = \alpha_0 W_0$) and fixed inlet particle flux. In the second case, the fixed flux is taken equal to the case of $\beta = 3$ and $\beta = 0.6$. All the other conditions are the same as in figure 5.2. The horizontal dashed line correspond to the single-phase Rayleigh-Bénard threshold.

a consequence, convective rolls emerge in the bottom with a shorter wavelength (i.e. higher wave number). Then, convective motion which begins in the bottom layer drives

the movement in the upper (less unstable) part of the layer, as illustrated in Figure 5.7.

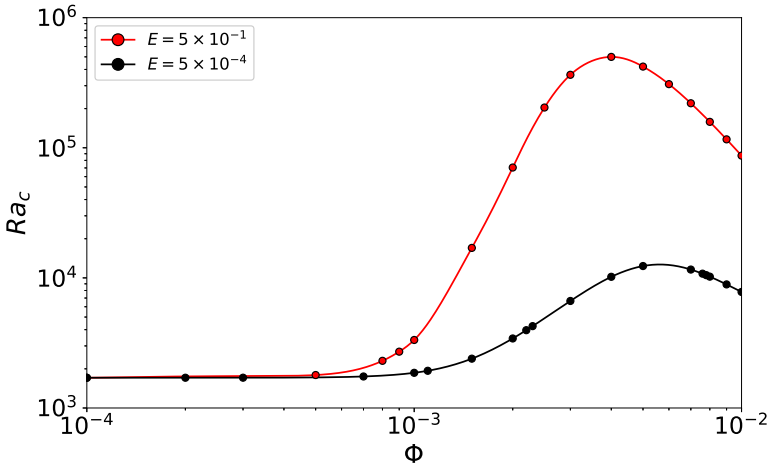

(a) $\beta = 0.5$

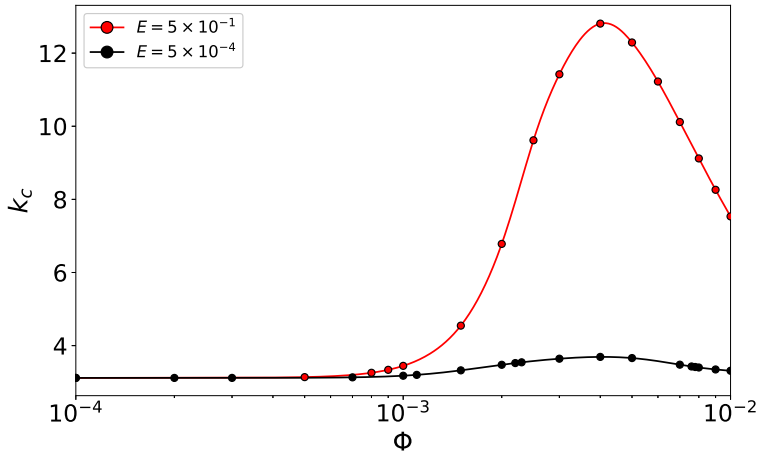

(b) $\beta = 0.5$

Figure 5.4: Evolution of the critical thresholds with particle diameter Φ, obtained for heavy particles with $\beta = 0.5$ and $\Theta_p^* = 0$.

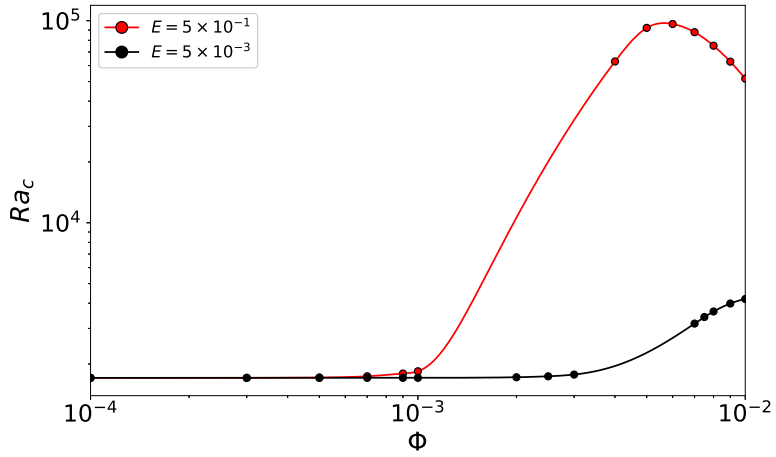

(a) $\beta = 1.5$

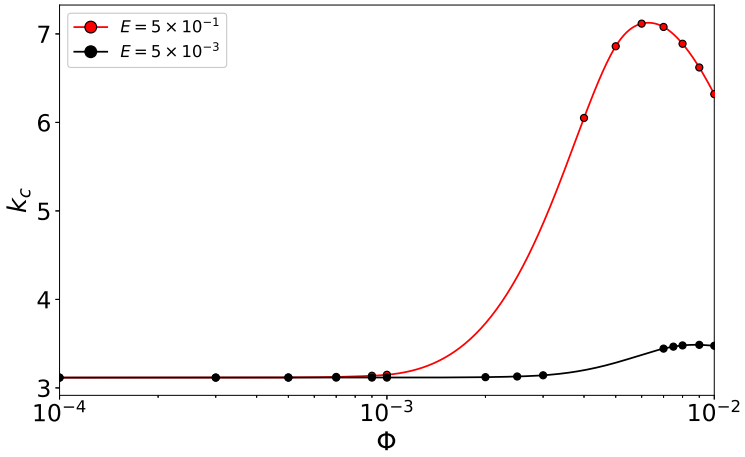

(b) $\beta = 1.5$

Figure 5.5: Evolution of the critical thresholds with particle diameter Φ, obtained for light particles with $\beta = 1.5$ and $\Theta_p^* = 1$.

5.2.7 Effect of volumetric heat flux

The stabilizing effect of the heat capacity ratio E illustrated in Figures 5.8 and 5.9 can be easily understood. The fluid/particle temperature difference increases with E. Indeed, the case $E \to 0$ corresponds to instant local thermal equilibrium between the fluid and

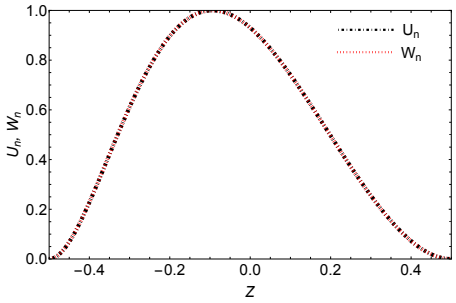

(a) $\Phi = 1 \times 10^{-3}$

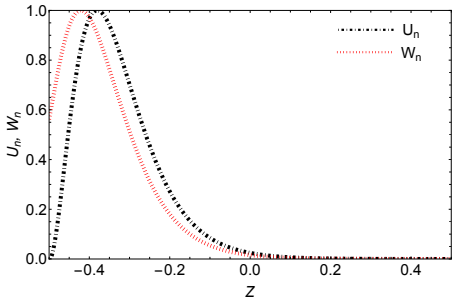

(b) $\Phi = 4 \times 10^{-3}$

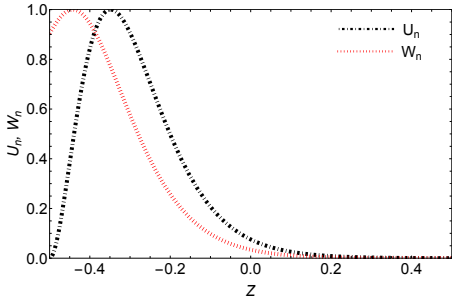

(c) $\Phi = 6 \times 10^{-3}$

Figure 5.6: Fluid and particles vertical velocity profiles at neutral conditions computed for parameters $\beta = 0.5$ and $E = 0.5$, illustrating changes in system behavior at three values of Φ: (a) just before the critical "jump" in Ra_c ($\Phi = 10^{-3}$), (b) at the inflection point where Ra_c reaches its peak ($\Phi = 4 \times 10^{-3}$), (c) and after the gradual decrease in Ra_c ($\Phi = 6 \times 10^{-3}$).

the particles, i.e. $\Theta' = \Theta'_p$, and to a linear base fluid temperature profile. When cold heavy particles ($\Theta^*_p = 0$) are being injected from above with a high thermal inertia (i.e. high E), particles are still cold when they get to the bottom, hence contributing to homogenize the fluid temperature within the layer. With smaller thermal gradients, the fluid gets stabilized. The inverse reasoning can be done for hot light particles being injected from the below ($\Theta^*_p = 1$). From Figures 5.8(a) and 5.9(a) one may also note that the stabilization provoked by E arrives earlier for larger particles. Following the behavior of Ra_c, a sharp increase is also observed on the critical wave number in Figures 5.8(b) and 5.9(b), which can be explained from the base fluid temperature profile as before.

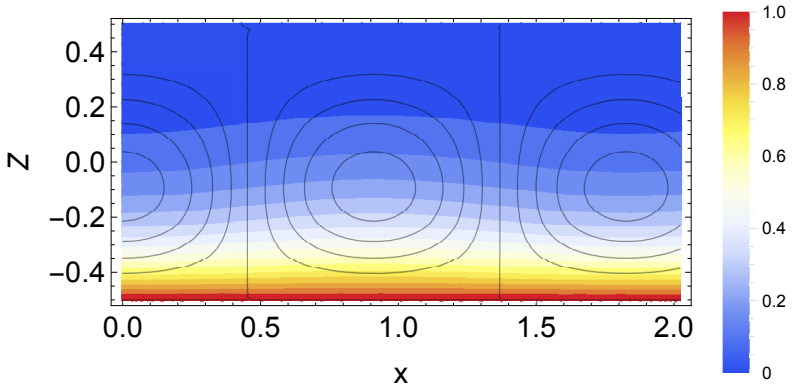

Figure 5.7: Iso-contours of the fluid velocity field and heatmap of the temperature for the set of parameters of Figure 5.6, showing the effect of particle diameter Φ on flow characteristics. The subfigures illustrate cases with (a) $\Phi = 1 \times 10^{-2}$, (b) $\Phi = 4 \times 10^{-3}$, and (c) $\Phi = 6 \times 10^{-2}$, all at $E = 5 \times 10^{-1}$ and $\beta = 0.5$.

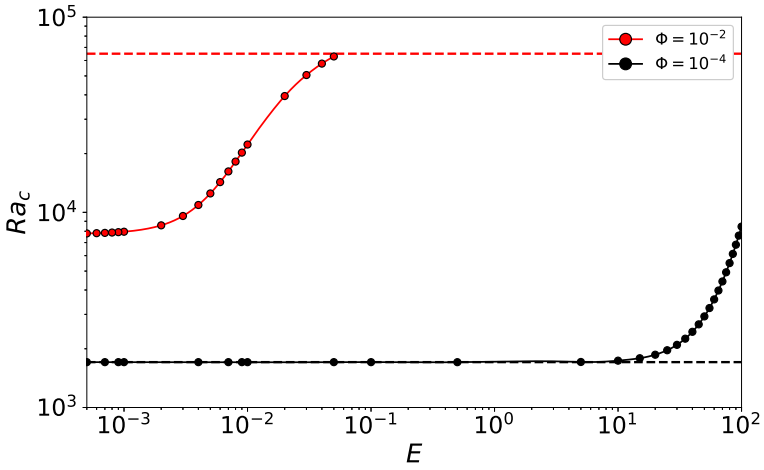

(a)

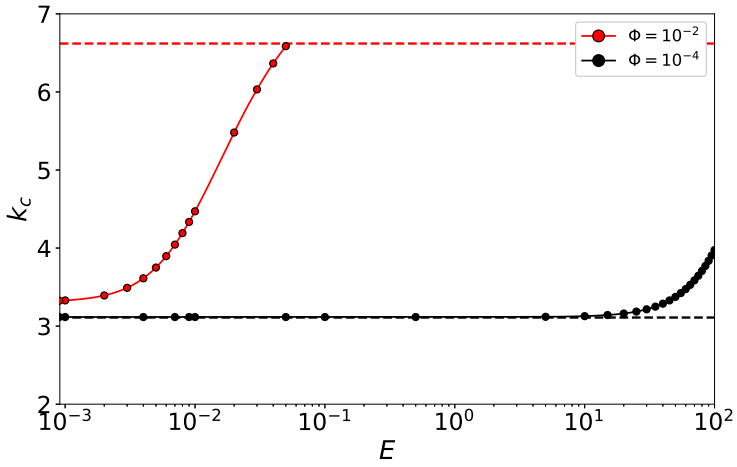

(b)

Figure 5.8: Evolution of the critical thresholds with the heat capacity ratio E, obtained for heavy particles with $\beta = 0.5$ and $\Theta_p^* = 0$. The red horizontal dashed line represents the limiting case $E \to \infty$, where the stability threshold remains constant, illustrating the asymptotic behavior of Ra_c. The horizontal black dashed line represents single-phase Rayleigh–Bénard thresholds.

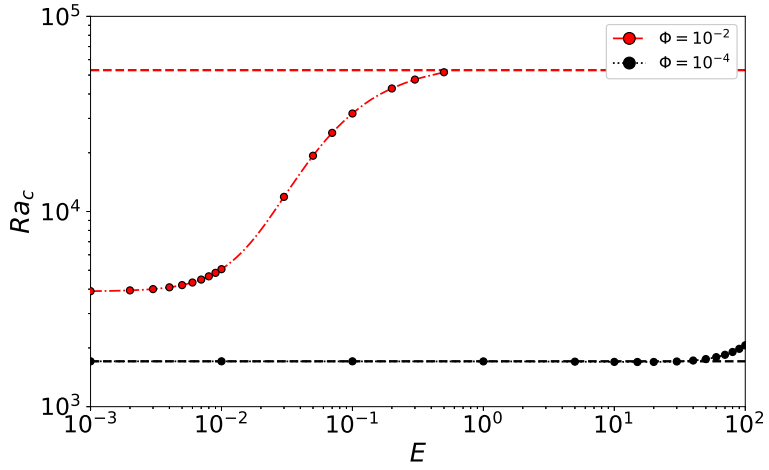

(a)

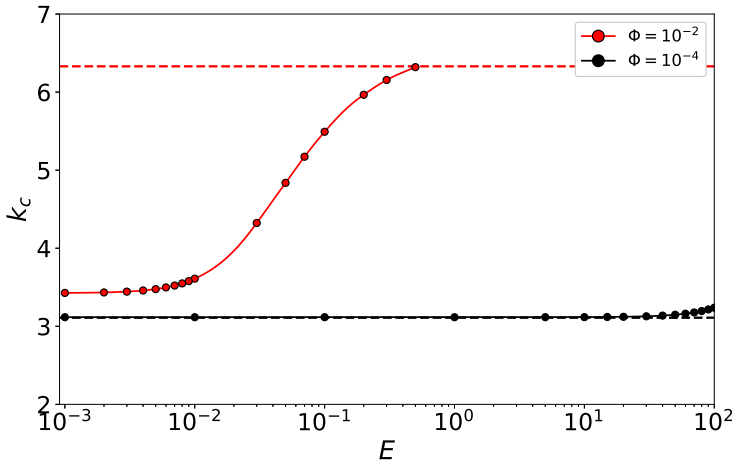

(b)

Figure 5.9: Evolution of the critical thresholds with the heat capacity ratio E, obtained for light particles with $\beta = 1.5$ and $\Theta_p^* = 1$. The red horizontal dashed line represents the limiting case $E \to \infty$, where the stability threshold remains constant, illustrating the asymptotic behavior of Ra_c. The horizontal black dashed line represents single-phase Rayleigh–Bénard thresholds.

5.2.8 Influence of injection temperature

Figure 5.10 shows the effect of particle injection temperature for heavy and light particles, with $E = 0.5$ and $\Phi = 0.01$. The observed trend is the same for both cases : the critical Rayleigh number increases, reaches a maximum and then starts to decrease. This behavior can be understood by inspecting the base temperature profiles of Figure 3.7. For $\Theta_p^* = -1$ one may observe a large region in the lower part of the system where the undisturbed vertical temperature gradient is destabilizing. By increasing the particle temperature to $\Theta_p^* = 0$, the extent of this region decreases and as a consequence, the system becomes more stable. This is the cause of the increase on the critical Rayleigh number observed in Figure 5.10. For $\Theta_p^* = 1$, the unstable part of the undisturbed temperature gradient is now located on the top of the cell (cf. Figure 3.7). The extent of this unstable region grows by further increasing particle temperature, which causes destabilization and hence, the decrease in Ra_c observed for $\Theta_p^* = 2$.

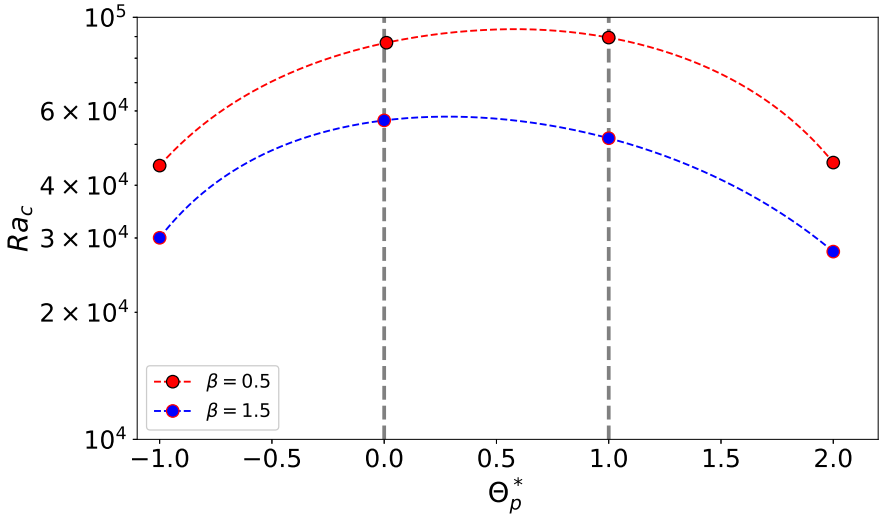

Figure 5.10: Evolution of the critical Rayleigh number with particle injection temperature for heavy and light particles for fixed $E = 5 \times 10^{-1}$ and $\Phi = 10^{-2}$.

5.2.9 Energy budget analysis

An *a posteriori* analysis of the energy transferred between the base state and the critical mode is here employed to identify the physical mechanisms leading to flow instability

and to validate the overall energy conservation of our neutral mode. To that end, we employ a methodology similar to the one presented in [132], and numerically evaluate all terms in the spatially averaged linearized energy and momentum conservation equations.

Thermal energy

From equation (3.59), the following relationship for the spatially averaged disturbance thermal energy e_Θ is obtained

$$\lambda e_\Theta = e_\Theta^{th} + e_\Theta^{diff} + e_\Theta^{fp}$$

with

$$e_\Theta = \int_{-1/2}^{1/2} \mathrm{Re}\left[|\Theta_n(z)|^2\right] dz, \tag{5.13}$$

$$e_\Theta^{th} = -\int_{-1/2}^{1/2} \mathrm{Re}\left[(U_n D\Theta_0)\bar{\Theta}_n\right] dz, \tag{5.14}$$

$$e_\Theta^{diff} = \int_{-1/2}^{1/2} \mathrm{Re}\left[(D^2 - k^2)(\Theta_n \times \bar{\Theta}_n)\right] dz, \tag{5.15}$$

$$e_\Theta^{fp} = -\frac{\alpha_0 12}{\Phi^2} \int_{-1/2}^{1/2} \mathrm{Re}\left[(\Theta_n - \Theta_{pn})(\bar{\Theta}_n)\right] dz, \tag{5.16}$$

where overbars denote the complex conjugate, e_Θ^{th} is the energy due to thermal advection, e_Θ^{diff} corresponds to the thermal dissipation energy. The energy exchange between particles and fluid as a result of drag forces is represented by e_Θ^{fp}. It quantifies how particle motion is impacted by the fluid resistance, which results in transfers of energy between particles and the surrounding fluid. The sign of the integrands determines whether the local energy transfer acts as a destabilizing (positive) or a stabilizing (negative) contribution. If the rate of change of the total energy e_Θ is positive, the basic flow is unstable, and vice-versa. Hence, the energy budget can also be used to verify the linear stability results since the rate of change of the total energy must vanish for the neutral modes. In our computations, such a condition is verified at the fifth digit. By normalizing the different contributions by the absolute value of the dissipation energy, we obtain at neutral conditions ($\lambda = 0$) :

$$E_\Theta^{th} + E_\Theta^{fp} = 1, \tag{5.17}$$

where $E_\Theta^{th} = e_\Theta^{th}/|e_\Theta^{diff}|$ and $E_\Theta^{fp} = e_\Theta^{fp}/|e_\Theta^{diff}|$.

Kinetic Energy

By following the same procedure, equation (3.57) leads to the ensuing relationship for the rate of change of the fluctuating kinetic energy e_K :

$$\lambda e_K = e^{th} + e^{diff} + e^{fp}, \tag{5.18}$$

with

$$e_K^{th} = PrRa \int_{-1/2}^{1/2} \mathrm{Re}\Big[(\Theta_n k^2)\bar{U}_n\Big] dz, \tag{5.19}$$

$$e_K^{diff} = -Pr \int_{-1/2}^{1/2} \mathrm{Re}\Big[(D^2 - k^2)^2 (U_n \times \bar{U}_n)\Big] dz, \tag{5.20}$$

$$e_K^{fp} = \frac{6\alpha_0 Pr(3-\beta)}{\Phi^2} \int_{-1/2}^{1/2} \mathrm{Re}\Big[(D^2 - k^2)(U_n - W_n) \times \bar{U}_n)\Big] dz, \tag{5.21}$$

After normalization, we obtain at neutral conditions ($\lambda = 0$) :

$$E_K^{th} + E_K^{fp} = 1, \tag{5.22}$$

where $E_K^{th} = e_K^{th}/|e_K^{diff}|$ and $E_K^{fp} = e_K^{fp}/|e_K^{diff}|$. Figure 5.11 reports the total thermal and kinetic energy budgets for the neutral modes as a function of the density ratio β. Results show that both the thermal and mechanical fluid/particle coupling contribute to the stabilization of the base state. Heavy particles present a more pronounced mechanical effect than light particles, while the thermal stabilization effect is more important for light particles. As the particles become lighter, the mechanical stabilization effect decreases, and as mentioned before, for $\beta = 3$ the contribution of Stokes drag is zero ($E_K^{fp} = 0$).

The total energy budgets for varying Φ are presented in Figure 5.12. One may note that the curves present roughly three regions with different slopes : $\Phi \lesssim 10^{-3}$, $10^{-3} \lesssim \Phi \lesssim 4\times10^{-3}$, and $\Phi \gtrsim 4\times10^{-3}$, corresponding to the three different slopes of Figure 5.4(a) for $E = 0.5$.

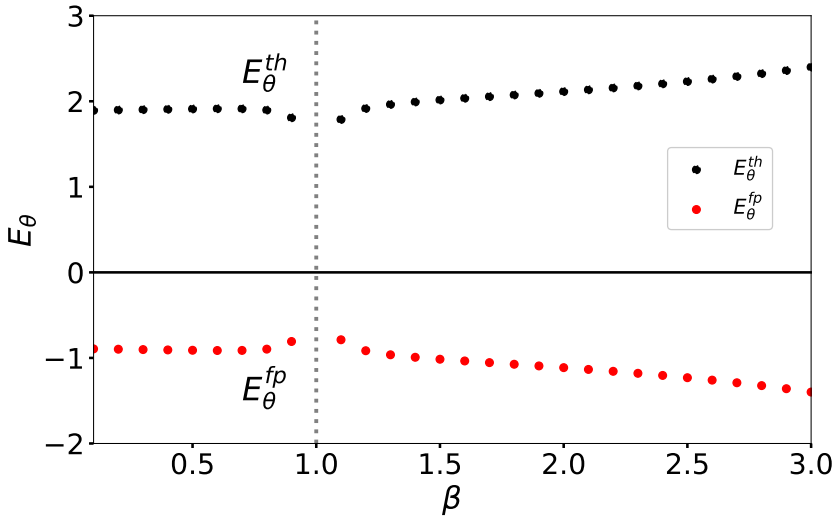

(a)

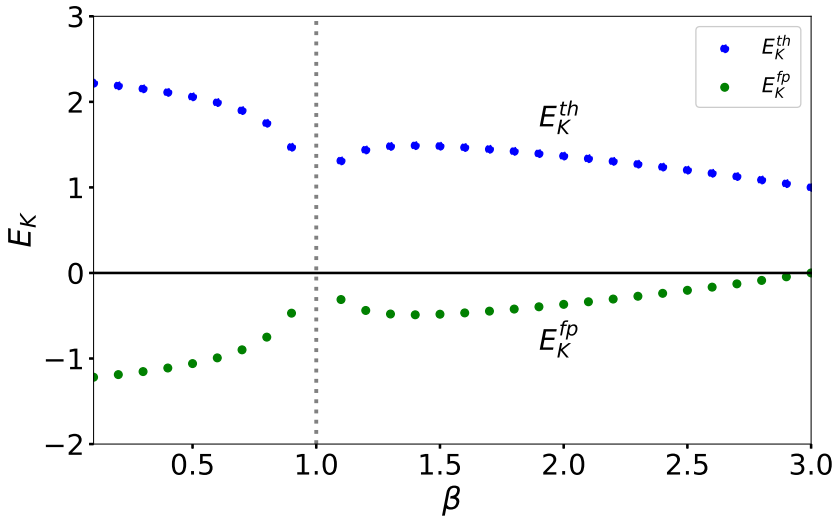

(b)

Figure 5.11: (a) Thermal and (b) Kinetic energy budgets for $E = 0.5$ and $\Phi = 0.01$.

5.3 Conclusions

We theoretically studied the effects of a diluted dispersed particulate phase on the onset of Rayleigh-Bénard (RB) convection in a fluid layer by means of a two-fluid Eulerian modelization. The particles are macroscopic, spherical, with inertia and heat capacity,

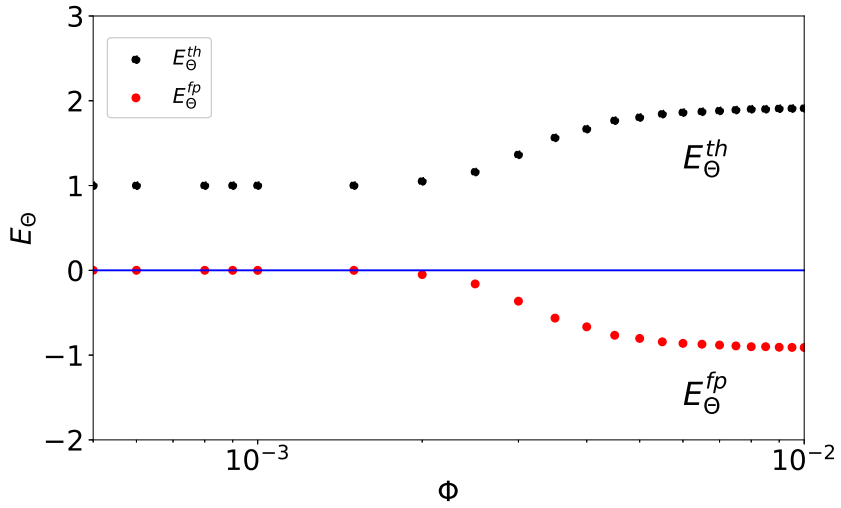

(a)

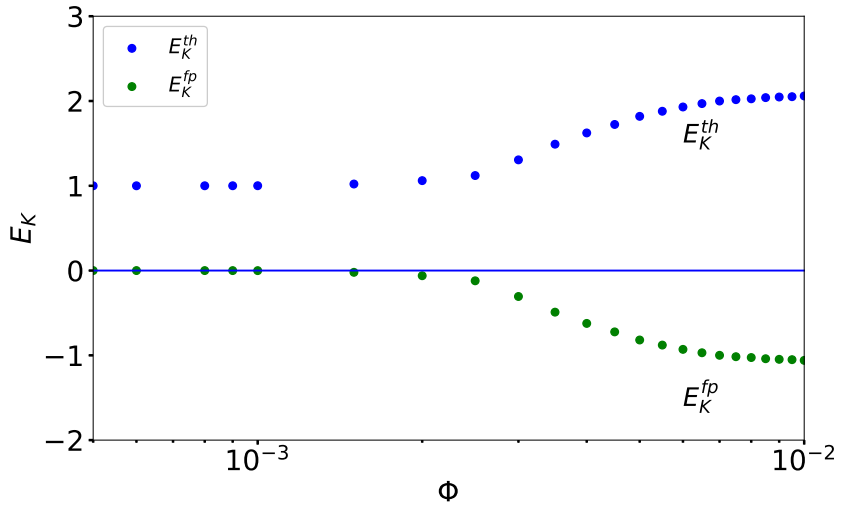

(b)

Figure 5.12: (a) Thermal and (b) Kinetic energy budgets for $E = 0.5$ and $\beta = 0.5$.

and are assumed to interact with the surrounding fluid mechanically and thermally. We examine both the cases of particles denser and lighter than the fluid that are injected uniformly at the system's top and bottom walls respectively, with their settling terminal Stokes velocity and prescribed temperatures. The presented linear stability analysis shows that the onset of thermal convection is stationary, i.e., the system undergoes

a pitchfork bifurcation as in the classical single-phase RB problem. Remarkably, the particle presence always stabilizes the system, increasing the critical Rayleigh number (Ra_c) of the convective onset. The limiting cases $E \to 0$ (when particles instantly adapt to fluid temperature) and $E \to \infty$ (when particles remain at their inlet temperature) were discussed in detail. The overall resulting stabilization effect on Ra_c is significant, reaching for a particulate volume fraction of 0.1% up to a factor 30 for the case of the lightest density particles and 60 for the heaviest ones. Particle diameter and inlet temperature have a non-monotonic effect due to nonlinear particle/fluid interactions that we have analyzed in detail. A thermal and kinetic energy budget analysis was also carried out, clarifying the role of the different thermal and mechanical contributions to the heavy and light particle systems.

In spite of the fact that the present model system accounts for the compressibility of the particulate velocity field and so can accommodate for the phenomenon of particle clustering, this aspect has not been explored in this study. Indeed, by simultaneously imposing the particle Stokes velocity and the particulate volume concentration at the inlet, we constrained the divergence of the particle velocity field to zero throughout the system. Although this assumption has the advantage of reducing the dimensionality of the problem (from eight to four scalar equations), this assumption is very restrictive and may have important consequences on the stability. Relaxing such a condition is possible for instance by imposing an inlet volume (or mass) flux of particles, however only at the price of more complex calculations. This may reconcile the apparent counterintuitive nature of our current results, where any kind of particle heavier/lighter than the fluid is capable to increase the system stability. Although we are not aware of experiments in the exact setting described by our pRB model system, as we already mentioned, it is well known that bubbles rising in a isothermal still fluid produce mechanical destabilizations that lead to enhance mixing and to convective like movements [83, 84, 52]. For this reason, it will be of primary interest to check how different boundary conditions, in particular resembling to the ones that could be realized in a laboratory experiment, may have consequences on the overall hydrodynamic stability of the system. Furthermore, as pointed out in [82, 51] the inclusion of the lift force for bubbles may also play key role in the fluid layer destabilization.

Chapter 6

Impact of particle injection velocity on the stability of the particulate Rayleigh-Bénard system

Outline of the current chapter

In the previous chapter, we investigated the influence of heavy and light particles injecting in he pRB system at their terminal velocity. Here, instead, we, explore the influence of particle injection velocity on the stability of the particulate Rayleigh–Bénard (pRB) system, providing new insights into how with this and particulate fluxes alter convective dynamics. The results presented here are based on the article *"Impact of Particle Injection Velocity on the Stability of the Particulate Rayleigh–Bénard System"*, published in Journal of Fluid Mechanics (JFM Rapids) coauthored with Romulo B. Freitas

, Leonardo S. B. Alves, Enrico Calzavarini1 and Silvia C. Hirata [172].

Our objective is to use a linear stability analysis to examine how variations in injection velocity modify the onset and development of convective instabilities in the pRB system. In particular, we focus on the contrasting responses of the flow when heavy particles are injected from above versus when light particles (or bubbles) are introduced from below.

The chapter is organized as follows. Section 6.1 introduces the problem and its context, whereas Sec. 6.2 is devoted to the detailed presentation and discussion of the results, focusing successively on the influence of particle mass density (Sec. 7.1.3), the impact of injection velocity and inlet flux (Sec. 6.2.2), particle concentration distributions at the onset of convection (Sec. 6.2.3), and the energy budget (Sec. 6.2.4). Concluding remarks are provided in Sec. 6.3.

6.1 Introduction

The stability of a quiescent fluid layer under the influence of a settling dispersed phase composed of particles, drops, or bubbles, is a fluid dynamic problem of remarkable richness and complexity [141, 143]. Even under highly idealized physical conditions, the problem statement involves a large number of physical parameters required to specify the material properties of both the fluid and the suspension, as well as all their boundary conditions. This is even more true when the couplings between the fluid and particles is not only mechanical but also energetic, involving e.g. temperature, phase-changes (melting, condensation, evaporation). In the case where the particles are small, very numerous, and highly diluted, an Eulerian two-fluid approach can be adopted to identify the parametric conditions under which they can destabilize the fluid, leading to large-scale advective motion [144].

Recently, [50] proposed studying a system in which a fluid layer is confined between two horizontal plates maintained at different temperatures, using heating from below to create an unstable density stratification (Rayleigh-Bénard configuration). In this system, particles heavier than the fluid are continuously introduced from the top wall, at their terminal velocity and prescribed temperature, and removed from the bottom one. This system, named particulate Rayleigh-Bénard (pRB), is shown to be more stable than the particle-free system. In other words, the Rayleigh number of the system must be larger than the $Ra_c \simeq 1708$ to trigger large-scale fluid motion, where Ra_c identifies the supercritical bifurcation point of a pure fluid system. Subsequently, [146] extended

the pRB model to particles of arbitrary density, including particles lighter than the fluid, which are injected from the lower plate at fixed temperatures. Even in this case, the system with particles is more stable than the particle-free system, regardless of the fluid-to-particle relative mass density and the strength of the mechanical and/or thermal couplings between the dispersed and continuous phases. The latter result appears to contradict the analysis of [51, 52], who demonstrated that the injection of bubbles from the bottom into an isothermal fluid layer is linearly unstable. Differently from the previously mentioned studies, these authors had considered the possibility of injecting bubbles at sub-terminal velocities, which is more realistic with respect to experiments. This fact has an important technical consequence in the linear stability problem, it allows the particle concentration to develop spatial inhomogeneities, which are prevented when the particles are injected at terminal velocity. Nakamura *et al.* observed that the variation of the injection velocity does not affect the system stability, unless the velocity is very close to the terminal rising velocity.

These issues raise the question of the role of particle injection velocity in the pRB system, and whether there exists specific combinations of injection velocities and particle densities allowing the system to be de/stabilized and, thus, controlled. They are addressed in the present study by improving the linear stability analysis of [146], where the particle injection velocity was set equal to the terminal velocity. Doing so shows that the system can be either stabilized or destabilized by properly tuning the particle inlet velocity and flux, where heavy and light particles induce opposite trends.

6.2 Results and discussion

The following section discusses the results obtained from solving the pRB system (3.28)–(3.33) in conjunction with the boundary conditions (3.34)–(3.35). Since the present study focuses on the influence of particle inlet velocity on the model stability, the following parameters are kept constant throughout the analysis: $Ga = 9.8 \times 10^9$, $Pr = 5$, $E = 5 \times 10^{-3}$, $\Phi = 10^{-2}$. Heavy particles are injected from the top with the cold wall temperature $\Theta_p^* = 0$, while light particles are injected from the bottom with the hot wall temperature $\Theta_p^* = 1$. Furthermore, the inlet flux was varied with respect to a reference value $\mathcal{J} = \mathcal{J}_0 = 533.3$. Finally, the thermal feedback of the particles to the fluid is assumed negligible in the present work since $E \ll 1$.

6.2.1 Influence of particle mass density

The first thing to notice is that the linear onset of instability is characterized by a pitchfork bifurcation in the parameter space explored here. In other words, the oscillatory frequency λ_i is always zero. Second, the effects of the modified density ratio on the critical thresholds under different particle inlet velocity are presented in figure 6.1. For heavy particles sedimenting from the top ($\beta < 1$), an increase in the inlet velocity leads to a decrease in the critical Rayleigh number, thereby destabilizing the system. Conversely, for light particles injected from the bottom ($\beta > 1$), the trend is reversed, with higher inlet velocities promoting stabilization. The most unstable cases occur for sub-terminal particle velocities. Notably, for $\beta > 2.8$ and $W^*/W_T = 0.5$, the critical Rayleigh number for the pRB modal falls below that of the single-phase RB system, indicating that a weakly injected particulate-phase can promote instability in the case of light particles and bubbles. It should be noted that the case of neutrally buoyant particles ($\beta = 1$) is singular, since one would have to inject an infinite amount of particles to keep the volumetric particulate flux constant. As illustrated in figure 6.1(b), the critical wave number slightly decreases with increasing inlet particle velocity for both heavy and light particles, though this decrease is more pronounced in the latter case.

6.2.2 Impact of partice injection velocity and inlet flux

Figures 6.2(a-d) show the effect of the particle inlet velocity on the critical thresholds under different inlet volumetric flux intensities for selected values of the modified density ratio. For the case of bubbles ($\beta = 3$), increasing the inlet flux is destabilizing for low inlet velocities but stabilizing otherwise, since all three curves intersect at $W^*/W_T \sim 0.6$. A similar trend is observed for all light particle cases, though the value of W^*/W_T where the intersection occurs decreases as β decreases. For $\beta \lesssim 2.5$, no intersection is observed and the increase in the particle flux always plays a stabilizing role. It is also worth pointing out that, for $\beta = 3$ and $\mathcal{J} = 1.5\mathcal{J}_0$, the critical Rayleigh number becomes negative for low enough values of W^*/W_T. This means that bubbles can trigger convective instabilities even when the pRB model is heated from above. As discussed by [52], this is due to a potentially unstable density stratification within the liquid-gas mixture near the bottom wall. As the bubble velocity increases to its terminal velocity, the volume fraction in this region decreases from $\mathcal{J}/W^*$ to $\mathcal{J}/W_T$, increasing the possibility of a locally unstable density gradient.

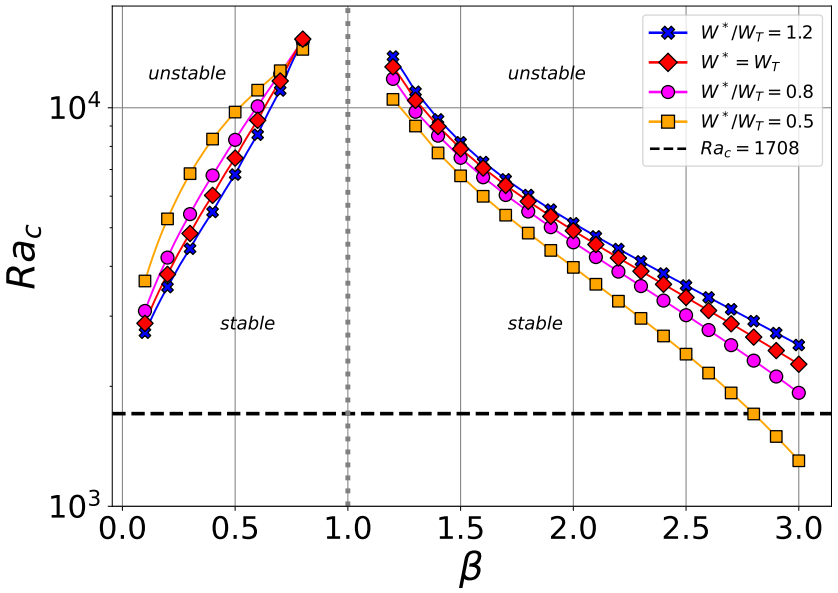

(a)

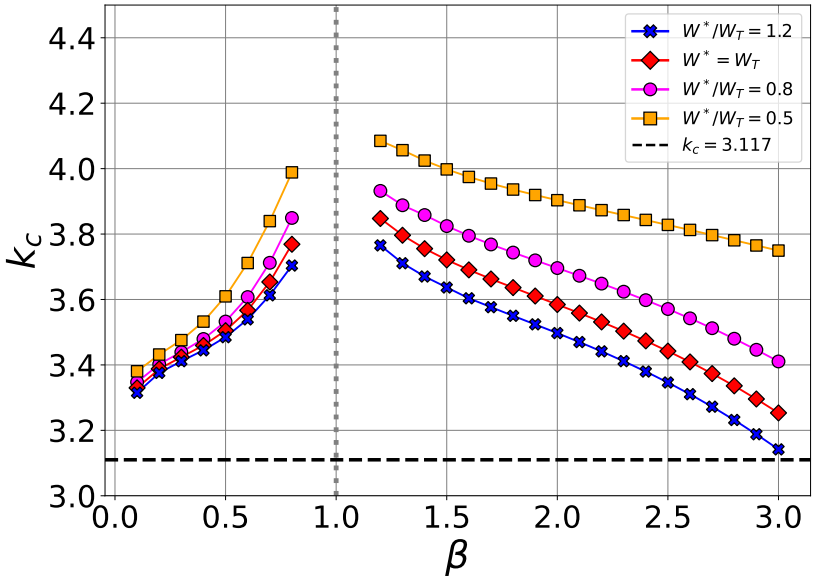

(b)

Figure 6.1: Variation with the density ratio β of the critical Rayleigh number Ra_c (a) and wave vector k_c (b). Calculations for various inlet velocities W^* are shown, from sub-terminal $< W_T$ to super-terminal $> W_T$. For comparison the values Ra_c, k_c corresponding to the single-phase RB system, are drawn as horizontal lines. The particle inlet flux is $\mathcal{J} = \mathcal{J}_0$.

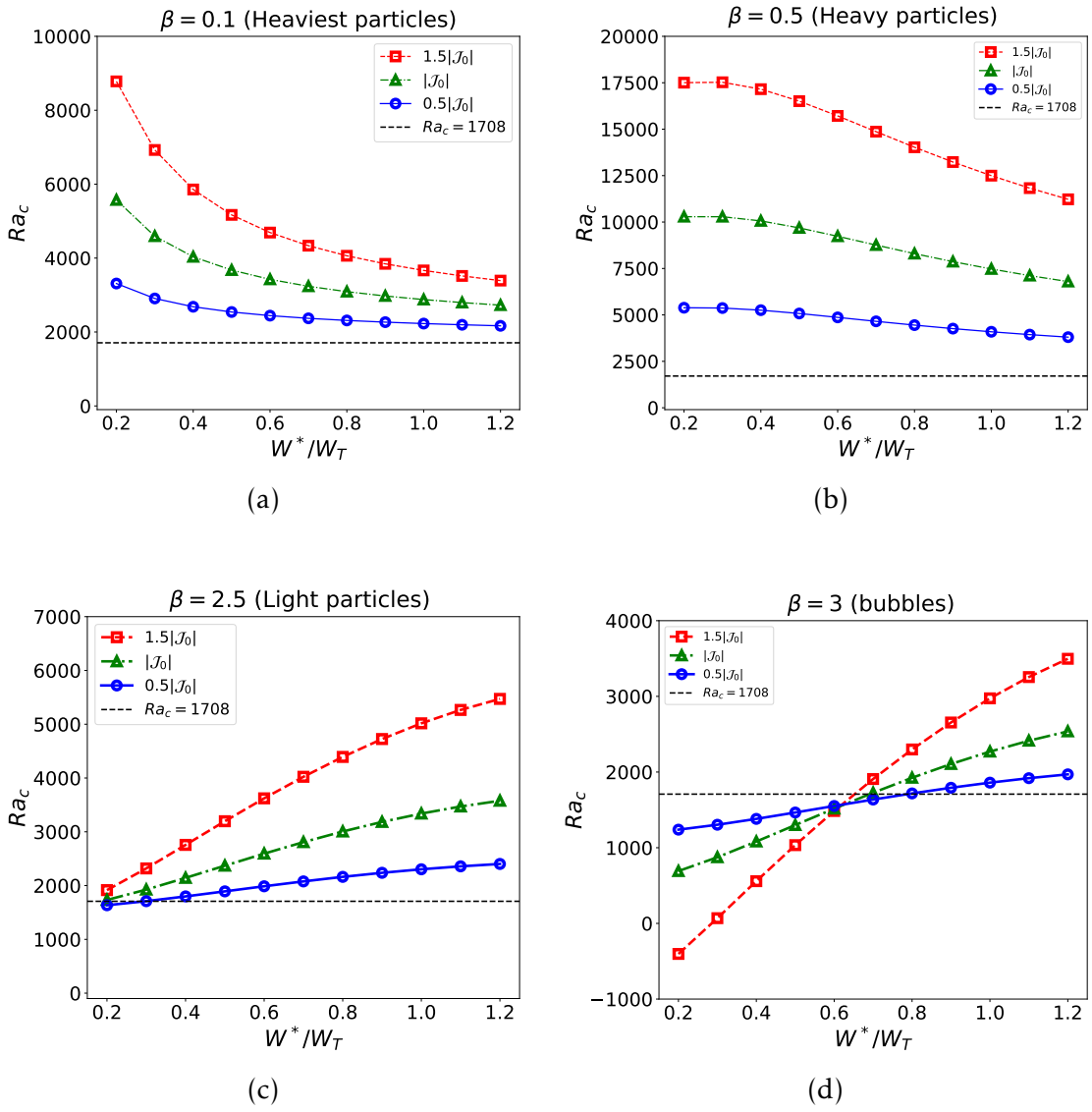

Figure 6.2: Critical Rayleigh number as a function of the inlet velocity for three different particle fluxes. The horizontal dashed lines correspond to the single-phase RB threshold.

For heavy particles, e.g. figures 6.2(a) and 6.2(b), increasing the particle inlet flux is always stabilizing, but the effect is more pronounced at low inlet velocities. Additional simulations were conducted for heavy particles, exploring higher values of both particle flux and inlet velocity, within the validity range of the present model. In all cases, the critical Rayleigh number remained above the RB threshold, providing strong evidence that it is not possible to destabilize the RB model by adding heavy particles. Furthermore, figures 6.3(a)-(d) show that the wave number dependence on both particle flux and inlet velocity is relatively weaker. This means that the size of the convective cells at the onset of convection are not significantly different from their single-phase RB counterparts. Such a difference becomes more pronounced, however, for very slow-rising bubbles at high volumetric inlet rates, as illustrated by the red line in figure 6.3(d).

6.2.3 Particle concentrations at the onset

Streamlines and particle concentration at the onset of convection are plotted in figure 6.4 and 6.5, through the eigenvectors of the perturbed fluid velocity $\boldsymbol{U}'$ and particle distribution α', for both heavy and light particles. Heavy particles figure 6.4(a-b) accumulate near the bottom. For sub-terminal (super-terminal) inlet velocities, a higher particle volume fraction is observed in the downwelling (upwelling) plumes. The particular case where $W^* = W_T$ is not shown for conciseness as it is already known that it possess a uniform particle distribution [146]. The opposite behavior is observed for light particles 6.5(d-f). They accumulate near the top, with upwelling (downwelling) plumes favoring higher concentrations for sub-terminal (super-terminal) velocities. Finally, when comparing figures 6.4(c) and 6.5(f), it can be observed that heavy particles ($\beta = 0.5$) tend to accumulate closer to the walls than light ones ($\beta = 3$) at super-terminal velocities ($W^*/W_T = 1.2$).

6.2.4 Energy budget analysis

An energy budget analysis is performed in order to gain further insights into the physical mechanisms triggering instabilities in the pRB system. In order to derive the evolution equation for the perturbation kinetic energy, we take the product of the momentum equation (3.29) and the complex conjugate of the vertical fluid velocity, $\bar{U}_z^n$, where the overbar denotes complex conjugate. By integrating the resulting equation over the entire domain, the following relationship for the spatially averaged perturbation kinetic energy

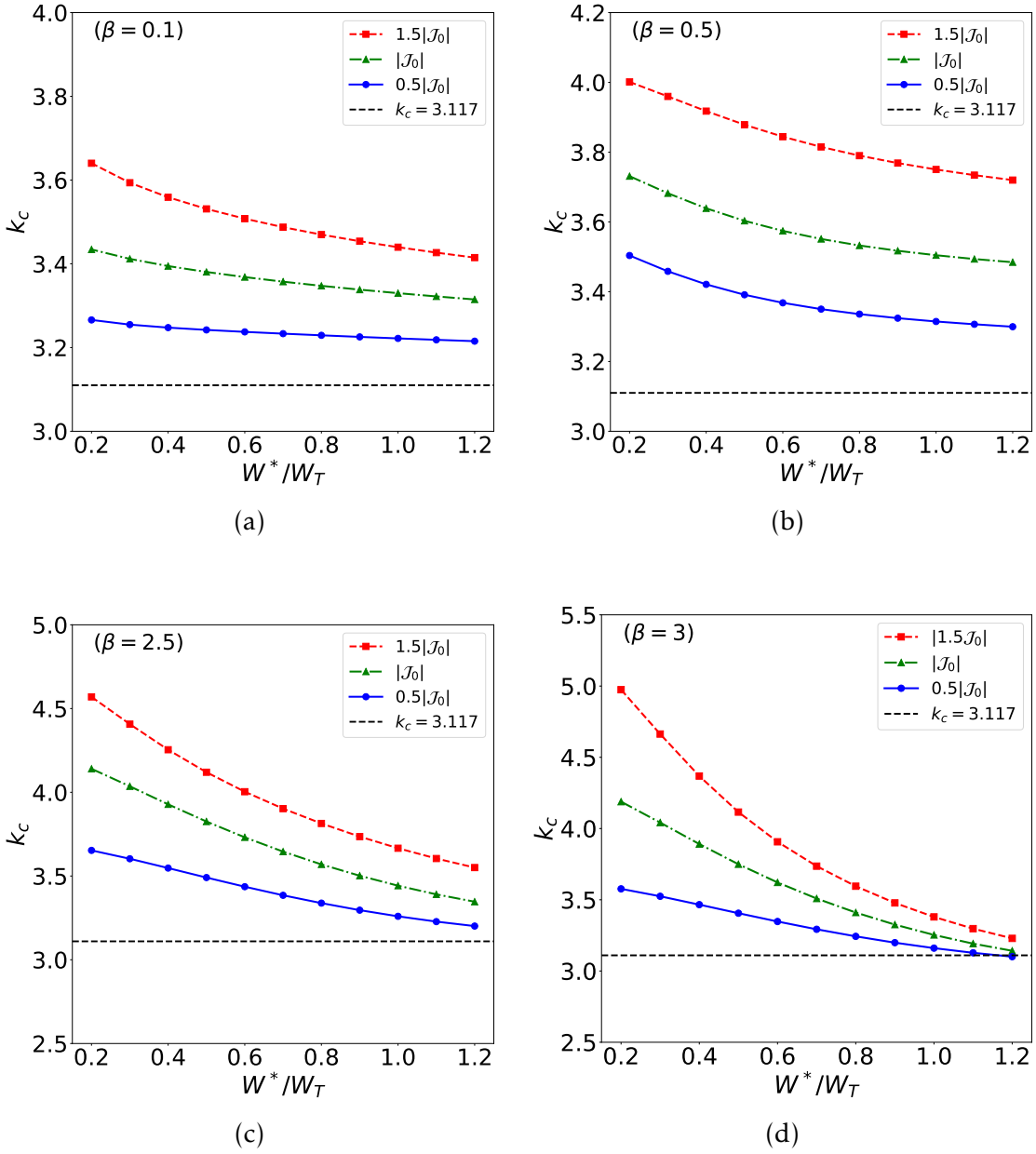

Figure 6.3: Critical wave number as a function of the inlet velocity for three different particle fluxes. The horizontal dashed lines correspond to the single-phase RB threshold.

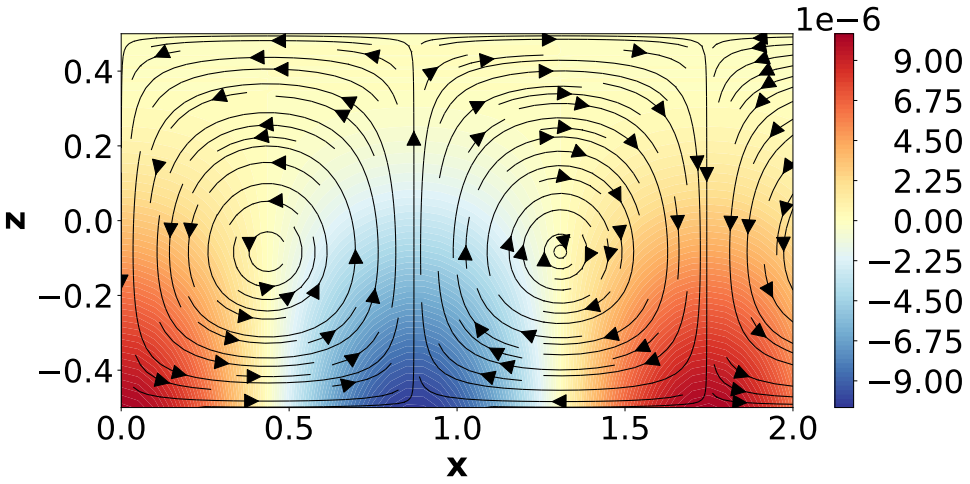

(a) $\beta = 0.5,\ W^*/W_T = 0.5$

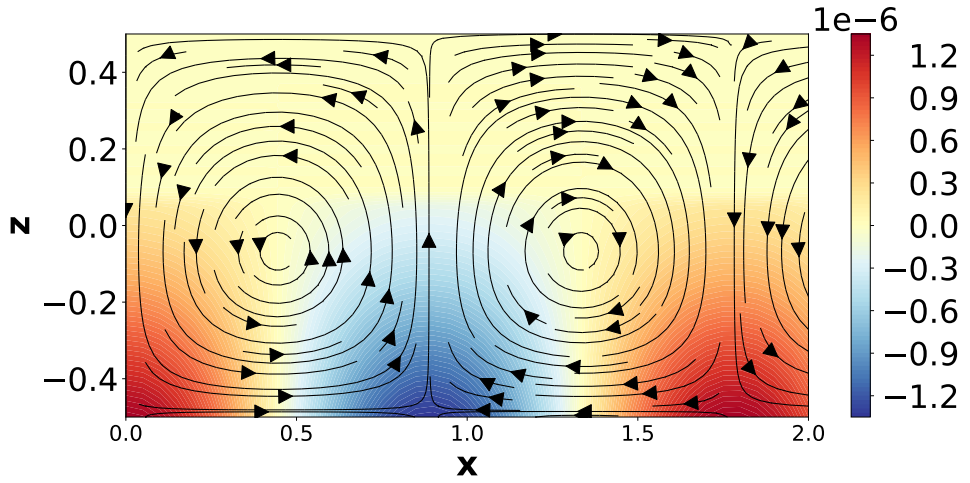

(b) $\beta = 0.5,\ W^*/W_T = 0.8$

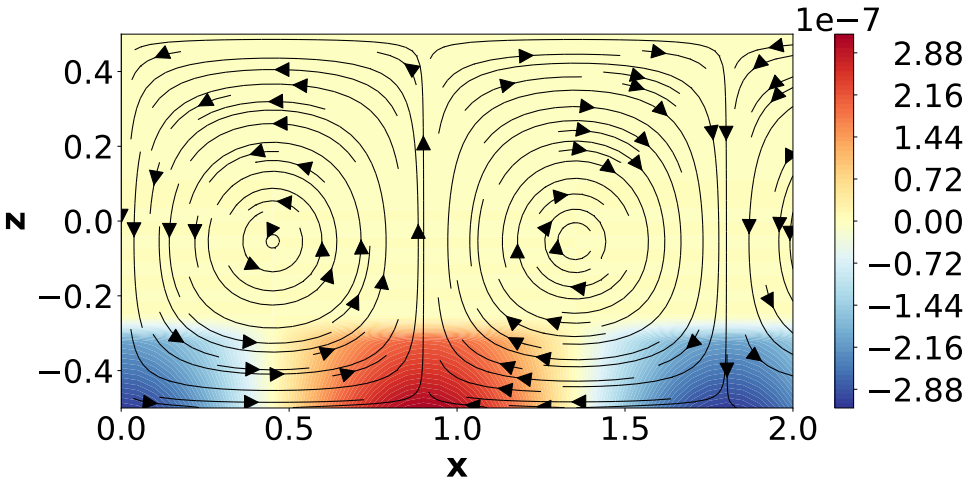

(c) $\beta = 0.5,\ W^*/W_T = 1.2$

Figure 6.4: Streamlines of fluid velocity field and colormap of the particle volume fraction at the onset of convection for $\beta = 0.5$ and increasing inlet velocities from top to bottom. For a better comparison, the particle volume fraction α' is normalized with respect to the base volume fraction α_0 for $\beta = 3$ and $W^* = W_T$ particles. The particle inlet flux is $\mathcal{J} = \mathcal{J}_0$

rate is obtained:

$$\lambda\, e^K = e^\Theta + e^V + e^{\alpha_0 W} + e^{\alpha W_0} + e^{\alpha Ga}, \tag{6.1}$$

with each term in this equation being defined as:

$$\begin{aligned} e^K &= \left(1 - \tfrac{\alpha_0}{2}(\beta-1)\right) \int_{-1/2}^{1/2} \mathrm{Re}\left[(D^2-k^2)(U_z^n)\bar{U}_z^n\right] dZ \\ &\quad + \tfrac{(\beta-1)}{2} \int_{-1/2}^{1/2} D\alpha_0\, \mathrm{Re}\left[D(U_z^n)\bar{U}_z^n\right] dZ, \end{aligned} \tag{6.2}$$

$$e^\Theta = \mathrm{Pr}\cdot\mathrm{Ra} \int_{-1/2}^{1/2} \mathrm{Re}\left[(\Theta^n k^2)\bar{U}_z^n\right] dZ, \tag{6.3}$$

$$e^V = -\mathrm{Pr} \int_{-1/2}^{1/2} \mathrm{Re}\left[(D^2-k^2)^2(U_z^n)\bar{U}_z^n\right] dZ, \tag{6.4}$$

$$\begin{aligned} e^{\alpha_0 W} &= \frac{6\,\mathrm{Pr}(3-\beta)}{\Phi^2}\Bigg[\int_{-1/2}^{1/2} \alpha_0\, \mathrm{Re}\left[(D^2-k^2)(U_z^n)\bar{U}_z^n + (ikDW_x^n + k^2 W_z^n)\bar{U}_z^n\right] dZ \\ &\quad + \int_{-1/2}^{1/2} D\alpha_0\, \mathrm{Re}\left[(ikW_x^n)\bar{U}_z^n + D(U_z^n)\bar{U}_z^n\right] dZ \Bigg], \end{aligned} \tag{6.5}$$

$$e^{\alpha W_0} = \frac{6\,\mathrm{Pr}(3-\beta)}{\Phi^2} \int_{-1/2}^{1/2} W_0\, \mathrm{Re}\left[(\alpha^n k^2)\bar{U}_z^n\right] dZ, \tag{6.6}$$

$$e^{\alpha Ga} = \frac{(\beta-1)\,Ga\,\mathrm{Pr}^2}{2} \int_{-1/2}^{1/2} \mathrm{Re}\left[(\alpha^n k^2)\bar{U}_z^n\right] dZ, \tag{6.7}$$

where e^Θ is the power of the thermal buoyancy force, e^V indicates the rate of viscous energy dissipation. Furthermore, $e^{\alpha_0 W}$, $e^{\alpha W_0}$ and $e^{\alpha Ga}$ collectively represent the particle feedback, i.e. the parts due to the base particle concentration, base particle velocity and particle buoyancy, respectively. The first two terms represent the drag force, while the latter represents the Archimedes force. The superscript α denotes the terms arising from the non-homogeneous distribution of particles, which are absent if $W^* = W_T$ as in [50, 146]. By normalizing these contributions using the absolute value of the dissipation rate, we obtain at neutral condition ($\lambda = 0$):

$$E^\Theta + E^{\alpha_0 W} + E^{\alpha W_0} + E^{\alpha Ga} = 1. \tag{6.8}$$

Figure 6.6 shows the aforementioned normalized kinetic energy rates versus the particle inlet velocity for different particle fluxes $\mathcal{J}$ and density ratios β. Positive (negative) contributions indicate destabilization (stabilization) of the steady-state. Heavy-particle

cases (figures 6.6(a, b)) show a competition between the destabilizing thermal buoyancy and the stabilizing particle drag feedback. Hence, heavy particle action is purely dissipative as their friction opposes the thermal buoyancy. However, the energy injection due to particle buoyancy $E^{\alpha Ga}$ is always negligible in the present study. This is at odds with the light particle cases (figures 6.6(c, d)) where the particle buoyancy term turns out to be important. Here $E^{\alpha Ga}$ is destabilizing when the injection velocity is smaller than the terminal one, while the opposite is true otherwise. This highlights the importance of the direction of particle motion, namely ascending or descending, as well as the sign of their acceleration, which determines whether the particle concentration near the injection wall is diluted or intensified. We note that in the special case of bubbles (figure 6.6(d)), where the drag terms $E^{\alpha_0 W}$ and $E^{\alpha W_0}$ vanish by definition according to equations (6.5–6.6), the competition is solely between the thermal and particle buoyancies.

6.3 Concluding remarks

The present investigation highlighted how the particle inlet velocity influences the linear stability of the pRB system. Increasing the inlet velocity while maintaining a constant particle flux destabilizes the system for heavy particles but progressively stabilizes it for light particles. While the general features of particle accumulation persist across the range of inlet velocities, the spatial localization of accumulation shifts between upwelling and downwelling regions as the injection speed transitions from sub-terminal to super-terminal values. When the injection velocity matches the terminal velocity, the linearized system dynamics does not support the accumulation of particles. In that case particle accumulation could arise only through nonlinear interactions as shown by [54]. In this study the thermal coupling was deliberately minimized in order to isolate the effects of the mechanical coupling introduced by the injection velocity. This was achieved by maintaining $E \ll 1$ and setting the particle inlet temperature equal to the inlet-wall temperature. Nevertheless, particle thermal inertia and injection temperature offer alternative mechanisms for influencing the flow onset within this model. Preliminary investigations in this direction [145] indicate that increasing E consistently enhances system stability when particles are heavier than the fluid, regardless of the volumetric particle flux, injection velocity, or injection temperature. In contrast, for particles lighter than the fluid, the effects are more complex: the influence of E can be either stabilizing or destabilizing, depending on the inlet velocity and particulate volumetric flux. This suggest that the effects of momentum coupling dominate over

the thermal ones. However, we shall note that the parameter E depends on the relative density between the particles and the fluid, in fact $E = (c_{Pp}/c_P)(3-\beta)/(2\beta)$ implying that when the particles are very light, the thermal coupling decreases and eventually becomes negligible in the bubble limit. The physical mechanisms underlying the behavior of the thermal coupling remain to be fully understood and will be the focus of the next chapter.

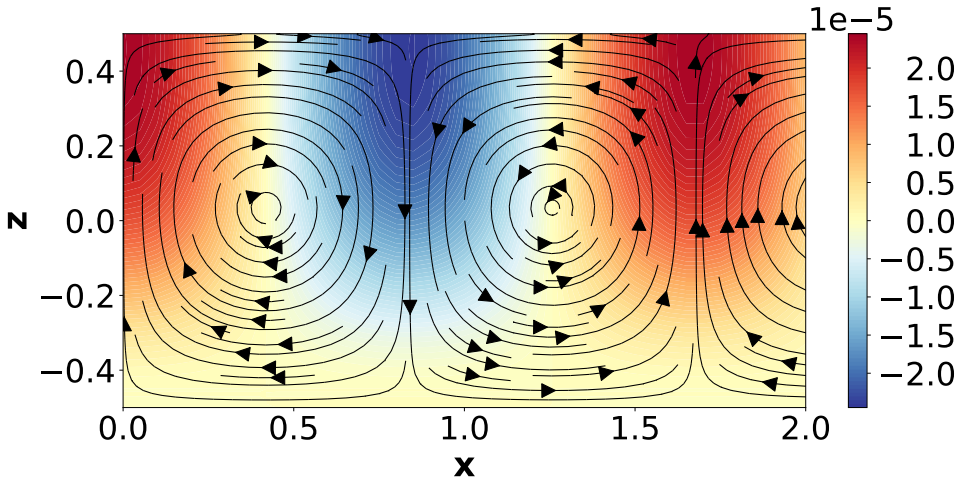

(d) $\beta = 3,\ W^*/W_T = 0.5$

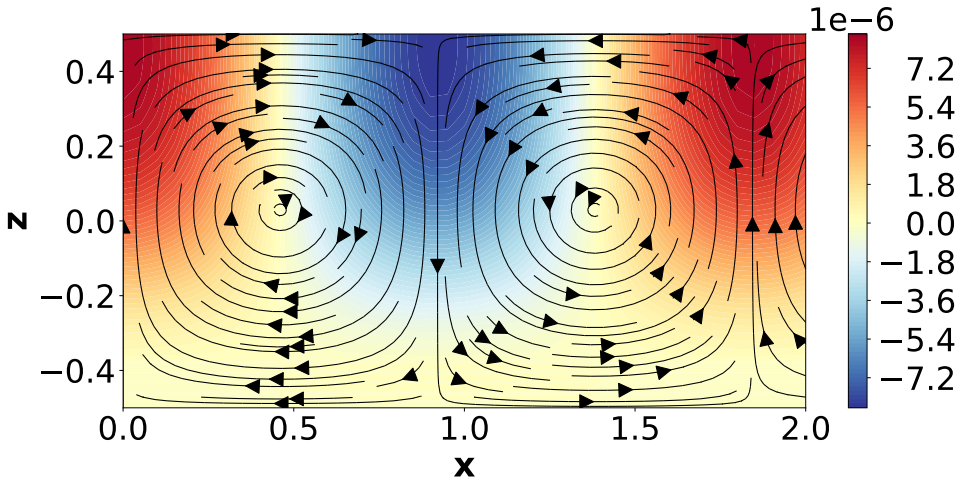

(e) $\beta = 3,\ W^*/W_T = 0.8$

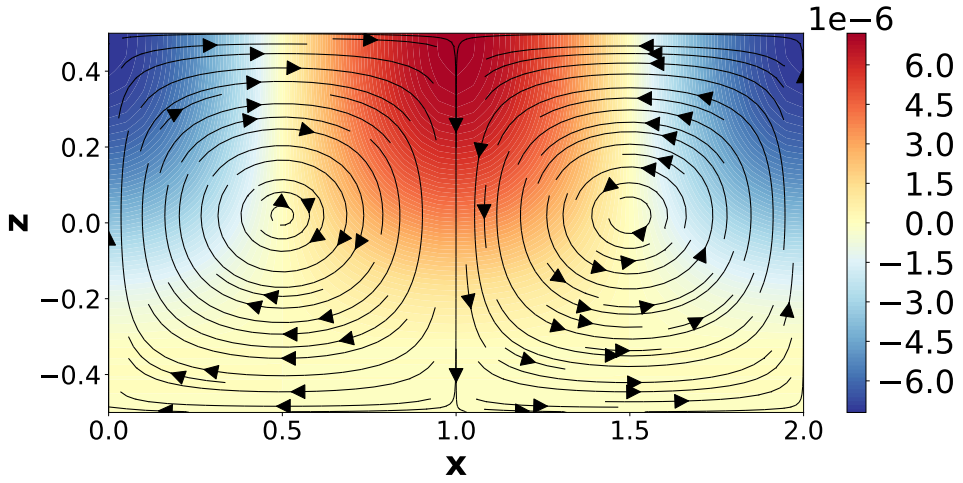

(f) $\beta = 3,\ W^*/W_T = 1.2$

Figure 6.5: Streamlines of fluid velocity field and colormap of the particle volume fraction at the onset of convection for $\beta = 3$ and increasing inlet velocities from top to bottom. For a better comparison, the particle volume fraction α' is normalized with respect to the base volume fraction α_0 for $\beta = 3$ and $W^* = W_T$ particles. The particle inlet flux is $\mathcal{J} = \mathcal{J}_0$

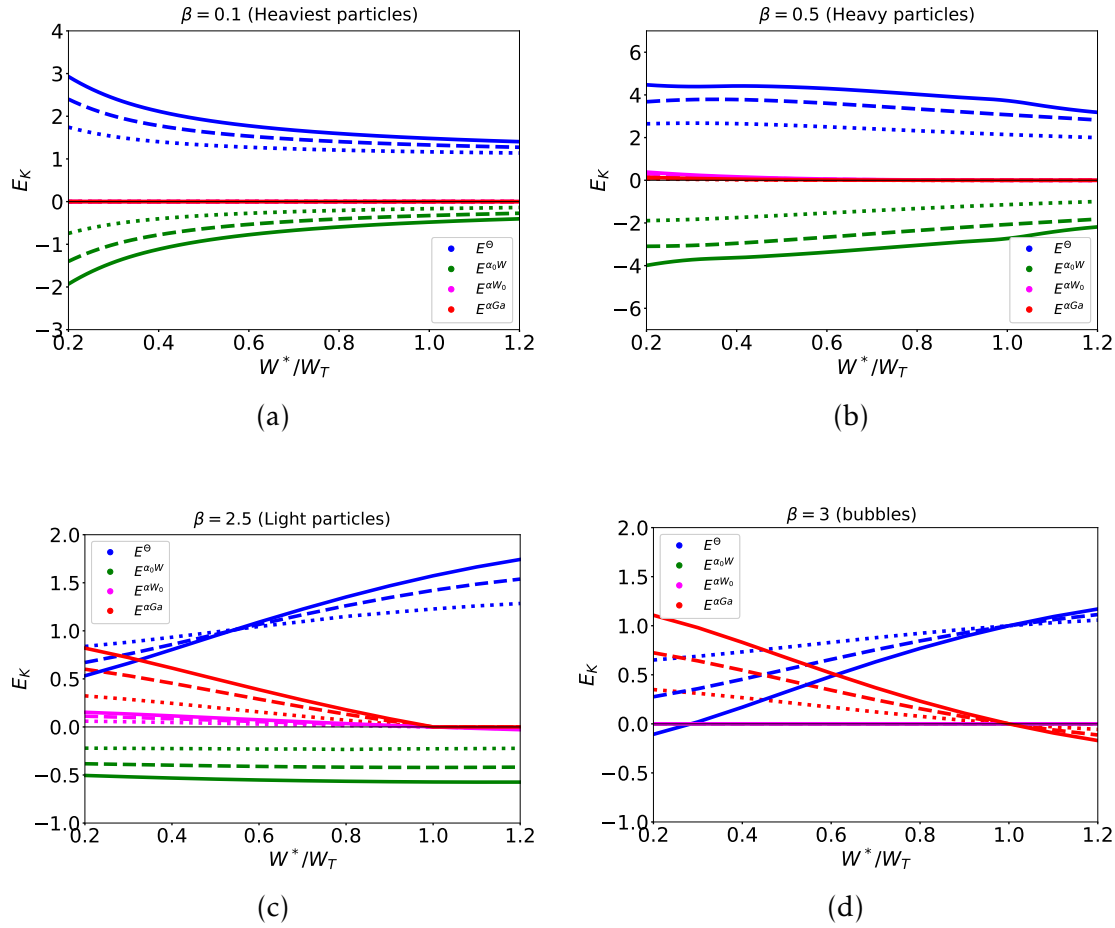

Figure 6.6: Components of the kinetic energy budget at the neutral stability condition versus the particle inlet velocity: thermal buoyancy injection power E^{Θ}, viscous dissipation rate E^{V}, particle feedback's due to the base particle concentration, base particle velocity and particle buoyancy $E^{\alpha_0 W}$, $E^{\alpha W_0}$,$E^{\alpha Ga}$. Results obtained for different particle inlet fluxes: $0.5\mathcal{J}_0$ (dotted lines), $\mathcal{J}_0$ (dashed lines), $1.5\mathcal{J}_0$ (solid lines).

Chapter 7

Particle Thermal Inertia Delays the Onset of Convection in Particulate Rayleigh–Bénard System

Outline of the current chapter

Chapter 6 analyzed the influence of particle injection velocity and inlet flux on the stability of the particulate Rayleigh–Bénard (pRB) system. In this chapter, we focus on the effect of thermal coupling between the particles and the fluid. In particular, we explore the convective onset when the thermal inertia of the particles or their injection temperature into the system is varied.

In previous chapters, thermal coupling between the particulate and fluid phases was described by particle to fluid volumetric heat capacity ratio denoted by the parameter E, defined as

$$E = \left(\frac{c_{Pp}}{c_P}\right)\frac{\rho_p}{\rho}.$$

This parameter was kept always constant and << 1. However, we can observe that it can be written as,

$$E = \left(\frac{c_{Pp}}{c_P}\right)\frac{3-\beta}{2\beta},$$

where

$$\beta = \frac{3\rho}{\rho + 2\rho_p},$$

is the fluid to particle modified density ratio. As expressed above, E combines two independent physical contributions: the specific heat capacity ratio:

$$\epsilon = \frac{c_{Pp}}{c_P},$$

and the modified mass density β. In this chapter we therefore reformulate the problem in terms of ϵ, which allows us to separate the influence of thermal properties from that of the mass density. This separation also makes clear that in the limit $\rho_p \to 0$, i.e. bubbles in water with $\rho_p/\rho \approx 10^{-3}$, the thermal coupling becomes negligible despite finite heat capacity, whereas for particles comparable or denser than the fluid, thermal exchanges remain important.

This chapter is organized as follows. Section 7.1 presents the results and discussion, focusing on the influence of key physical parameters on the stability characteristics of the particle-laden Rayleigh–Bénard (pRB) system. Specifically, Subsections 7.1.1 to 7.1.5 address the effects of the specific heat capacity ratio (ϵ), injection temperature, mass density, injection velocity and inlet flux, and particle concentration at the onset, respectively. Section 7.2 provides an analysis of the energy budget to elucidate the mechanisms governing flow stability. Finally, Section 7.3 summarizes the main findings and concluding remarks of this chapter.

7.1 Results and discussion

In this study, some of the parameters that characterize the system are kept constant. These are: $Pr = 5$, $Ga = 9.8 \times 10^9$, $\Phi = 10^{-2}$. The critical Rayleigh number Ra_c is used

as the primary control parameter in our stability analysis. The parameters varied throughout the study are: β, ϵ, Θ_p^* and $\mathcal{J}$ and, $\mathbf{W}^*$, where $\mathbf{W}_T$ is the particle terminal velocity in the still fluid, that reads $\mathbf{W}_T = ((1-\beta)/\beta)((\Phi^2)/12)\, Ga\, Pr\, \hat{\mathbf{z}}$. Unless otherwise specified, the particle flux is set to $\mathcal{J}_0 = 533.3$, $\mathbf{W}^* = 0.5\mathbf{W}_T$, and the particle injection temperature Θ_p^* is assumed to match the temperature of the wall from which they are introduced — i.e., warm for light particles (injected from below) and cold for heavy particles (injected from above).

7.1.1 Influence of the specific heat capacity ratio

Figure 7.1 shows the dependence of the critical Rayleigh number Ra_c on the specific heat capacity ratio ϵ for representative values of β corresponding to heavy and light particles. The parameter ϵ quantifies the efficiency of heat exchange between particles and fluid, thereby controlling the strength of thermal coupling. For small ϵ, the particle heat capacity is negligible compared to that of the fluid, and the particles rapidly equilibrate with the surrounding temperature field. In contrast, for large ϵ, particles act as distributed heat sources or sinks, influencing the local thermal field while maintaining their own temperature. The mechanical coupling between the two phases remains unaffected, as it is independent of ϵ. This separation of mechanical and thermal effects distinguishes the present parametrization from earlier pRB studies.

The results in Figure 7.1 show that stronger thermal coupling systematically increases system stability, as reflected by higher Ra_c values for both heavy and light particles. The stabilizing trend persists until a saturation point, beyond which further increases in ϵ no longer affect the critical thresholds. This saturation behavior is also observed in the critical wavenumber k_c. In case of extreme specific heat capacity ratio ($\epsilon \to \infty$) the temperature of the particulate phase does not change and also in this case particle energy equation can be discarded. We have to reconstruct the base state which follows from equations (2.44) and (2.45) as,

$$D^2\Theta_0 - \frac{12\alpha_0}{\Phi^2}(\Theta_0 - \Theta_p^*) = 0 \tag{7.1}$$

Finally, the stabilizing effect is not monotonic with β for the three representative cases shown in Figure 7.1; this dependence is further discussed in Section 7.1.3.

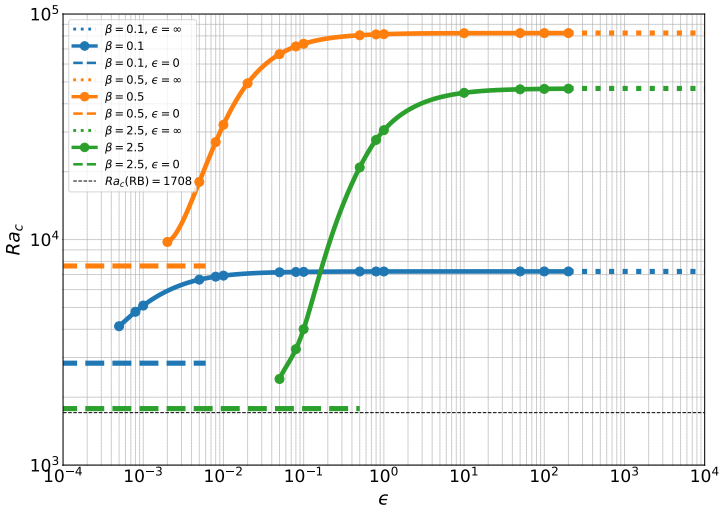

(a)

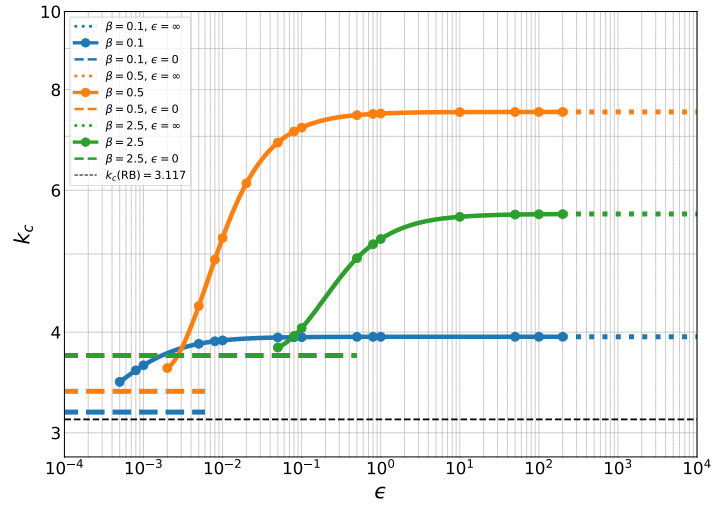

(b)

Figure 7.1: Effect of thermal coupling on the critical stability thresholds of the particulate Rayleigh-Bénard (pRB) system for heavy and light particles. Panel (a) shows the critical Rayleigh number Ra_c, while panel (b) presents the critical wavenumber k_c. The horizontal dashed colored lines correspond to the limiting case $\epsilon = 0$, which represents purely mechanical coupling without any thermal effects, while the dotted horizontal lines represents the limiting case $\epsilon \to \infty$, where the instability reaches a clear plateau. The black dashed line indicates the reference Rayleigh–Bénard threshold for a single-phase system $Ra_c = 1708$.

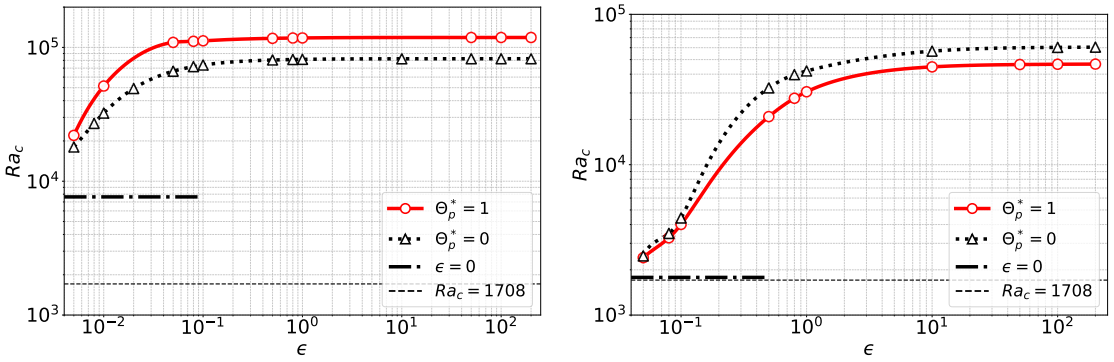

(a) $\beta = 0.5$ (Heavy particles) (b) $\beta = 2.5$ (Light particles)

Figure 7.2: Effect of particle injection temperature on the critical threshold. (a) Heavy particles ($\beta = 0.5$) are injected from above with the cold wall temperature $\Theta_p^* = 0$, and inversely with the temperature of the opposite hot wall, $\Theta_p^* = 1$. (b) Light particles ($\beta = 2.5$) are injected from below with the hot wall temperature $\Theta_p^* = 1$, and inversely with the opposite cold wall temperature $\Theta_p^* = 0$.

7.1.2 Impact of injection temperature

Figure 7.2 shows that the stabilizing effect of ϵ is independent of the particle injection temperature. This is evident from the similar trends of $Ra_c(\epsilon)$ for cases where particles enter the system with the temperature of the injection wall or with that of the opposite wall. Although the absolute Ra_c values differ between these cases, the stabilizing tendency with increasing ϵ remains unchanged for both heavy and light particles. As $\epsilon \to 0$, the influence of the injection temperature vanishes, and both curves converge to the critical Rayleigh number of the purely mechanically coupled system.

7.1.3 Influence of mass density

Figures 7.3 and 7.4 show the respective dependence of the critical Rayleigh and wavenumbers, Ra_c and k_c, on the density ratio parameter β for three different values of the specific heat capacity ratio ϵ. The horizontal dashed lines mark the corresponding reference Rayleigh–Bénard thresholds, $Ra_c = 1708$ and $k_c = 3.117$. Three distinct regimes can be identified.

On the left-hand side of both figures ($\beta < 1$), corresponding to particles denser than the fluid, the three curves nearly collapse onto one another, indicating that thermal coupling has little influence in this regime. Even in the extremely heavy particle

limit ($\beta \to 0$), where particles behave as distributed constant-temperature sources, as suggested by Equations (2.38) and (2.39), the stability is dominated by mechanical coupling. For $\beta = 0$ (the ballistic limit), particles retain a constant temperature and accelerate uniformly, resulting in an infinite terminal velocity. Since the particle flux is held constant in our analysis, this effectively means no particles are injected. In this limit, the system thus reduces to the classical single-phase Rayleigh–Bénard problem, with a convective onset at $Ra_c \simeq 1708$.

As the particle density approaches that of the carrier ($\beta \to 1$), the system becomes increasingly stable, i.e. Ra_c rises sharply, and the dominant disturbances become smaller, i.e. k_c increases. The limit $\beta \to 1$ is singular in the present model: maintaining a constant inlet particulate flux would require a particle concentration exceeding the dilute limit, leading to nonphysical or divergent solutions. This likely explains why the two numerical methods no longer yield consistent results near $\beta \sim 1$, marked as the gray-shaded region in both figures. Only data points for which consistent results were obtained across all methods are shown.

In the light-particle regime ($\beta > 1$), distinct trends emerge. As β increases beyond unity, the three curves separate, showing that the influence of the specific heat capacity ratio ϵ becomes significant. Consistent with previous results, larger ϵ values, i.e. stronger particle heat capacity relative to the fluid—lead to higher critical Rayleigh and wavenumbers, indicating increased stability and smaller dominant structures, respectively. When β is sufficiently large, however, all curves shift downward. For instance, when $\epsilon = 0.1$, Ra_c falls below the single-phase Rayleigh–Bénard threshold. Varying β therefore modifies both mechanical and thermal coupling effects. This dual influence can be seen directly in Equation (2.39), where the limit $\beta \to 3$ is equivalent to $\epsilon \to 0$. For $\beta = 3$, conventionally referred to as the "bubble" case, the thermal coupling vanishes.

7.1.4 Impact of injection velocity and inlet flux

The trend discussed above, namely the stabilization observed with increasing particle thermal inertia, persists when the particle injection velocity $\mathbf{W}^*$ and volumetric particle flux $\mathcal{J}$ are varied, as illustrated in Figures 7.5a and 7.6a.

For heavy particles (Fig. 7.5a), the changes in $\mathcal{J}$ and $\mathbf{W}^*$ do not lead to qualitative differences between low and high thermal coupling regimes (corresponding respectively to $\epsilon = 5 \times 10^{-3}$ and $\epsilon = 200$). However, when the inlet particle flux is increased, the influence of ϵ becomes strongly amplified, that is, changing $\mathcal{J}$ by 50% nearly double the

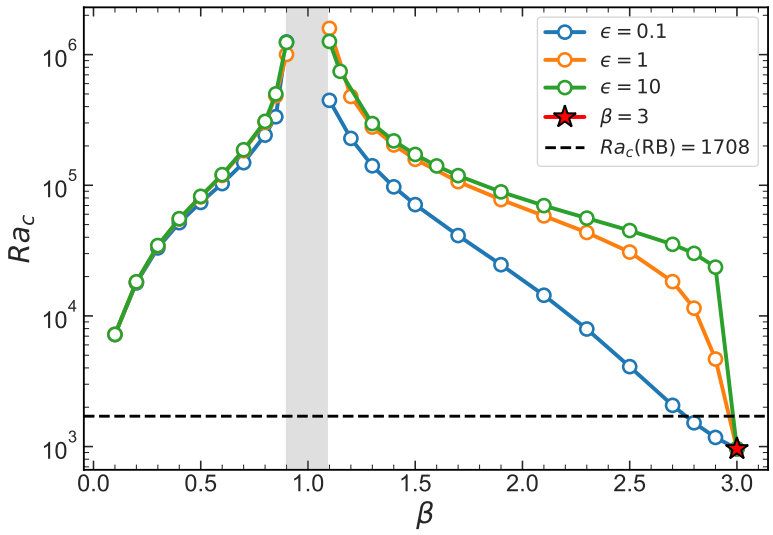

Figure 7.3: Critical Rayleigh number Ra_c as a function of the density ratio parameter β, for three values of the particle-to-fluid specific heat capacity ratio ϵ. The left branch corresponds to particles denser than the fluid, while the right branch corresponds to lighter particles. The horizontal dashed line indicates the reference Rayleigh–Bénard threshold ($Ra_c = 1708$).

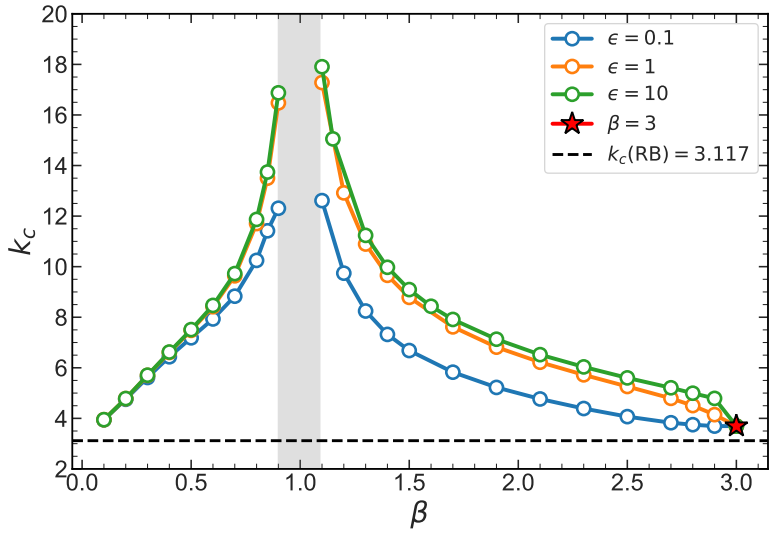

Figure 7.4: Critical wavenumber k_c as a function of the density ratio parameter β, for three values of the particle-to-fluid specific heat capacity ratio ϵ. The horizontal dashed line indicates the reference Rayleigh–Bénard value ($k_c = 3.117$).

Table 7.1: Numerical results for Ra_c and k_c for a selected subset of particle classes with β and ϵ values, corresponding to results in Figure (7.3). We compare results from Shooting method (SM) and Matrix-Forming methods (MFM). The case $\beta = 3$ is independent of the ϵ value, i.e., it corresponds to the case of no thermal coupling.

ϵ	β	Ra_c (SM)	k_c (SM)	Ra_c (MFM)	k_c (MFM)
6*0.1	0.1	7.1900×10^3	3.9431	7.1906×10^3	3.9430
	0.5	7.3801×10^4	7.1761	7.3875×10^4	7.1856
	0.8	2.4175×10^5	10.2235	2.4027×10^5	10.2477
	2.5	4.0072×10^3	4.0464	4.0905×10^3	4.0687
	2.7	2.0326×10^3	3.8158	2.0679×10^3	3.8267
	2.8	1.5002×10^3	3.7425	1.5204×10^3	3.7493
6*1.0	0.1	7.2184×10^3	3.9469	7.2189×10^3	3.9468
	0.5	8.1409×10^4	7.4711	8.1479×10^4	7.4799
	0.8	3.0225×10^5	11.6887	3.0249×10^5	11.7043
	2.5	3.0544×10^4	5.2199	3.0827×10^4	5.2603
	2.7	1.8142×10^4	4.7702	1.8306×10^4	4.7913
	2.8	1.1465×10^4	4.5051	1.1465×10^4	4.5050
6*10	0.1	7.2645×10^3	3.9477	7.2208×10^3	3.9470
	0.5	8.2220×10^4	7.5019	8.2291×10^4	7.5106
	0.8	3.0814×10^5	11.8536	3.0836×10^5	11.8685
	2.5	4.4727×10^4	5.5611	4.5033×10^4	5.6012
	2.7	3.5091×10^4	5.1823	3.5318×10^4	5.2096
	2.8	3.0113×10^4	4.9950	3.0113×10^4	4.9950
$\forall \epsilon \in [0, \infty)$	3.0	9.6150×10^2	3.6948	9.6621×10^2	3.7146

value of Ra_c

Similar to heavy particles, for light particles the increment of thermal coupling also leads to stabilization, with stronger stability achieved as the specific heat capacity ratio ϵ increases. The stabilization effect of ϵ is strongly enhanced by increasing the inlet flux of particles. Also, contrarily to the heavy particles case, increasing, inlet velocity promotes stabilization. Our results suggest that higher fluxes and larger specific heat

capacity ratios strengthen stability for both heavy and light particles.

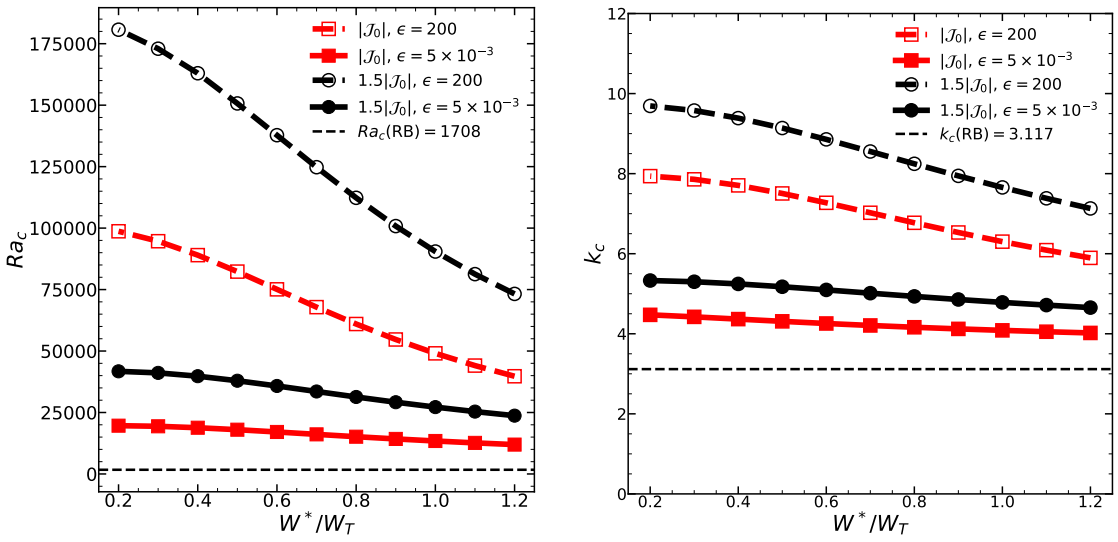

(a) (b)

Figure 7.5: (a) Critical Rayleigh number (Ra_c) and (b) critical wavenumber (k_c) as functions of inlet velocity, showing the onset of instability for $\beta = 0.5$ (heavy particles) under different thermal coupling strengths and particulate flux conditions.

7.1.5 Flow patterns and particle concentrations at the convective onset

The linear stability analysis enables the visualization of fluid and particle patterns at the onset of natural convection. These fields are representative of the physical system as long as disturbance amplitudes remain small, such that the linear approximation holds, i.e. before nonlinear saturation mechanisms become significant. Despite this limitation, the analysis provides valuable insight into the linear interaction between fluid and particle patterns. In addition, it allows examination of whether a nonuniform spatial distribution of particles can develop at the onset of convection.

Within the framework of linearized dynamics, only particle injections with velocities differing from their terminal value can generate spatial inhomogeneities, as shown in [172]. Figures 7.7 present visualizations of the velocity and temperature fields of both the fluid and dispersed phases, together with the particle concentration, at the onset of

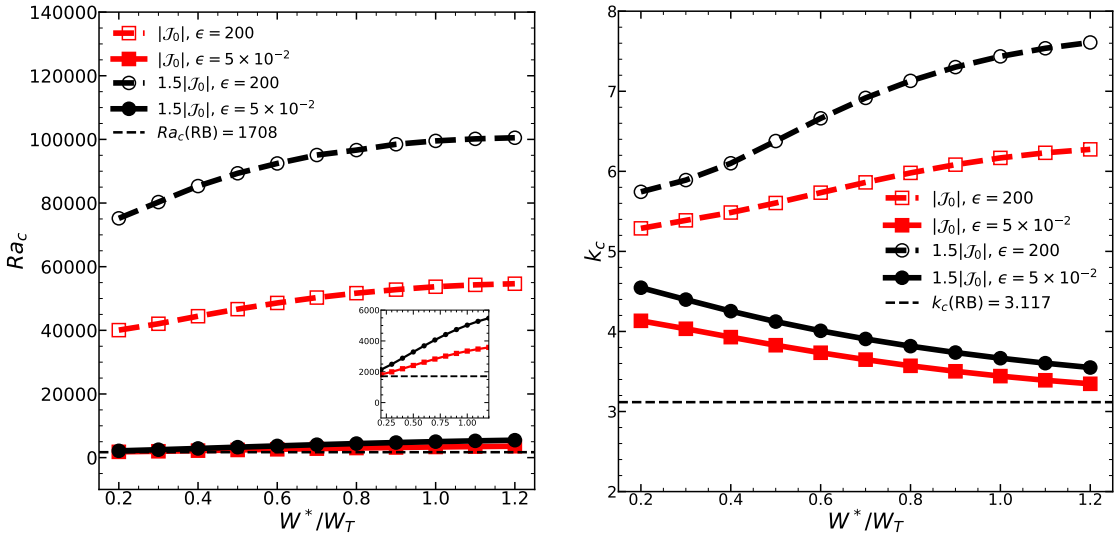

(a) (b)

Figure 7.6: (a) Critical Rayleigh number (Ra_c) and (b) critical wavenumber (k_c) as functions of inlet velocity, showing the onset of instability for $\beta = 2.5$ (light particles) under different thermal coupling strengths and particulate flux conditions.

convection for heavy particles ($\beta = 0.5$). Only disturbance fields are displayed; base-state contributions are omitted.

When particle thermal inertia is high, the particle temperature does not relax to that of the surrounding fluid and therefore remains nearly constant. Regions where both the fluid and particles are colder—that is, exhibit negative temperature disturbances—correspond to zones of high particle concentration. This behavior is expected since initially cold particles are injected from above and dispersed near the lower wall due to downwelling plumes. Varying the parameter ϵ does not alter this trend. Another notable feature is the dependence of the dominant disturbance wavelength on particle inertia: larger inertia leads to smaller convection patterns. Similar behavior is observed for light particles ($\beta = 2.5$), shown in Figure 7.8, the only difference being that light particles accumulate near the upper wall in upwelling plumes [172].

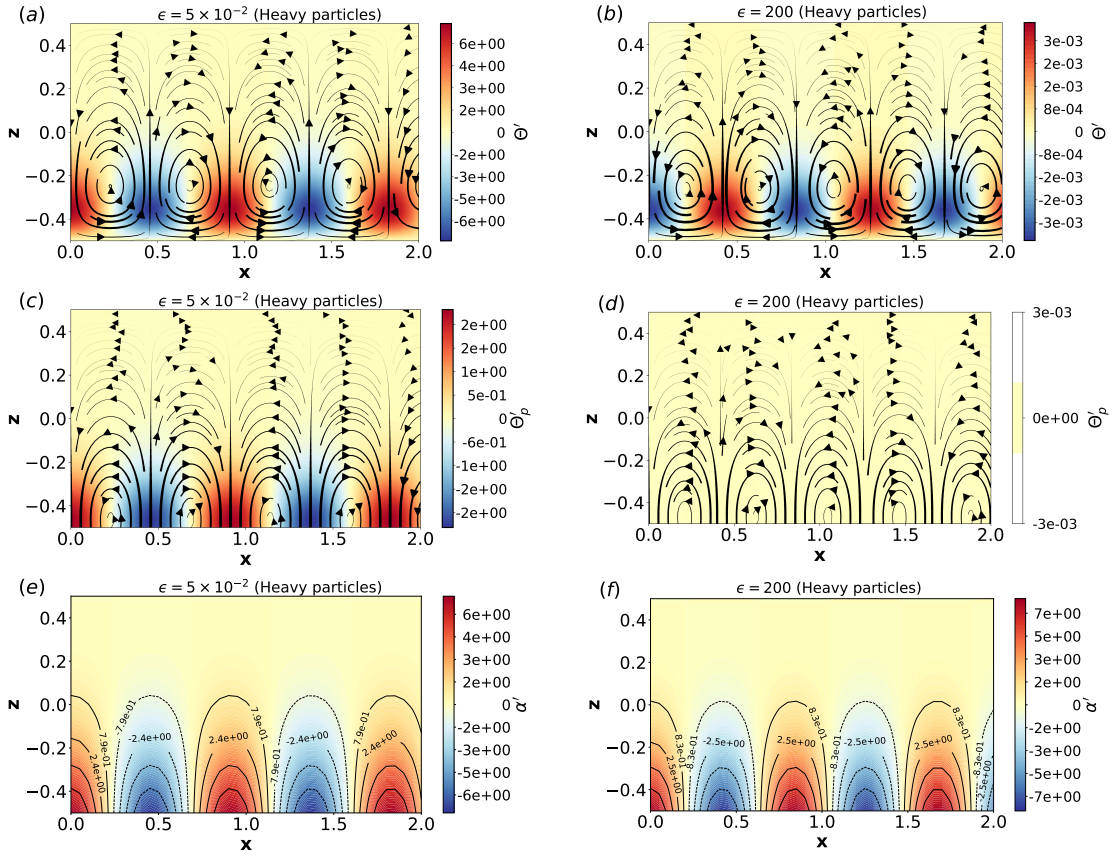

Figure 7.7: Field visualizations for $\beta = 0.5$ (heavy particles), $\mathcal{J} = \mathcal{J}_0$ and $W^* = 0.5W_T$: (a-b) Streamlines of the fluid velocity overlaid on the fluid temperature field Θ' (in colors). (c-d) Streamlines of the particle velocity field overlaid on the particle temperature field Θ'_p (in colors). (e-f) Contour lines and heatmap for concentration of the particle.

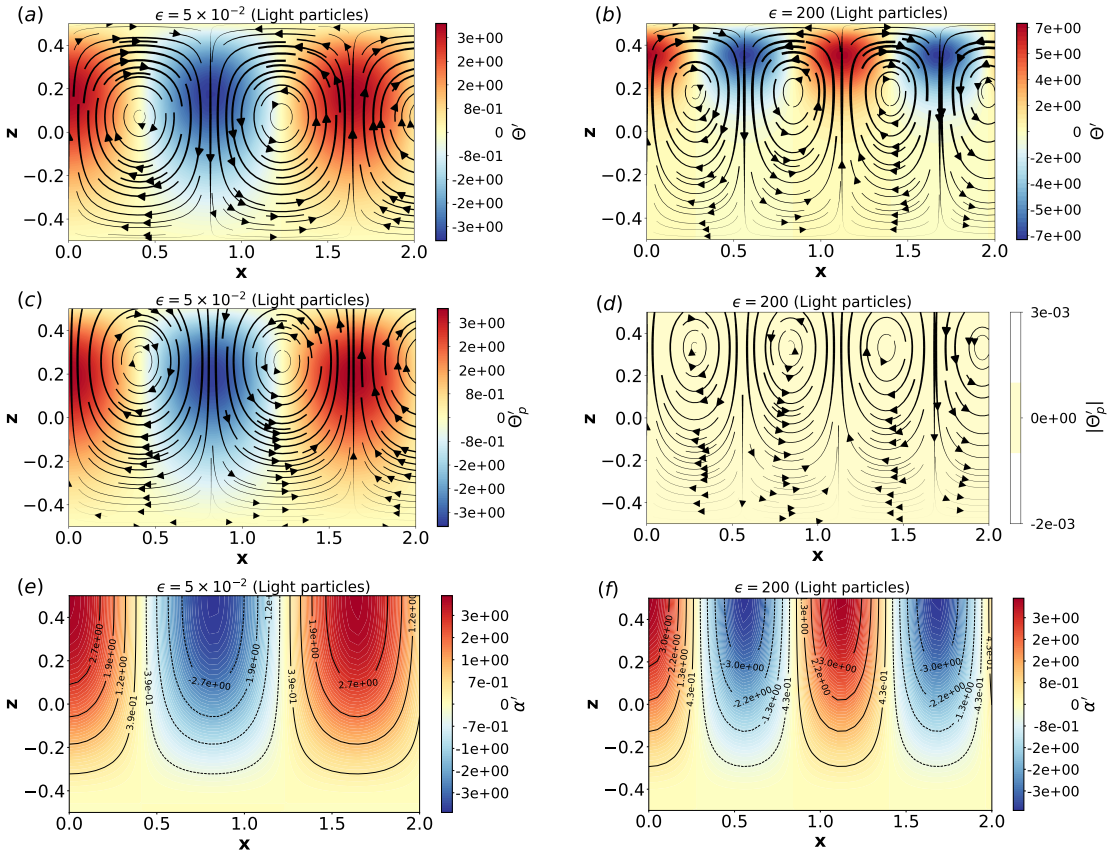

Figure 7.8: Field visualizations for $\beta = 2.5$ (light particles), $\mathcal{J} = \mathcal{J}_0$ and $W^* = 0.5W_T$: (a-b) Streamlines of the fluid velocity overlaid on the fluid temperature field Θ (in colors). (c-d) Streamlines of the particle velocity field overlaid on the particle temperature field Θ'_p (in colors). (e-f) Contour lines and heatmap for concentration of the particle.

7.2 Energy budget analysis

An *a posteriori* analysis of the energy transferred between the base state and the critical mode is here employed to identify the physical mechanisms leading to flow instability and to validate the overall energy conservation of our neutral mode. To that end, we employ a methodology similar to the one presented in [146], and numerically evaluate all terms in the spatially averaged linearized energy and momentum conservation equations.

From equation (3.32), the following relationship for the spatially averaged disturbance thermal energy e_Θ is obtained

$$\lambda e_\Theta = e_\Theta^{th} + e_\Theta^{diff} + e_\Theta^{fp} + e_\Theta^{fp\alpha}$$

with

$$e_\Theta = \int_{-1/2}^{1/2} (1-\alpha_0)\mathrm{Re}\left[(\Theta^n)\bar{\Theta}^n\right] - \Theta_0\mathrm{Re}\left[(\alpha^n)\bar{\Theta}^n\right] dz, \tag{7.2}$$

$$e_\Theta^{th} = \int_{-1/2}^{1/2} (\alpha_0 - 1)D\Theta_0\mathrm{Re}\left[(U_z^n)\bar{\Theta}^n\right] dz, \tag{7.3}$$

$$e_\Theta^{diff} = \int_{-1/2}^{1/2} \mathrm{Re}\left[(D^2 - k^2)(\Theta^n)\bar{\Theta}^n\right] dz, \tag{7.4}$$

$$e_\Theta^{fp} = -\frac{12}{\Phi^2}\int_{-1/2}^{1/2} \alpha_0\mathrm{Re}\left[(\Theta^n - \Theta_p^n)(\bar{\Theta}^n)\right] dz, \tag{7.5}$$

$$e_\Theta^{fp\alpha} = -\frac{12}{\Phi^2}\int_{-1/2}^{1/2} (\Theta_0 - \Theta_{p0})\mathrm{Re}\left[(\alpha^n)\bar{\Theta}^n\right] \tag{7.6}$$

where overbars denote the complex conjugate, e_Θ^{th} is the energy due to thermal advection, e_Θ^{diff} corresponds to the thermal dissipation energy. The energy exchange between particles and fluid as a result of drag forces is represented by e_Θ^{fp}. It quantifies transfers of energy between particles and the surrounding fluid. The sign of the integrands determines whether the local energy transfer acts as a destabilizing (positive) or a stabilizing (negative) contribution. If the rate of change of the total energy e_Θ is positive, the basic flow is unstable, and vice-versa. Hence, the energy budget can also be used to verify the linear stability results since the rate of change of the total energy must vanish for the neutral modes. In our computations, such a condition is verified at the fifth digit. By normalizing the different contributions by the absolute value of the dissipation

energy, we obtain at neutral conditions ($\lambda = 0$) :

$$E_\Theta^{th} + E_\Theta^{fp} + E_\Theta^{fp\alpha} = 1, \tag{7.7}$$

where $E_\Theta^{th} = e_\Theta^{th}/|e_\Theta^{diff}|$, $E_\Theta^{fp} = e_\Theta^{fp}/|e_\Theta^{diff}|$ and $E_\Theta^{fp\alpha} = e_\Theta^{fp\alpha}/|e_\Theta^{diff}|$.

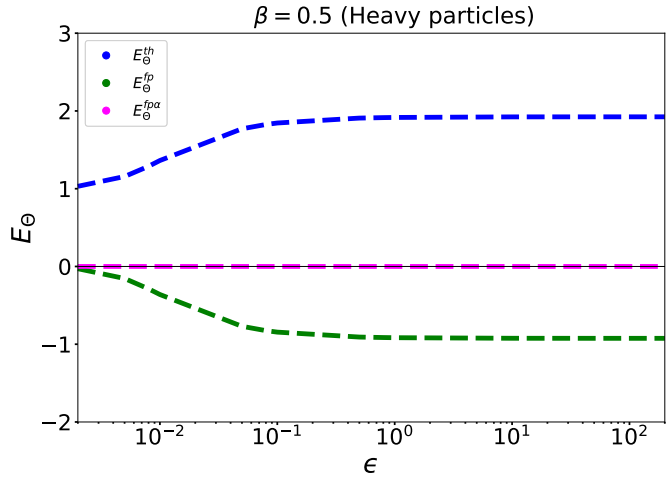

Figure 7.9: Thermal energy budget for the case of heavy particles.

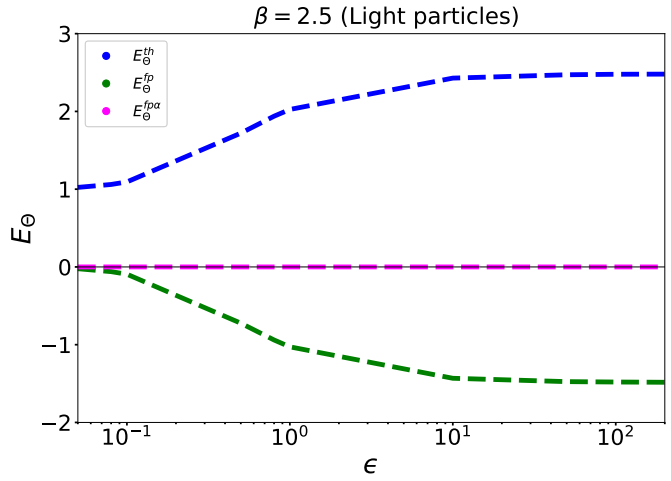

Figure 7.10: Thermal energy budget for the case of light particles.

7.3 Conclusion

A linear stability analysis of particulate Rayleigh–Bénard convection was conducted to quantify the influence of particle thermal inertia, density ratio, and injection conditions on the onset of convection. The study combined the coupled momentum and energy equations for the fluid and dispersed phases to determine how each parameter modifies the critical Rayleigh number and wavenumber. Particle thermal inertia, represented by the specific heat capacity ratio ϵ, has a stabilizing effect on the system. Increasing ϵ homogenizes the temperature field, weakens buoyancy-driven motion, and raises both the critical Rayleigh number and the dominant wavenumber, indicating smaller convection cells. This stabilizing trend is independent of the particle injection temperature and roughly saturates beyond $\epsilon = \mathcal{O}(1)$. The density ratio β exerts an asymmetric influence: both heavy ($\beta < 1$) and light ($\beta > 1$) particles stabilize the system relative to the single-phase case, but the effect is stronger for heavy particles. For $\beta \to 1$, the model reaches a singular limit where maintaining a constant particle flux would violate the dilute suspension assumption. For large β, the system approaches the "bubble" limit ($\beta = 3$), where thermal coupling vanishes. In such case the system may become even more unstable that the classical single phase RB system. Variations in the inlet particle velocity $\mathbf{W}^*$ and volumetric flux $\mathcal{J}$ modulate the stabilizing effect of ϵ. Higher fluxes enhance the influence of particle thermal inertia for both heavy and light particles. However, increasing $\mathbf{W}^*$ promotes stability in the light-particle regime but not in the heavy-particle one.

These findings clarify the distinct roles of particle thermal and mechanical couplings in the stability of particulate Rayleigh–Bénard systems. They provide a quantitative foundation for future nonlinear analysis either theoretical or numerical and experimental studies.

Conclusions & Perspectives

In this thesis, we advanced the theoretical understanding of particulate Rayleigh–Bénard convection by conducting a systematic study that aimed to extensively explore the parameters of the problem, from the material properties of the particles to those of their mode of introduction into the system. We begin with a review of different strategies for describing dispersed multiphase flows, including Eulerian, Lagrangian, and fully resolved approaches, and discuss their respective advantages and limitations. Next, we derive the governing equations for the particulate phase in detail, covering the mass, momentum, and energy balances. Building on this foundation, we formulate the two-fluid Eulerian description of dispersed two-phase flows, which couples the particulate and fluid phases through conservation laws for mass, momentum, and energy. With this general formulation in place, we derive the particulate Rayleigh–Bénard model system in its dimensional form, and subsequently introduce the corresponding dimensionless equations, separating fluid and particle contributions and identifying the key parameters that control mechanical and thermal coupling.

In part II, we shed the light on the methodology used to analyze this model system. We begin with the theoretical framework for linear stability analysis (Chapter 3), first introducing the general formalism and then applying it to the particulate Rayleigh–Bénard system. We examine the base state and analyze how variations in the key control parameters of the model influence it and how the onset of instability is further affected. We then extend the analysis to the special case where particles are injected at their terminal velocity, highlighting the dynamics of this simplified model system. Finally, (Chapter 4) we discussed in detail the numerical methods used to solve the generalized eigenvalue problems arising from the stability analysis. Rather than relying on a single approach, we adopted a complementary strategy that combines the strengths of different methods. The Galerkin method was first employed to provide accurate initial guesses, which were then refined using the shooting method. All final results were obtained

with the shooting method, chosen for its accuracy and robustness in capturing stability thresholds. In addition, a matrix-forming approach was applied in selected cases to cross-check the results, thereby reinforcing the reliability of the conclusions presented in this thesis.

In Part III, we presented the results of this study, structured into three chapters. The first major contribution of this work (Chapter 5) is the theoretical demonstration that when particles are injected at their terminal Stokes velocity, they invariably stabilize the system with respect to classical Rayleigh–Bénard or in other words, particles aid in delaying the onset of convection, regardless of whether they are heavier or lighter than the fluid, including the limiting case of bubbles. The linear stability analysis revealed that the critical Rayleigh number is systematically increased, with stabilization effect reaching up to a factor of 30 for the lightest particles and 60 for the heaviest ones at a particulate volume fraction of 0.1%. The analysis of the thermal and kinetic energy budgets clarified the respective roles of thermal and mechanical couplings in this stabilizing effect. These results extend the earlier work of Prakhar and Prosperetti [50]- where stabilization was demonstrated only for very heavy particles - by incorporating the added-mass force and thereby covering the full range of particle densities.

To overcome the limitations of earlier studies, In (Chapter 6) we introduced arbitrary particle injection velocities in the particulate Rayleigh–Bénard system. This extension made it possible to account for particle accumulation and revealed a richer set of mechanical coupling effects which are missing in previous studies. The analysis showed that in case of heavy particles, the increase in particle injection velocity promotes destabilization, while light particles progressively stabilize it as the injection velocity increases. In the bubble limit, sufficiently low injection velocities can even shift the onset of convection to negative Rayleigh numbers, corresponding to heating from above. Furthermore, particle accumulation zones were found to shift between upwelling and downwelling regions as the injection speed transitions from sub-terminal to super-terminal values. These findings demonstrate that injection velocity is a central control parameter governing both system stability and the spatial localization of particle accumulation. In developing this framework, two possible sets of inlet control parameters were considered for characterizing the particle–fluid mechanical coupling: (i) injection velocity and volumetric particle flux, or (ii) injection velocity and volumetric particle concentration. We adopted the first approach, since it is more amenable to experimental realization, where it is generally easier to prescribe and control the inlet flow rate than to maintain a fixed particle-phase surface concentration. This modeling

choice, combined with the introduction of arbitrary injection velocities, represents a key contribution of this work, providing a more realistic and experimentally relevant foundation for the theoretical study of particulate-laden convection.

Finally, In (Chapter 7) we investigated the role of thermal coupling, parameterized by the ratio of particulate to fluid heat capacities. For heavy particles, increasing thermal inertia consistently enhances stability across all injection regimes. On the other hand, for light particles the effect of thermal coupling also leads to stabilization, similar to heavy particles, with stronger stability achieved as the particle-to-fluid heat capacity ratio (e) increases. Thermal effects were also shown to influence the horizontal scale of convection patterns, highlighting their nontrivial role in shaping flow structures.

Together, these results provide a comprehensive framework for understanding the interplay of momentum and heat transfer in particulate-laden convection. They establish clear benchmarks for future theoretical, numerical, and experimental work, while also extending the frontier of stability analysis to regimes that had not previously been considered. Several avenues emerge naturally from this study.

Incorporating additional forces may further alter the onset of convection. Foe example by incorporating nonlinear drag forces which is an important factor that can strongly influence particle–flow coupling. Similarly, extending the model to nonspherical particles would be relevant, since particle settling and reorientation have been studied in other contexts [141, 173] but not in Rayleigh–Bénard systems. Examining these effects in convection could reveal new instability mechanisms.

Second, particle size effects only approximately represented in Eulerian models call for particle-resolved numerical simulations to capture nonlinear particle–fluid interactions and inter-particle collisions more faithfully. Parallel laboratory experiments with controlled injection conditions would be invaluable for validating theoretical predictions and refining numerical models. Moreover, Rayleigh–Bénard convection is not the only stratified flow of interest: related particle-laden dynamics could be explored in Rayleigh–Taylor instabilities, where a heavier layer overlies a lighter one, or in stratified shear flows such as Rayleigh–Bénard-Poiseuille (RBP) [174] and flows in channels [147]. The same modeling framework developed here can be adapted to these cases. Among the perspective studies, the recent work on heavy particles in Rayleigh–Bénard convection showed that two-way momentum coupling enhances settling at high particle volume fractions [41].

Finally, while the present work focused on the linear regime, extending the analysis to weakly and fully nonlinear dynamics is essential to assess the long-term impact

of particulate phases on convective heat and momentum transport. This can be pursued through weakly nonlinear stability analyses, as in [54], or via direct numerical simulations based on the approaches reviewed in Chapter 2.

Appendix A

Influence of lift force on the stability of bubbly Rayleigh-Bénard system

Outline of the current chapter

This appendix[1] contains additional results related to the influence of the lift force on the stability of the bubbly Rayleigh–Bénard system. While these results were not developed into a full chapter, they highlight important aspects of the lift-force effect and are included here for completeness. The findings presented may serve as a useful reference for future investigations.

A.1 Modal analysis

Following the linearized system of equations in Chapter 3, the modal analysis equations are extended by including the lift force.

$$\lambda\alpha^n = -\left(\alpha_0 DW_z^n + W_z^n D\alpha_0\right) - \alpha_0 ikW_x^n - \left(W_0 D\alpha^n + \alpha^n DW_0\right), \tag{A.1}$$

[1] This part of the research has been carried out in collaboration with Yan Zhang and Apolline which is kindly acknowledged.

$$\begin{aligned}\lambda(D^2-k^2)U_z^n &= Pr(D^2-k^2)^2U_z^n - PrRak^2\Theta^n + \frac{D\alpha_0(\beta-1)}{2}\lambda DU_z^n \\ &- \frac{6Pr(3-\beta)}{\Phi^2}\left(\alpha_0(D^2-k^2)U_z^n + \alpha_0k^2W_z^n + \alpha_0ikDW_x^n\right) \\ &- \frac{6Pr(3-\beta)}{\Phi^2}\left(D\alpha_0DU_z^n + D\alpha_0ikW_x^n\right) + \frac{\alpha_0(\beta-1)}{2}\lambda(D^2-k^2)U_z^n \\ &- \left(\frac{\beta-1}{2}GaPr^2 + 6Pr(3-\beta)\frac{W_0}{\Phi^2}\right)k^2\alpha^n \\ &+ \frac{3-\beta}{6}\left(W_0\alpha_0\left(ikD^2U_x^n + k^2DU_z^n\right)\right) \\ &+ \frac{3-\beta}{6}\left(\left(ikDU_x^n + k^2U_z^n\right)\left(\alpha_0DW_0 + W_0D\alpha_0\right)\right),\end{aligned} \tag{A.2}$$

$$\lambda {W_z}^n + W_0D{W_z}^n + {W_z}^n\frac{dW_0}{dz} = \beta\lambda U_z^n + 12Pr\beta\frac{({U_z}^n - {W_z}^n)}{\Phi^2}, \tag{A.3}$$

$$\lambda {W_x}^n + W_0(D{W_x}^n) = \beta\lambda U_x^n + \frac{12Pr\beta}{\Phi^2}\left(-\frac{DU_z^n}{ik} - {W_x}^n\right) + \frac{\beta W_0}{3}\left(-ikU_z^n - \frac{D^2U_z^n}{ik}\right), \tag{A.4}$$

$$(1-\alpha_0)\left[\lambda\Theta^n + U_z^nD\Theta_0\right] = \alpha^n\lambda\Theta_0 + (D^2-k^2)\Theta^n - 12\alpha_0\frac{(\Theta^n-\Theta_p^n)}{\Phi^2} - 12\alpha^n\frac{(\Theta_0-\Theta_{p0})}{\Phi^2}, \tag{A.5}$$

$$\lambda\Theta_p^n + W_0D\Theta_p^n + {W_z}^nD\Theta_{p0} = \frac{12}{E}\frac{\Theta^n-\Theta_p^n}{\Phi^2}, \tag{A.6}$$

where D represents the derivative with respect to Z.

The system of equations (A.1)-(A.6), subject to the same boundary conditions (3.34-3.35), is solved numerically using the shooting method.

A.2 Results and discussion

As shown in Figures A.1a and A.3a when the lift force is included, the stability of the system exhibits a strong dependence on the injection velocity relative to the terminal velocity. At relatively high injection speeds (greater than about $0.6W_T$), the critical Rayleigh number Ra_c is consistently higher than that of the classical single-phase Rayleigh–Bénard (RB) system across all studied injection fluxes. Physically, this indicates that at higher injection velocities the upward transport of bubbles enhances momentum exchange and mixing, thereby suppressing the onset of buoyancy-driven

thermal convection and stabilizing the system. Conversely, at lower injection speeds (less than about $0.6W_T$), the presence of bubbles reduces the effective stability: the critical Rayleigh number drops below the RB threshold, suggesting that weak bubble injection promotes earlier onset of convection.

Figures A.1b and A.3b illustrate the same variation in the absence of lift. For the bubble size considered in this study, comparison of the effects with and without lift shown in Figure A.2 reveals that the effect of the lift force on Ra_c is relatively weak, at least within the range of injection parameters explored. This is in contrast to the findings of [52], who reported that lift significantly stabilizes the flow in horizontal bubble-laden systems without heating. The apparent contradiction can be traced to the fundamental differences between the two systems. In [52], the model considered rising bubbles in an initially quiescent liquid, where the flow was driven solely by bubble-induced buoyancy. In that context, the lift force redistributed bubbles and modified the momentum transfer, thereby exerting a strong influence on stability.

By contrast, in our system two distinct buoyancy mechanisms are present. The thermal buoyancy term,

$$B_T = PrRa\Theta\hat{\mathbf{z}},$$

acts directly on the fluid, whereas the bubble-induced buoyancy appears as a feedback force from the dispersed phase, which in the limit $\beta = 3$ reads

$$B_B = \alpha GaPr.$$

The imposed vertical temperature gradient therefore generates a more complex flow field, in which the contribution of lift becomes comparatively less dominant. Even under the weak thermal coupling considered here, thermal buoyancy introduces an additional mode of instability that reduces the relative importance of lift. This fundamental distinction explains the divergence between the present results and those of [52]. Figure A.4 presents the variation of the critical wavenumber k_c with different injection velocities. The upper set of curves corresponds to the situation without lift force, while the lower set of curves corresponds to the case with lift force. For all velocities considered, the inclusion of lift leads to systematically smaller values of k_c.

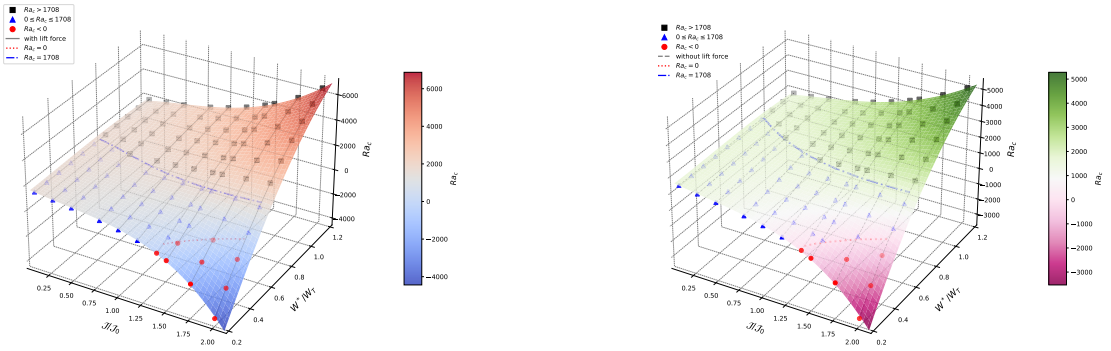

(a) with lift force (b) without lift force

Figure A.1: Variation of the critical Rayleigh number Ra_c with inlet flux $\mathcal{J}/\mathcal{J}_0$and inlet velocity W^*/W_T (a) with lift effect (b) without lift force. At high injection velocities, Ra_c exceeds the classical Rayleigh–Bénard threshold, indicating enhanced system stability.

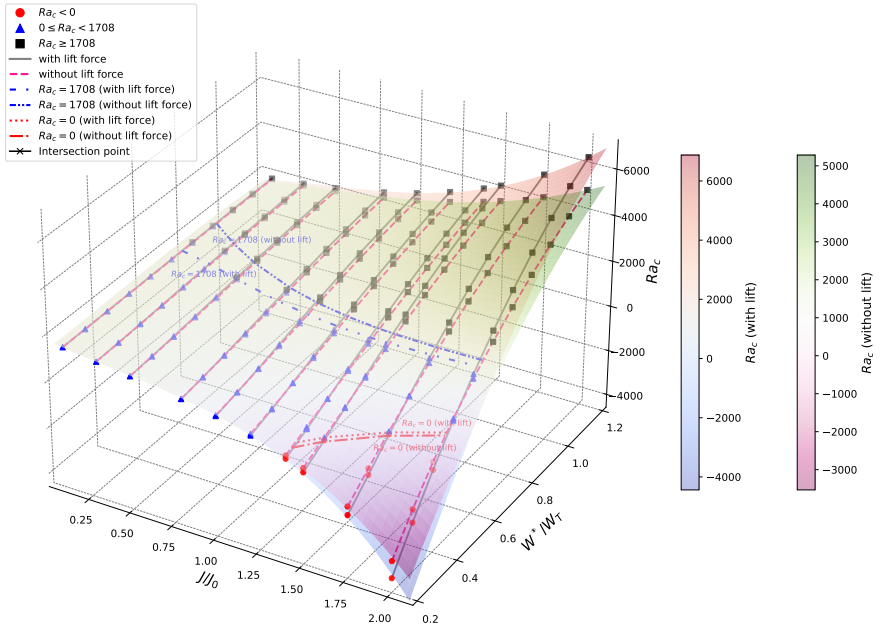

Figure A.2: Comparison of the critical Rayleigh number surface Ra_c as a function of inlet flux $\mathcal{J}/\mathcal{J}_0$ injection velocity (W^*/W_T), with and without lift force effects. The colored surfaces represent polynomial fits to the data, while scatter points mark the original values classified by stability regimes. Intersection curves at $Ra_c = 0$ and $Ra_c = 1708$ highlight the transition boundaries, illustrating how the lift force modifies convective onset conditions.

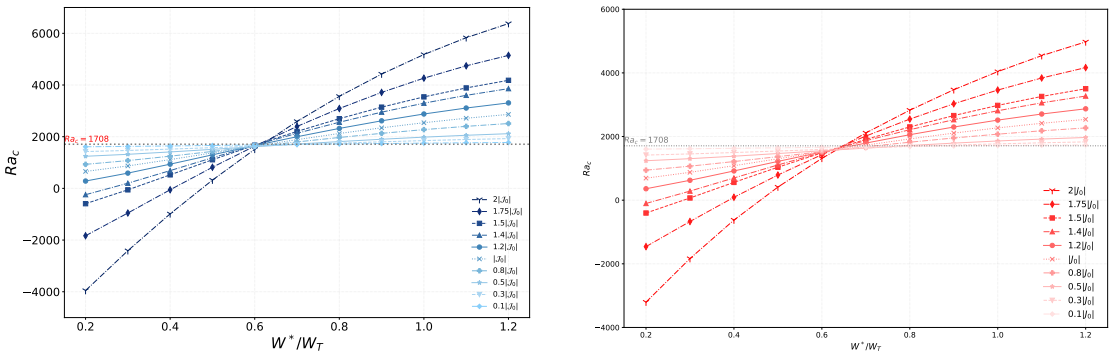

(a) with lift force (b) without lift force

Figure A.3: Critical Rayleigh number as a function of the inlet velocity for different particle fluxes. The horizontal dashed lines correspond to the single-phase RB threshold.

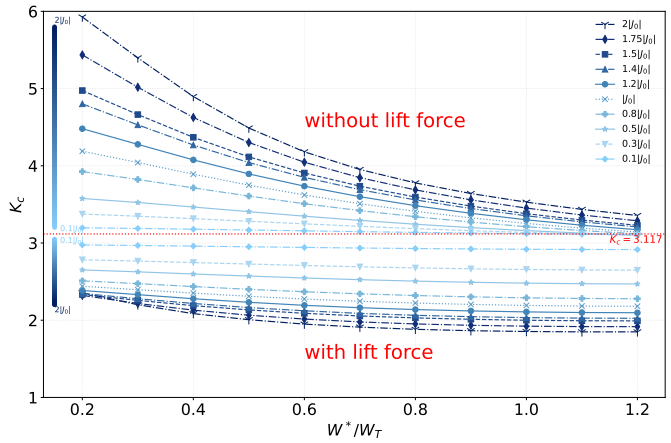

Figure A.4: Critical wave number as a function of inlet velocity for different particle fluxes, with and without the lift force. The horizontal dashed line denotes the single-phase Rayleigh–Bénard threshold.

Bibliography

[1] A. V. Getling. *Rayleigh-Bénard Convection: Structures and Dynamics*. Vol. 11. World Scientific, 1998. DOI: 10.1142/3097.

[2] P.G. Drazin and W.H. Reid. *Hydrodynamic Stability*. Cambridge University Press, 2004.

[3] S. Chandrasekhar. *Hydrodynamic and Hydromagnetic Stability*. Oxford University Press, 1961.

[4] G. Schubert, D.L. Turcotte, and P. Olson. *Mantle Convection in the Earth and Planets*. Cambridge University Press, 2001.

[5] J.M. Aurnou, E.M. King, and M.H. Heimpel. "Turbulent rotating convection controls the large-scale circulation of the Earth's mantle". In: *Nature* 517.7536 (2015), pp. 528–531.

[6] K.L. Chan and S. Sofia. "Astrophysical convection". In: *Annual Review of Astronomy and Astrophysics* 39 (2001), pp. 441–489.

[7] S. Kakaç, Y. Yener, and A. Pramuanjaroenkij. *Convective Heat Transfer*. CRC Press, 2009.

[8] D.A. Nield and A. Bejan. *Convection in Porous Media*. Springer, 2013.

[9] Lord Rayleigh. "On convection currents in a horizontal layer of fluid, when the higher temperature is on the under side". In: *Philosophical Magazine* 32.192 (1916), pp. 529–546.

[10] G. I. Taylor. "Stability of a viscous liquid contained between two rotating cylinders". In: *Philosophical Transactions of the Royal Society of London. Series A* 223 (1923), pp. 289–343.

[11] E. Hopf. "Abzweigung einer periodischen Lösung von einer stationären Lösung eines Differentialsystems". In: *Berichte der Mathematisch-Physikalischen Klasse der Sächsischen Akademie der Wissenschaften zu Leipzig* 94 (1942), pp. 1–22.

[12] E. N. Lorenz. "Deterministic nonperiodic flow". In: *Journal of the Atmospheric Sciences* 20.2 (1963), pp. 130–141.

[13] Stephan-Marian Piatkowski. “A spectral discontinuous Galerkin method for incompressible flow with applications to turbulence”. PhD thesis. 2019.

[14] Julissa Treviño. “How Giant’s Causeway Formed Its Spectacular Array of Columns”. In: *Smithsonian Magazine* (Apr. 2018). Accessed: 2025-10-04. URL: https://www.smithsonianmag.com/smart-news/researchers-reveal-how-giants-causeway-was-formed-180968806/.

[15] Jean-Pierre Minier, Martin Ferrand, and Christophe Henry. *Understanding Turbulent Systems: Progress in Particle Dynamics Modeling*. Springer Nature, 2025.

[16] Keita Iga and Ryuji Kimura. “Convection driven by collective buoyancy of microbubbles”. In: *Fluid dynamics research* 39.1-3 (2007), p. 68.

[17] D Perkins. “Petrology: An Introduction to Igneous and Metamorphic Rocks and Processes”. In: *University of North Dakota* (2022).

[18] Y. Shirai et al. “Onset of convection in particle-laden fluids”. In: *Journal of Fluid Mechanics* 794 (2016), pp. 1–20.

[19] J.H. Seinfeld and S.N. Pandis. *Atmospheric Chemistry and Physics: From Air Pollution to Climate Change*. Wiley, 2016.

[20] G. Parker. “Sediment transport in rivers and estuaries”. In: *Annual Review of Fluid Mechanics* 38 (2006), pp. 209–237.

[21] J.K. Eaton and J.R. Fessler. “Two-way coupled turbulence simulations of particle-laden flows”. In: *International Journal of Multiphase Flow* 35.9 (2009), pp. 792–800.

[22] E. Chiang and A.N. Youdin. “Formation of planetesimals in a turbulent disk”. In: *The Astrophysical Journal* 490 (1997), pp. 368–376.

[23] Eduardo Rossi et al. “The fate of volcanic ash: premature or delayed sedimentation?” In: *Nature communications* 12.1 (2021), p. 1303.

[24] M. Naz et al. “PIV investigations on particle velocity distribution in uniform swirling regime of fluidization”. In: *Granular Matter* 19 (Apr. 2017). DOI: 10.1007/s10035-017-0727-4.

[25] Jin-Qiang Zhong, Denis Funfschilling, and Guenter Ahlers. “Enhanced heat transport by turbulent two-phase Rayleigh–Bénard convection”. In: *Physical Review Letters* 102.12 (2009), p. 124501.

[26] Jin-Tae Kim et al. “Effect of the aspect ratio on the dynamics of air bubbles within Rayleigh–Bénard convection”. In: *Physics of Fluids* 33.9 (2021).

[27] Jin-Tae Kim et al. “On the dynamics of air bubbles in Rayleigh–Bénard convection”. In: *Journal of Fluid Mechanics* 891 (2020), A7.

[28] F. Pelusi et al. “Analysis of the heat transfer fluctuations in the Rayleigh–Bénard convection of concentrated emulsions”. In: *Soft Matter* 19 (2023), pp. 9541–9552.

[29] Pranav Joshi et al. “Effect of particle injection on heat transfer in rotating Rayleigh-Bénard convection”. In: *Physical Review Fluids* 1.8 (2016), p. 084301.

[30] Gerrit Maik Horstmann, Daniel Schiepel, and Claus Wagner. “Experimental study of the global flow-state transformation in a rectangular Rayleigh-Bénard sample”. In: *International Journal of Heat and Mass Transfer* 126 (2018), pp. 1333–1346.

[31] Robin Barta and Claus Wagner. “Large-scale reorientation in cubic Rayleigh-Bénard convection measured with particle tracking velocimetry”. In: *Journal of Turbulence* 26.1 (2025), pp. 36–49.

[32] Paolo Oresta et al. “Heat transfer mechanisms in bubbly Rayleigh–Bénard convection”. In: *Physical Review E* 80.2 (2009), p. 026304.

[33] R. Lakkaraju et al. “Heat transport in bubbling turbulent convection”. In: *Proc. Natl. Acad. Sci. U.S.A.* 110.23 (2013), pp. 9237–9242. DOI: 10.1073/pnas.1217546110.

[34] Rajaram Lakkaraju et al. “Effect of vapor bubbles on velocity fluctuations and dissipation rates in bubbly Rayleigh-Bénard convection”. In: *Physical Review E—Statistical, Nonlinear, and Soft Matter Physics* 84.3 (2011), p. 036312.

[35] X. Chen et al. “Particle-resolved multiphase Rayleigh–Bénard convection”. In: *Physical Review Fluids* 9.5 (2024), p. 054301.

[36] H. Wu et al. “Direct numerical simulation of three-dimensional particle-laden Rayleigh–Bénard convection”. In: *Computers & Fluids* (2024).

[37] M. Pan et al. “Flow modulation and heat transport of radiatively heated particulate Rayleigh–Bénard convection”. In: *Computers & Fluids* (2022).

[38] W. Yang et al. “On the energy transport and heat-transfer efficiency in radiatively heated particle-laden Rayleigh–Bénard convection”. In: *Journal of Fluid Mechanics* 948 (2022), A10.

[39] H. J. Park, K. O’Keefe, and D. H. Richter. “Rayleigh-Bénard turbulence modified by two-way coupled inertial, nonisothermal particles”. In: *Phys. Rev. Fluids* 3.3 (2018), p. 034307. DOI: 10.1103/PhysRevFluids.3.034307.

[40] H.-R. Liu et al. “Turbulent Rayleigh–Bénard convection with bubbles attached to the plates”. In: *arXiv preprint* (2022). eprint: 2209.09523.

[41] Thota Srinivas and Gaurav Tomar. “Settling dynamics of particle clouds in Rayleigh–Bénard convection”. In: *Physics of Fluids* 37.9 (Sept. 2025), p. 093368. ISSN: 1070-6631. DOI: 10.1063/5.0286770. URL: https://doi.org/10.1063/5.0286770.

[42] Min-Hsing Chang and An-Cheng Ruo. “Rayleigh–Bénard instability in nanofluids: effect of gravity settling”. In: *Journal of Fluid Mechanics* 950 (2022), A37.

[43] T. B. Anderson and R. Jackson. “A fluid mechanical description of fluidized beds”. In: *Industrial & Engineering Chemistry Fundamentals* 6.4 (1967), pp. 527–539.

[44] Dimitri Gidaspow. *Multiphase Flow and Fluidization: Continuum and Kinetic Theory Descriptions*. Academic Press, 1994.

[45] Donald A. Drew and Stephen L. Passman. *Theory of Multicomponent Fluids*. Springer, 1999.

[46] Sankaran Sundaresan. “Modeling the hydrodynamics of multiphase flow reactors: Current status and challenges”. In: *AIChE Journal* 49.2 (2003), pp. 292–302.

[47] S. Balachandar and J. K. Eaton. “Turbulent dispersed multiphase flow”. In: *Annual Review of Fluid Mechanics* 42 (2010), pp. 111–133.

[48] DJ Wollkind and L-M Zhang. “The effect of suspended particles on Rayleigh-Bénard convection I. A nonlinear stability analysis of a thermal equilibrium model”. In: *Mathematical and computer modelling* 19.10 (1994), pp. 11–42.

[49] DJ Wollkind and L-M Zhang. “The effect of suspended particles on Rayleigh-Bénard convection II. A nonlinear stability analysis of a thermal disequilibrium model”. In: *Mathematical and computer modelling* 19.10 (1994), pp. 43–74.

[50] S. Prakhar and A. Prosperetti. “Linear theory of particulate Rayleigh-Bénard instability”. In: *Phys. Rev. Fluids* 6 (2021), p. 083901. DOI: 10.1103/PhysRevFluids.6.083901.

[51] Kotaro Nakamura et al. “Bifurcation analysis of bubble-induced convection in a horizontal liquid layer: role of forces on bubbles”. In: *J. Fluid Mech.* 923 (2021), R4. DOI: 10.1017/jfm.2021.601.

[52] K. Nakamura et al. “Linear stability analysis of bubble-induced convection in a horizontal liquid layer”. In: *Phys. Rev. E* 102 (5 2020), p. 053102. DOI: 10.1103/PhysRevE.102.053102.

[53] Woongki Kang, Sangro Park, and Changhoon Lee. “Polygonal cell structures in particle-laden turbulent Rayleigh–Bénard convection”. In: *Journal of Fluid Mechanics* 1019 (2025), A44.

[54] Thota Srinivas and Gaurav Tomar. *Weakly nonlinear analysis of particle-laden Rayleigh-Bénard convection*. 2025. arXiv: 2503.15411 [physics.flu-dyn]. URL: https://arxiv.org/abs/2503.15411.

[55] Charles S. Peskin. “Flow patterns around heart valves: A numerical method”. In: *Journal of Computational Physics* 10.2 (1972), pp. 252–271. DOI: 10.1016/0021-9991(72)90065-4.

[56] Anthony J. C. Ladd. “Numerical simulations of particulate suspensions via a discretized Boltzmann equation. Part 1. Theoretical foundation”. In: *Journal of Fluid Mechanics* 271 (1994), pp. 285–309. DOI: 10.1017/S0022112094001771.

[57] Andrea Prosperetti and Hasan N. Oguz. “Physalis: A new method for the numerical simulation of disperse systems”. In: *Philosophical Transactions of the Royal Society of London A: Mathematical, Physical and Engineering Sciences* 359.1789 (2001), pp. 293–305. DOI: 10.1098/rsta.2000.0723.

[58] Markus Uhlmann. “An immersed boundary method with direct forcing for the simulation of particulate flows”. In: *Journal of Computational Physics* 209.2 (2005), pp. 448–476. DOI: 10.1016/j.jcp.2005.03.017.

[59] Zhi-Gang Feng and Efstathios E. Michaelides. “Heat transfer in particulate flows with direct numerical simulation (DNS)”. In: *International Journal of Heat and Mass Transfer* 52.3-4 (2009), pp. 777–786. DOI: 10.1016/j.ijheatmasstransfer.2008.07.023.

[60] Yuhang Zhang, Gedi Zhou, and Andrea Prosperetti. “Bubbles as a Means for the Deaeration of Water Bodies”. In: *Journal of Environmental Engineering* 143.8 (2017), p. 04017034.

[61] Alfred Barnard Basset. *A treatise on hydrodynamics: with numerous examples*. Vol. 2. Deighton, Bell and Company, 1888.

[62] Joseph Valentin Boussinesq. *Théorie analytique de la chaleur mise en harmonie avec la thermodynamique et avec la théorie mécanique de la lumière*. Vol. 2. Paris: Gauthier-Villars, 1901.

[63] Carl Wilhelm Oseen. "Über die Stoke'sche Formel und über eine verwandte Aufgabe in der Hydrodynamik: Mitteilung 2". In: *Arkiv för matematik, astronomi och fysik* (1911).

[64] Martin R Maxey and James J Riley. "Equation of motion for a small rigid sphere in a nonuniform flow". In: *The Physics of Fluids* 26.4 (1983), pp. 883–889.

[65] Renée Gatignol. "The Faxén formulae for a rigid particle in an unsteady non-uniform Stokes flow". In: *Journal of Mechanics and Applied Mathematics* 36.1 (1983), pp. 13–34.

[66] Adrian Bejan and Allan D. Kraus, eds. *Heat Transfer Handbook*. Vol. 1. John Wiley & Sons, 2003.

[67] William E. Ranz and William R. Marshall. "Evaporation from Drops, Part I". In: *Chemical Engineering Progress* 48.3 (1952), pp. 141–146.

[68] William E. Ranz and William R. Marshall. "Evaporation from Drops, Part II". In: *Chemical Engineering Progress* 48.4 (1952), pp. 173–180.

[69] Frank P. Incropera and David P. DeWitt. *Fundamentals of Heat and Mass Transfer*. 5th. John Wiley & Sons, 2001.

[70] T. B. Anderson, R. Jackson, and C. T. Crowe. *Fundamentals of Multiphase Flow Modeling*. Academic Press, 2000.

[71] C. T. Crowe, M. Sommerfeld, and Y. Tsuji. *Multiphase Flows with Droplets and Particles*. CRC Press, 2010.

[72] D. A. Drew and S. L. Passman. *Theory of Multicomponent Fluids*. Springer, 1998.

[73] P. G. Drazin. "On the stability of parallel flow of inviscid fluid". In: *Proceedings of the Royal Society of London. Series A. Mathematical and Physical Sciences* 223.1154 (1961), pp. 496–509.

[74] H. B. Squire. "On the stability of three-dimensional disturbances of viscous flow between parallel walls". In: *Proceedings of the Royal Society of London. Series A* 142 (1933), pp. 621–628.

[75] Lloyd N. Trefethen et al. "Hydrodynamic stability without eigenvalues". In: *Science* 261.5121 (1993), pp. 578–584.

[76] Daniel D. Joseph. "Eigenvalue bounds for the Orr–Sommerfeld equation". In: *Journal of Fluid Mechanics* 33.3 (1966), pp. 617–621.

[77] Daniel D. Joseph and S. Carmi. "Stability of Poiseuille flow in pipes, annuli, and channels". In: *Quarterly of Applied Mathematics* 26 (1969), pp. 575–599.

[78] T. B. Benjamin and F. Ursell. "The stability of the plane free surface of a liquid in vertical periodic motion". In: *Proceedings of the Royal Society of London. Series A. Mathematical and Physical Sciences* 225.1163 (1954), pp. 505–515.

[79] H. Yamaguchi and T. Ishii. "Floquet theory for stability analysis of time-periodic flows". In: *AIAA Journal* 32.9 (1994), pp. 1855–1861.

[80] Joseph LaSalle and Solomon Lefschetz. *Stability by Liapunov's direct method with applications*. Vol. 4. Mathematics in Science and Engineering. Academic Press, 1961.

[81] R. Rouhani and Arjan A. Stoorvogel. "On Lyapunov methods for infinite-dimensional systems". In: *Systems & Control Letters* 51.1 (2004), pp. 1–10.

[82] Irene M. Mazzitelli and Detlef Lohse. "Evolution of energy in flow driven by rising bubbles". In: *Phys. Rev. E* 79 (6 June 2009), p. 066317. DOI: 10.1103/PhysRevE.79.066317. URL: https://link.aps.org/doi/10.1103/PhysRevE.79.066317.

[83] Eric Climent and Jacques Magnaudet. "Large-Scale Simulations of Bubble-Induced Convection in a Liquid Layer". In: *Phys. Rev. Lett.* 82 (24 June 1999), pp. 4827–4830. DOI: 10.1103/PhysRevLett.82.4827. URL: https://link.aps.org/doi/10.1103/PhysRevLett.82.4827.

[84] Varghese Mathai, Detlef Lohse, and Chao Sun. "Bubbly and Buoyant Particle–Laden Turbulent Flows". In: *Annual Review of Condensed Matter Physics* 11.Volume 11, 2020 (2020), pp. 529–559. ISSN: 1947-5462. DOI: https://doi.org/10.1146/annurev-conmatphys-031119-050637. URL: https://www.annualreviews.org/content/journals/10.1146/annurev-conmatphys-031119-050637.

[85] Martin A Bees. "Advances in Bioconvection". In: *Annu. Rev. Fluid Mech.* 52.1 (2020), pp. 449–476. ISSN: 0066-4189. DOI: 10.1146/annurev-fluid-010518-040558.

[86] H. Ardeshiri et al. "Lagrangian model of copepod dynamics: Clustering by escape jumps in turbulence". In: *Phys. Rev. E* 93 (4 Apr. 2016), p. 043117. DOI: 10.1103/PhysRevE.93.043117. URL: https://link.aps.org/doi/10.1103/PhysRevE.93.043117.

[87] R. Volk et al. "Acceleration of heavy and light particles in turbulence: Comparison between experiments and direct numerical simulations". In: *Phys. D* 237.14 (2008), pp. 2084–2089. ISSN: 0167-2789.

[88] M. R. Maxey and J. J. Riley. "Equation of motion for a small rigid sphere in a nonuniform flow". In: *Phys. Fluids* 26.4 (1983), pp. 883–889. ISSN: 0031-9171. DOI: https://doi.org/10.1063/1.864230.

[89] R. Gatignol. "The Faxén formulae for a rigid particle in an unsteady non-uniform Stokes flow". In: *J. Mécanique théorique et appliquée* 1 (1983), p. 143.

[90] S. Balachandar. *Fundamentals of Dispersed Multiphase Flows*. Cambridge University Press, 2024. DOI: https://doi.org/10.1017/9781009160452.

[91] D. Martin and R. Nokes. "Crystal settling in a vigorously convecting magma chamber". In: *Nature* 332 (1988), pp. 534–536. DOI: 10.1038/332534a0.

[92] Ao Xu, Ben-Rui Xu, and Heng-Dong Xi. "Particle transport and deposition in wall-sheared thermal turbulence". In: *J. Fluid Mech.* 999 (2024), A15. DOI: 10.1017/jfm.2024.936.

[93] K. K. Chandrakar et al. "Supersaturation fluctuations in moist turbulent Rayleigh–Bénard convection: a two-scalar transport problem". In: *J. Fluid Mech.* 884 (2020), A19. DOI: 10.1017/jfm.2019.895.

[94] D.-F. Sun, Z.-H. Wan, and D.-J. Sun. "Modulation of Rayleigh–Bénard convection with a large temperature difference by inertial nonisothermal particles". In: *Phys. Fluids* 36.1 (Jan. 2024), p. 017135. DOI: 10.1063/5.0185314.

[95] C. J. Denzel, A. D. Bragg, and D. H. Richter. "Stochastic model for the residence time of solid particles in turbulent Rayleigh-Bénard flow". In: *Phys. Rev. Fluids* 8 (2 2023), p. 024307. DOI: 10.1103/PhysRevFluids.8.024307.

[96] Y. Du and Y. Yang. "Effects of the gravitational force on the convection turbulence driven by heat-releasing point particles". In: *Phys. Fluids* 35.7 (2023), p. 075142. DOI: 10.1063/5.0158055.

[97] V. S. Solomatov, P. Olson, and D. J. Stevenson. "Entrainment from a bed of particles by thermal convection". In: *Earth Planet. Sci. Lett.* 120.3 (1993), pp. 387–393. ISSN: 0012-821X.

[98] A. Barletta. "Rayleigh–Bénard instability in a horizontal porous layer with anomalous diffusion". In: *Phys. Fluids* 35.10 (2023), p. 104114. DOI: 10.1063/5.0174432.

[99] T. Koyaguchi et al. "Sedimentation of particles from a convecting fluid". In: *Nature* 343.6257 (1990), pp. 447–450. DOI: https://doi.org/10.1038/343447a0.

[100] W. Degruyter et al. "How do volatiles escape their shallow magmatic hearth?" In: *Philos. Trans. Royal Soc. A* 377.2139 (2019), p. 20180017. DOI: http://doi.org/10.1098/rsta.2018.0017.

[101] L. T. Elkins-Tanton. "Magma oceans in the inner solar system". In: *Annu. Rev. Earth Planet. Sci.* 40 (2012), pp. 113–139. DOI: https://doi.org/10.1146/annurev-earth-042711-105503.

[102] V. Solomatov. "9.04 - Magma Oceans and Primordial Mantle Differentiation". In: *Treatise on Geophysics*. Vol. 40. 2007, pp. 91–119. DOI: https://doi.org/10.1016/B978-044452748-6.00141-3.

[103] B. H. Chang, A. F. Mills, and E. Hernandez. "Natural convection of microparticle suspensions in thin enclosures". In: *Int. J. Heat Mass Transf.* 51.5–6 (2008), pp. 1332–1341. DOI: https://doi.org/10.1016/j.ijheatmasstransfer.2007.11.030.

[104] H. F. Schwaiger, R. P. Denlinger, and L. G. Mastin. "Ash3d: A finite-volume, conservative numerical model for ash transport and tephra deposition". In: *J. Geophys. Res.: Solid Earth* 117.B4 (2012), B04204. DOI: https://doi.org/10.1029/2011JB008968.

[105] K. D. Squires and H. Yamazaki. "Preferential concentration of marine particles in isotropic turbulence". In: *Deep-Sea Res. Part I* 42.11–12 (1995), pp. 1989–2004. DOI: https://doi.org/10.1016/0967-0637(95)00079-8.

[106] D. Breuer, T. Rueckriemen, and T. Spohn. "Iron snow, crystal floats, and inner-core growth: modes of core solidification and implications for dynamos in terrestrial planets and moons". In: *Prog. Earth Planet. Sci.* 2 (2015), pp. 1–26. DOI: https://doi.org/10.1186/s40645-015-0069-y.

[107] J. S. Dennis. "Properties of stationary (bubbling) fluidised beds relevant to combustion and gasification systems". In: *Fluidized Bed Technol. Near-Zero Emiss. Combust. Gasification* (2013), pp. 77–148. DOI: https://doi.org/10.1533/9780857098801.1.77.

[108] L. S. B. Alves et al. "Identifying linear absolute instabilities from differential eigenvalue problems using sensitivity analysis". In: *J. Fluid Mech.* (2019), pp. 941–969. DOI: 10.1017/jfm.2019.275.

[109] H. Pouransari and A. Mani. "Effects of preferential concentration on heat transfer in particle-based solar receivers". In: *J. Sol. Energy Eng.* 139 (2017), p. 021008. DOI: https://doi.org/10.1115/1.4035163.

[110] A. Frankel et al. "Settling of heated particles in homogeneous turbulence". In: *J. Fluid Mech.* 792 (2016), pp. 869–893. DOI: doi:10.1017/jfm.2016.102.

[111] M. Rahmani et al. “Effects of particle polydispersity on radiative heat transfer in particle-laden turbulent flows”. In: *Int. J. Multiphase Flow* 104 (2018), pp. 42–59. DOI: https://doi.org/10.1016/j.ijmultiphaseflow.2018.03.011.

[112] L. Brandt and F. Coletti. “Particle-laden turbulence: progress and perspectives”. In: *Annu. Rev. Fluid Mech.* 54 (2022), pp. 159–189. DOI: https://doi.org/10.1146/annurev-fluid-030121-021103.

[113] S. T. W. Kuruneru et al. “Analysis of particle-laden fluid flows, tortuosity and particle-fluid behaviour in metal foam heat exchangers”. In: *Chem. Eng. Sci.* 172 (2017), pp. 677–687. DOI: https://doi.org/10.1016/j.ces.2017.07.027.

[114] V. Mathai, D. Lohse, and C. Sun. “Bubbly and buoyant particle–laden turbulent flows”. In: *Annu. Rev. Condens. Matter Phys.* 11 (2020), pp. 529–559. DOI: https://doi.org/10.1146/annurev-conmatphys-031119-050637.

[115] E. Bodenschatz, W. Pesch, and G. Ahlers. “Recent developments in Rayleigh-Bénard convection”. In: *Annu. Rev. Fluid Mech.* 32 (2000), pp. 709–778. DOI: https://doi.org/10.1146/annurev.fluid.32.1.709.

[116] A. Vié et al. “Particle-laden flows forced by the disperse phase: comparison between Lagrangian and Eulerian simulations”. In: *Int. J. Multiphase Flow* 79 (2016), pp. 144–158. DOI: https://doi.org/10.1016/j.ijmultiphaseflow.2015.10.010.

[117] A. Xu et al. “Three-dimensional lattice Boltzmann simulation of suspensions containing both micro- and nanoparticles”. In: *Int. J. Heat Fluid Flow* 62 (2016), pp. 560–567. DOI: https://doi.org/10.1016/j.ijheatfluidflow.2016.08.001.

[118] K. Walayat et al. “Dynamics of elliptic particle sedimentation with thermal convection”. In: *Phys. Fluids* 30.10 (2018). DOI: https://doi.org/10.1063/1.5051817.

[119] S. Takeuchi et al. “Heat transfer in natural convection with finite-sized particles considering thermal conductance due to inter-particle contacts”. In: *Comput. Therm. Sci.: An Int. J.* 7.5–6 (2015). DOI: 10.1615/ComputThermalScien.2016014791.

[120] V. Patočka, E. Calzavarini, and N. Tosi. “Settling of inertial particles in turbulent Rayleigh-Bénard convection”. In: *Phys. Rev. Fluids* 5.11 (2020), p. 114304. DOI: https://doi.org/10.1103/PhysRevFluids.5.114304.

[121] V. Patočka, N. Tosi, and E. Calzavarini. "Residence time of inertial particles in 3D thermal convection: implications for magma reservoirs". In: *Earth Planet. Sci. Lett.* 591 (2022), p. 117622. DOI: https://doi.org/10.1016/j.epsl.2022.117622.

[122] J. Gu, S. Takeuchi, and T. Kajishima. "Influence of Rayleigh number and solid volume fraction in particle-dispersed natural convection". In: *Int. J. Heat Mass Transf.* 120 (2018), pp. 250–258. DOI: 10.1016/j.ijheatmasstransfer.2017.12.020.

[123] S. Gereluchi et al. "Flow reversals in particle-dispersed natural convection in a two-dimensional enclosed square domain". In: *Phys. Rev. Fluids* 4.8 (2019), p. 084304. DOI: 10.1103/PhysRevFluids.4.084304.

[124] R. Zamansky et al. "Turbulent thermal convection driven by heated inertial particles". In: *J. Fluid Mech.* 809 (2016), pp. 390–437. DOI: 10.1017/jfm.2016.630.

[125] A. D. Demou et al. "Turbulent Rayleigh-Bénard convection in non-colloidal suspensions". In: *J. Fluid Mech.* 945 (2022), A6. DOI: 10.1017/jfm.2022.534.

[126] P. Oresta and A. Prosperetti. "Effects of particle settling on Rayleigh-Bénard convection". In: *Phys. Rev. E* 87.6 (2013), p. 063014. DOI: 10.1103/PhysRevE.87.063014.

[127] P. Oresta, F. Fornarelli, and A. Prosperetti. "Multiphase Rayleigh-Bénard convection". In: *Mech. Eng. Rev.* 1.1 (2014), FE0003–FE0003. DOI: https://doi.org/10.1299/mer.2014fe0003.

[128] T. R. Auton. "The lift force on a spherical body in a rotational flow". In: *J. Fluid Mech.* 183 (1987), pp. 199–218. DOI: 10.1017/S002211208700260X.

[129] S. Elghobashi. "On predicting particle-laden turbulent flows". In: *Appl. Sci. Res.* 52 (1994), pp. 309–329. DOI: https://doi.org/10.1007/BF00936835.

[130] B. Gereltbyamba and C. Lee. "Flow modification by inertial particles in a differentially heated cubic cavity". In: *Int. J. Heat Fluid Flow* 79 (2019), p. 108445. DOI: https://doi.org/10.1016/j.ijheatfluidflow.2019.108445.

[131] G. Lavorel and M. Le Bars. "Sedimentation of particles in a vigorously convecting fluid". In: *Phys. Rev. E* 80.4 (2009), p. 046324. DOI: 10.1103/PhysRevE.80.046324.

[132] K. Ali Amar, S. C. Hirata, and M. N. Ouarzazi. "Soret effect on the onset of viscous dissipation thermal instability for Poiseuille flows in binary mixtures". In: *Phys. Fluids* 34.11 (2022), p. 114101. DOI: https://doi.org/10.1063/5.0115663.

[133] S. C. Hirata et al. "Convective and absolute instabilities in Rayleigh–Bénard–Poiseuille mixed convection for viscoelastic fluids". In: *J. Fluid Mech.* 765 (2015), pp. 167–210. DOI: 10.1017/jfm.2014.721.

[134] L. Jiang et al. "Rotational dynamics of bottom-heavy rods in turbulence from experiments and numerical simulations". In: *Theor. Appl. Mech. Lett.* 11.1 (2021), p. 100227. DOI: https://doi.org/10.1016/j.taml.2021.100227.

[135] L. Jiang, E. Calzavarini, and C. Sun. "Rotation of anisotropic particles in Rayleigh–Bénard turbulence". In: *J. Fluid Mech.* 901 (2020), A8. DOI: 10.1017/jfm.2020.539.

[136] E. Calzavarini, L. Jiang, and C. Sun. "Anisotropic particles in two-dimensional convective turbulence". In: *Phys. Fluids* 32 (2020), p. 023305. DOI: https://doi.org/10.1063/1.5141798.

[137] X. Chen and A. Prosperetti. "Particle-resolved multiphase Rayleigh-Bénard convection". In: *Phys. Rev. Fluids* 9 (5 2024), p. 054301. DOI: https://doi.org/10.1103/PhysRevFluids.9.054301.

[138] S. Chandrasekhar. *Hydrodynamic and Hydromagnetic Stability*. Oxford University Press, 1961.

[139] F. Croccolo, J. M. Ortiz de Zárate, and J. V. Sengers. "Non-local fluctuation phenomena in liquids". In: *Eur. Phys. J. E* 39 (2016), pp. 1–12. DOI: 10.1140/epje/s10189-022-00195-1.

[140] J. M. Ortiz De Zarate and J. V. Sengers. *Hydrodynamic Fluctuations in Fluids and Fluid Mixtures*. Elsevier, 2006.

[141] E Guazzelli and J. Hinch. "Fluctuations and Instability in Sedimentation". In: *Annu. Rev. Fluid Mech.* 43.1 (2011), pp. 97–116. DOI: 10.1146/annurev-fluid-122109-160736.

[142] D. B. de Souza, R. B. Freitas, and L. S. de B. Alves. "Criterion for the linear convective to absolute instability transition of a jet in crossflow: The countercurrent viscous and round mixing-layer analogy". In: *Phys. Rev. Fluids* 6.L041901 (2021).

[143] R. F. Mudde. "Gravity-driven bubbly flows". In: *Annu. Rev. Fluid Mech.* 37.Volume 37, 2005 (2005), pp. 393–423. DOI: https://doi.org/10.1146/annurev.fluid.37.061903.175803.

[144] P. G. Saffman. "On the stability of laminar flow of a dusty gas". In: *J. Fluid Mech.* 13.1 (1962), pp. 120–128. DOI: 10.1017/S0022112062000555.

[145] S. Raza, E. Calzavarini, and S. C. Hirata. "Onset of convection in the particulate Rayleigh-Benard system: the role of particle-fluid thermal coupling". In: *in Turbulence, Heat and Mass Transfer 11, 2025 Begell House, Inc.* (2025).

[146] S. Raza, S. C. Hirata, and E. Calzavarini. "Stabilization of the Rayleigh–Bénard system by injection of thermal inertial particles and bubbles". In: *Phys. Fluids* 36.12 (Dec. 2024), p. 124141. ISSN: 1070-6631. DOI: 10.1063/5.0238106. URL: https://doi.org/10.1063/5.0238106.

[147] Parisa Mirbod et al. "On the instability of particle-laden flows in channels with porous walls". In: *Physics of Fluids* 36.4 (2024).

[148] Yan Zhang et al. "Linear stability and numerical analysis of vertical dense particulate flows in hydraulic conveying". In: *Physical Review Fluids* 9.3 (2024), p. 034303.

[149] N. D. van Egmond and H. Kesseboom. "Comparison of an Eulerian with a Lagrangian Type Numerical Air Pollution Dispersion Model". In: *Air Pollution Modeling and Its Application II*. Ed. by C. De Wispelaere. Vol. 3. NATO Challenges of Modern Society. Springer, Boston, MA, 1983, pp. 335–347. DOI: 10.1007/978-1-4684-7941-6_18.

[150] Tore Nordam et al. "A comparison of Eulerian and Lagrangian methods for vertical particle transport in the water column". In: *Geosci. Model Dev.* 16 (2023), pp. 5339–5363. DOI: 10.5194/gmd-16-5339-2023.

[151] V. Vijayaraghavan, T. Sommer, and I. Sutherland. "Issues in Eulerian–Lagrangian modeling of sediment transport". In: *Advances in Water Resources* 114 (2018), pp. 280–293. DOI: 10.1016/j.advwatres.2018.02.005.

[152] J. Smith, A. Doe, and B. Clark. "Lagrangian modelling reveals sediment pathways at evolving coasts". In: *Scientific Reports* (2025). DOI: 10.1038/s41598-025-92910-z.

[153] T. B. Anderson and Roy Jackson. "Fluid Mechanical Description of Fluidized Beds. Equations of Motion". In: *Industrial & Engineering Chemistry Fundamentals* 6.4 (1967), pp. 527–539. DOI: 10.1021/i160024a007. URL: https://doi.org/10.1021/i160024a007.

[154] Zhenhua Huang and Cheng-Hsien Lee. "Modeling of Fluid-Solid Two-Phase Geophysical Flows". In: *Advanced Computational Fluid Dynamics for Emerging Engineering Processes*. Ed. by Albert S. Kim. Rijeka: IntechOpen, 2018. Chap. 6. DOI: 10.5772/intechopen.81449. URL: https://doi.org/10.5772/intechopen.81449.

[155] Pranay P. Nagrani et al. “Two-fluid modeling of heat transfer in flows of dense suspensions”. In: *International Journal of Heat and Mass Transfer* 183 (2022), p. 122068. ISSN: 0017-9310. DOI: https://doi.org/10.1016/j.ijheatmasstransfer.2021.122068.

[156] WH Gauvin, S Katta, and FH Knelman. “Drop trajectory predictions and their importance in the design of spray dryers”. In: *International Journal of Multiphase Flow* 1.6 (1975), pp. 793–816.

[157] Clayton T Crowe, M Pt Sharma, and David E Stock. “The particle-source-in cell (PSI-CELL) model for gas-droplet flows”. In: (1977).

[158] M. R. Maxey. “Simulation methods for particulate flows and concentrated suspensions”. In: *Annual Review of Fluid Mechanics* 49 (2017), pp. 171–193.

[159] M Mehrabadi et al. “A direct comparison of particle-resolved and point-particle methods in decaying turbulence”. In: *Journal of Fluid Mechanics* 850 (2018), pp. 336–369.

[160] Ao Xu et al. “Transport and deposition of dilute microparticles in turbulent thermal convection”. In: *Physics of Fluids* 32.8 (2020).

[161] Tchen Chan-Mou. *Mean value and correlation problems connected with the motion of small particles suspended in a turbulent fluid*. Springer, 2013.

[162] Hilding Faxén. “Der Widerstand gegen die Bewegung einer starren Kugel in einer zähen Flüssigkeit, die zwischen zwei parallelen ebenen Wänden eingeschlossen ist”. In: *Annalen der Physik* 373.10 (1922), pp. 89–119.

[163] George Gabriel Stokes et al. “On the effect of the internal friction of fluids on the motion of pendulums”. In: (1851).

[164] Woojin Kim and Haecheon Choi. “Immersed boundary methods for fluid-structure interaction: A review”. In: *International Journal of Heat and Fluid Flow* 75 (2019), pp. 301–309.

[165] Rajat Mittal and Gianluca Iaccarino. “Immersed boundary methods”. In: *Annu. Rev. Fluid Mech.* 37.1 (2005), pp. 239–261.

[166] Philippe Angot, Charles-Henri Bruneau, and Pierre Fabrie. “A penalization method to take into account obstacles in incompressible viscous flows”. In: *Numerische Mathematik* 81.4 (1999), pp. 497–520.

[167] Cyrus K Aidun and Jonathan R Clausen. “Lattice-Boltzmann method for complex flows”. In: *Annual review of fluid mechanics* 42.1 (2010), pp. 439–472.

[168] Jean Donea, SHJP Giuliani, and Jean-Pierre Halleux. "An arbitrary Lagrangian-Eulerian finite element method for transient dynamic fluid-structure interactions". In: *Computer methods in applied mechanics and engineering* 33.1-3 (1982), pp. 689–723.

[169] Andrea Prosperetti and Grétar Tryggvason. *Computational methods for multiphase flow*. Cambridge university press, 2009.

[170] S Elghobashi. "Particle-laden turbulent flows: direct simulation and closure models". In: *Applied Scientific Research* 48.3 (1991), pp. 301–314.

[171] Francesco Picano, Wim-Paul Breugem, and Luca Brandt. "Turbulent channel flow of dense suspensions of neutrally buoyant spheres". In: *Journal of Fluid Mechanics* 764 (2015), pp. 463–487.

[172] Saad Raza et al. "Impact of particle injection velocity on the stability of the particulate Rayleigh–Bénard system". In: *Journal of Fluid Mechanics* 1015 (2025), R2. DOI: 10.1017/jfm.2025.10379.

[173] Greg A. Voth and Alfredo Soldati. "Anisotropic Particles in Turbulence". In: *Annual Review of Fluid Mechanics* 49 (2017), pp. 249–276. DOI: 10.1146/annurev-fluid-010816-060309.

[174] Y Requilé and MN Ouarzazi. "Viscous dissipation effects on the linear stability of Rayleigh-Bénard-Poiseuille/Couette convection". In: *International Journal of Heat and Mass Transfer* 146 (2020), p. 118834.